CONTROL OF METALLURGICAL, MAGNETIC AND ELECTRICAL PROPERTIES OF ELECTRODEPOSITED CoFeNi THIN FILMS AND Cu NANOSTRUCTURES

A Dissertation

Presented to

the Faculty of the Department of Electrical and Computer Engineering

University of Houston

In Partial Fulfillment

of the Requirements for the Degree

Doctor of Philosophy

in Electrical Engineering

by

Nikhil Dole

May 2014

DEDICATION

I would like to dedicate this dissertation to my grandma, mom and dad whose unending love for me gave me the courage to win against all odds and achieve this success today. Thank you for being such a wonderful and caring family!!

ACKNOWLEDGEMENTS

I would like to use this opportunity to express my gratitude to my research advisor, Dr. Stanko R. Brankovic, for his unending patience, guidance and support during my research work. His knowledge and expertise in the field of thin film electrodeposition and magnetic material synthesis is unsurmountable. I still remember those long hours of discussion with him which helped me solve most of the complicated issues in my research. There is so much to learn from him and I am sure he has transformed me into a better research engineer!!! It was indeed a pleasure working with you Dr. Brankovic!! You will continue to hold a special place in my life!!

I would like to thank my committee members Dr. Jiming Bao, Dr. Paul Ruchhoeft, Dr. James Meen, Dr. Goran Majkic, and Dr. Luis Garfias for serving on my committee and providing me with their valuable inputs in my research and my dissertation document. There are many others in the University namely, Dr. Dmitri Litvinov for allowing me to use his Nanomagnetics Facility for conducting my experiments, Dr. Long Chang and Dr. Kelley Bradley for training me on several instruments in and out of the clean room. I would like to thank Dr. Will French, Dr. Dok Won Lee and Dr. Andrei Papou from Texas Instruments Inc. for their financial support and guidance during the research projects involving design of magnetic alloys for applications in MEMS devices. I would also like to thank Dr. Jasmeet Chawla from Intel Corp. for the informative discussions involving my research and providing us with loads of samples to perform the annealing experiments.

My research experiments would not have been possible without the help of my fellow labmates Qiuyi, Dongjun, Ela, Paul, Aakash, Katherine and former labmates

Jinnie, Dincer, Burhan, Rachit, Joel, Ashish, Siam, Pamela and Ade. Thank you guys for making the lab atmosphere joyful and lively to work. The moments spent with you guys in the lab will be cherished for my entire life.

I have high regards of appreciation for my friends and room-mates, Rachit and Sreejith, who always made sure I did not miss home and my family. This dissertation would have been next to impossible without the love and support of my wife, Amruta Dole, who always believed in me and gave me the courage to tackle all the difficult situations in life. A big hug to my in-laws for showering their love and unending faith in my work. I cannot forget to mention my beloved younger brother, Archit Dole who has been a great support to me and my family back home. God has been gracious to gift me with a wonderful set of parents who have always stood by my side and encouraged me to pursue my dreams!! Not to forget my late grandmother who is the reason behind every moment of success, happiness and prosperity in my life!! Last but not the least I bow before Him, my guru, Shri Gajanan Maharaj, who has answered all my prayers and forgiven my sins. I blindly follow Him...

CONTROL OF METALLURGICAL, MAGNETIC AND ELECTRICAL PROPERTIES OF ELECTRODEPOSITED CoFeNi THIN FILMS AND Cu NANOSTRUCTURES

An Abstract

of a

A Dissertation

Presented to

the Faculty of the Department of Electrical and Computer Engineering

University of Houston

In Partial Fulfillment

of the Requirements for the Degree

Doctor of Philosophy

in Electrical Engineering

by

Nikhil Dole

May 2014

ABSTRACT

The ever increasing quality and reliability demand of microsystems indicate that the electrodeposited magnetic alloys used for their fabrication should have minimum possible magnetic losses at the desired frequency range. In order to meet this challenge, the magnetic industry is facing the task of electrodepositing soft high magnetic moment alloys (SHMM) with high permeability (μ_r>400) and high resistivity (ρ>100$\mu\Omega$-cm). The ternary ferromagnetic CoFeNi alloys represent the class of SHMM alloys which inherently have a higher resistivity than their binary (NiFe or CoFe) counterparts, with similar magnetic properties. In the first part of this research, the work exploring the development of solution chemistry for the electrodeposition of CoFeNi magnetic thin films is discussed. The experimental results (FIB, EDS, XRD, 4-point probe and VSM) indicate that a high deposition rate CoFeNi film can be deposited from the developed bath chemistry yielding high saturation magnetization (M_s~2.0 T), high relative permeability (μ_r~700) and high resistivity (ρ~100$\mu\Omega$-cm). Additionally, the effect of sulfur containing additives like saccharin on the physical, electrical and metallurgical properties of CoFeNi films is studied. The role played by saccharin in stress reduction is exhibited by performing in-situ stress measurements during thin film growth.

The second part of this dissertation focuses on a novel approach towards improving the conductivity of Cu interconnects at nanoscale. The externally applied strain on the Cu interconnects during annealing is used to promote the grain growth via grain boundary densification process. The results indicate that this approach yields positive effect on the resistance of Cu interconnects. The drop in the resistance after

annealing at 200°C and 250°C is observed for externally imposed compressive strain along the Cu interconnects with critical dimensions (CD) of 50nm and 64nm. The analysis and results suggest that the compressive strain during annealing induces densification of the grain boundaries with the interface vector parallel to the current path. These results are of great significance for the overall improvement of conductivity of the Cu interconnects as well as reliability and life span of microelectronic devices.

TABLE OF CONTENTS

LIST OF FIGURES

LIST OF TABLES

CHAPTER 1

INTRODUCTION

1.1. Background

The technical applications of thin metal films in diverse fields such as microelectronics, magnetic recording heads, optical filters and corrosion resistant coatings has led to a large work on studying the properties of these films [1,2]. Remarkable progress in understanding the physical phenomenon of resistivity was achieved by depositing polycrystalline films on varying substrates under favorable deposition conditions. K. Fuchs [2] predicted in a famous paper that the electrical resistivity of thin metal films is due to the scattering of conduction electrons at the film surfaces. Later, however, it became obvious that the grain boundary scattering, surface roughness and film thickness also contributed to the resistivity of the polycrystalline films [2]. The influence of additives, impurities and annealing on the resistivity of the films should be additionally taken into consideration. In this dissertation, the importance of resistivity in electrodeposited magnetic alloys and copper nanostructures is elucidated by proposing innovative techniques to achieve the resistivity control.

1.2. Electrodeposition of High Resistivity Magnetic Materials

The development of theoretical foundations in electrochemical engineering, electrometallurgy and sophistication of tools used for electrodeposition has contributed to the wide-spread use of electrodeposition in the semiconductor and magnetic industries. Nowadays, electrodeposition is recognized as a mature method for fabrication of magnetic thin film heads, and in microelectronics and microelectromechanical system

(MEMS) technologies [3]. In the first part of this dissertation, the electrodeposition processes used for fabrication of soft high moment, high resistivity magnetic alloys are reviewed and their application for lossless energy conversion in MEMS devices is explained.

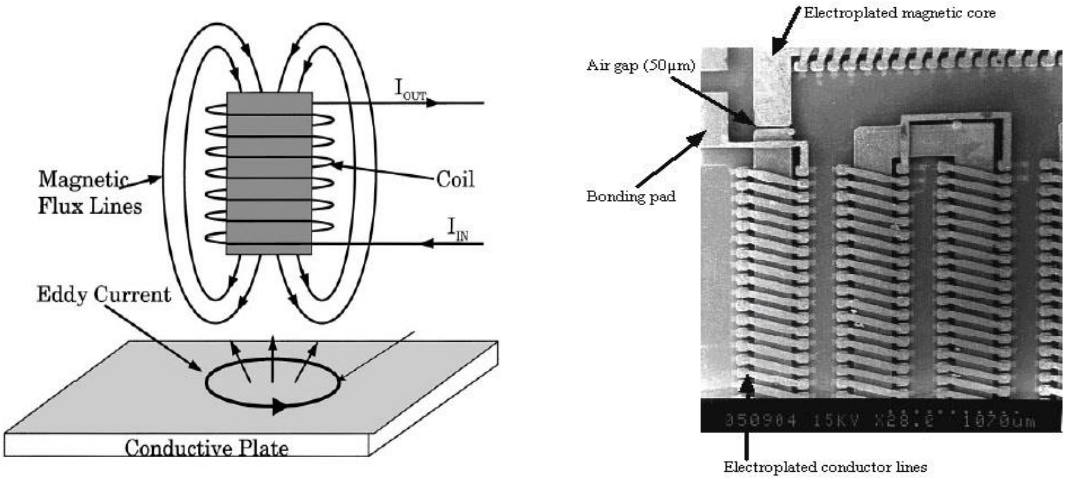

(a) (b)

Figure 1. (a) Eddy currents induced in a conductive plate (b) MEMS transformer with electroplated magnetic core [3].

As shown in Figure 1a, when a conductive material is placed in a varying magnetic field, an electrical current is induced in the material. The current penetrates the material at a shallow depth and is strongest at the surface. These currents are called eddy currents. According to the theory of electromagnetism, circulating a current through a conductor creates its own magnetic field (Figure 1a), which opposes any changes in the current and the external field acting on it. The stronger the external magnetic field, the greater the eddy current is. Consider a MEMS transformer with an electroplated magnetic core as shown in Figure 1b. The magnetic core is used to contain the magnetic flux

produced by the primary winding, and to link the flux to the secondary winding with minimum leakage [3]. Hence, the core needs to be designed with a magnetic material having high flux density (to transfer maximum flux to the secondary winding) and high resistivity (to minimize the eddy current losses). Eddy currents create loss that transforms some electromagnetic energy to heat, known as Joule heating [3]. The loss reduces the efficiency of devices that operate under alternating magnetic field conditions, evident in the iron core of transformers and alternating current motors. The power losses in the transformer due to eddy currents can be explained using Maxwell Equations [3],

$$\nabla \times E = \frac{-\partial B}{\partial t} = -\mu_o \mu_r \frac{\partial H}{\partial t} \qquad \text{Equation 1}$$

and $$\nabla \times H = J = \sigma E \ , \qquad \text{Equation 2}$$

where, H is the applied field which can be expressed as,

$$H = H_0 e^{i\omega t}(\bar{x}) \ . \qquad \text{Equation 3}$$

Combining Equations 1, 2 and 3,

$$\nabla \times (\nabla \times H) = -\sigma \mu_o \mu_r \frac{\partial H}{\partial t} \ . \qquad \text{Equation 4}$$

The field due to eddy currents can be expressed as [3]

$$\frac{\partial^2 H_x(z)}{\partial z^2} = i\omega\sigma\mu_o\mu_r H_x(z) \ . \qquad \text{Equation 5}$$

The solution to the above differential expression can be written as

$$H_x(z) = H_0 \frac{e^{(\frac{1+i}{\delta}z)} + e^{(-\frac{1+i}{\delta}z)}}{e^{(\frac{1+i}{2\delta}z)} + e^{(-\frac{1+i}{2\delta}z)}} \ , \qquad \text{Equation 6}$$

where the factor δ is a function of resistivity ρ, permeability $\mu_o * \mu_r$ of the material and the operating frequency f and is expressed as,

$$\delta = \sqrt{\frac{\rho}{\pi \mu_o \mu_r f}} \quad . \qquad \text{Equation 7}$$

From Equation 7, we can conclude that the field due to eddy currents can be minimized by using a material with optimum values of resistivity and permeability. The resistivity of the magnetic core can be either increased by using thin sheets of magnetic materials, known as laminations, or by using ferrites, both of which have low conductivity. However, use of these materials for the core affects the magnetic properties of the devices.

With the increasing efforts to minimize the eddy current losses in microelectromechanical systems (MEMS), there has been considerable research done in the development of Soft High Magnetic Moment (SHMM) materials [4].

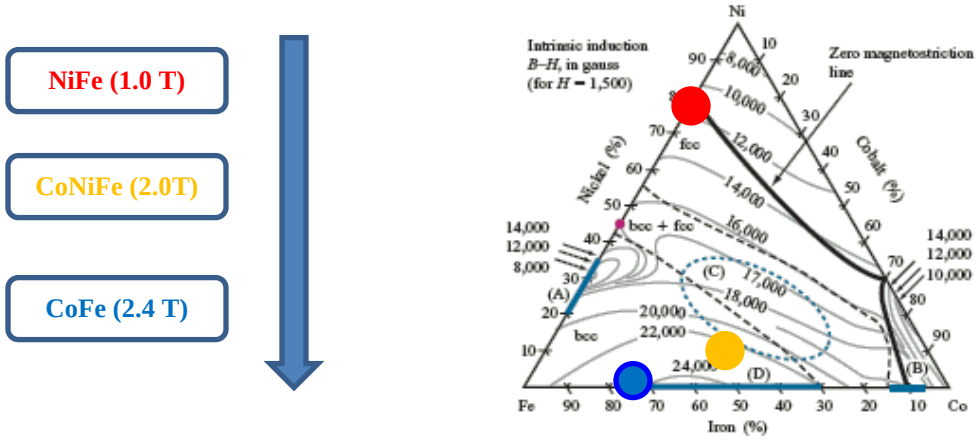

(a) (b)

Figure 2. (a) Trend in development of Soft High Moment Magnetic Alloys (b) Ternary Diagram explaining the composition of SHMM [4].

The need of a high resistive material with sufficiently high magnetic flux density has led researchers to investigate different magnetic alloys. Binary alloys like NiFe (1.0T) and CoFe (2.4T) shown in Figure 2a, were developed to yield high magnetic flux density but

failed to provide the high resistivity needed to minimize the eddy current losses. Hence, the primary focus of this research is to investigate the properties of ternary CoFeNi alloys, wherein inclusion of the third element in the alloy is expected to inherently improve its electrical resistivity. For applications in MEMS devices, the electrodeposited CoFeNi alloys also need to satisfy certain other properties such as low coercivity, low remanance, smooth and planar surface with low roughness exponent and low stress. Researchers in the industry, as well as academia, are facing the task of delivering SHMM thin films at nanoscale with the above mentioned properties [4, 5]. In order to obtain magnetic alloys with low coercivity, different additives have been used in the design of the electrodeposition solutions. The general action of additives is expressed through the leveling and brightening of the deposit, improved crystal structure, refined grain size and lower residual stresses [5]. Furthermore, this dissertation will cover the study of the effect of incorporation of saccharin on the electrical, magnetic and crystallographic properties of the electrodeposited CoFeNi alloys. The inclusion of saccharin in the electroplating solution also contributes in minimizing the overall stress in the CoFeNi alloys. Hence, the effect of saccharin incorporation on the grain size, as-deposited stress (pre annealing) and final state stress (post annealing) of electrodeposited CoFeNi thin films is investigated in this research.

1.3. Resistivity control in Cu Nanostructures

Many in the semiconductor industry did not believe that copper could replace aluminum even though limitations of aluminum were obvious. Scaling down of the device features resulted in the need to change the conducting material used for interconnects in integrated circuits. In 1997, IBM introduced a breakthrough in

semiconductor technology with the development of smaller, faster, more powerful and less costly integrated circuits using copper wiring in place of traditional aluminum shown in Figure 3 [6]. This was indeed a groundbreaking technological advance which has been governing the semiconductor industry for decades.

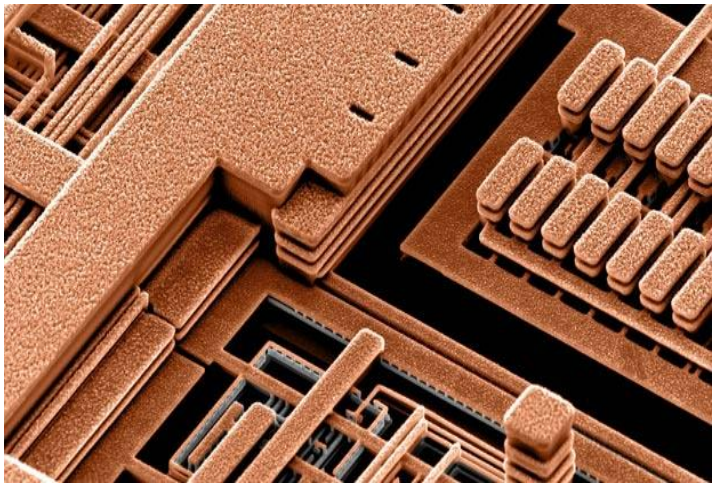

Figure 3. Replacement of Aluminum with Copper Interconnects, IBM 1998 [6].

With the downscaling of devices, the current density in interconnects increases to the order of 10^4 A/cm^2. The scattering from the atoms in such a high current density leads to the directional flow of electrons. The enhanced atomic displacement under the influence of the electric field is known as electromigration [6]. A thin film interconnect in a device can carry a high current density facilitating electromigration. Copper has a higher electromigration resistance than aluminum and hence, replacement of aluminum with copper improved the reliability of interconnects [7]. Copper also offered an opportunity to add more layers of interconnects using a radically different manufacturing process. IBM had to develop new fabrication techniques to build chips with copper.

With the advance in technology and the sophistication of the fabrication methods, the size of the Cu interconnects for future device/chip is shrinking down with critical dimensions of a few tens of nanometers. At this level, the conductivity of the Cu interconnects needs to be improved to maximize their performance and reliability. Properties and characteristics of interconnects are strongly dependent on the Cu grain microstructure and orientation. The average grain size, the distribution of the grains and grain orientations in the Cu interconnects; largely affect their performance and functionality. The Cu grains in the interconnect have a grain size which scales with the trench width [8]. The total strain in these interconnects, ε_0 is a summation of intrinsic and thermal strains. The initial (intrinsic) strain in these Cu grains, ε_i before annealing Cu interconnects is a function of the plating process, trench size and choice of deposition parameters. The change in deposition process parameters to minimize ε_i is not possible due to the crucial importance of the superfilling effect during the fabrication process. Strain due to annealing (thermal strain), ε_{th} can be controlled by annealing temperature and the choice of substrate. Changing the annealing temperature or substrate requires a major alteration in the device fabrication process.

The idea behind the proposed research is to control the value of strain, ε_0, by externally applying a controlled curvature on the wafer with Cu interconnects. One of the easiest ways is to deposit, on the opposite side of the wafer, a material having thermal coefficient of expansion such that the strain induced is sufficient enough to satisfy the criteria for grain boundary densification [8]. The thermodynamics of grain boundary densification and grain growth are shifted to favorable conditions with the help of

externally induced strain in the Cu interconnects [8]. The grain boundary area per unit volume will decrease during annealing, and conductivity of the Cu in trenches will be improved. The externally imposed curvature ε_{rr} can be easily measured using the state of art optical system based on cantilever bending method for stress/strain measurements. Hence, the second part of this dissertation focuses on the implementation of the proposed idea of 'strained annealing' and studying its effect on the resistivity of Cu interconnects.

1.4. Organization of the Dissertation

This dissertation is organized in the following chapters:

Chapter 1 is an introduction to the dissertation. The focus of this chapter is to educate the reader with the motivation behind this research and provide a brief summary of the proposed research. This chapter discusses the progress in development of soft high moment magnetic alloys and emphasizes the need for the study of the ternary CoFeNi alloys for the applications in MEMS devices. It further explains the trend in semiconductor technology and replacement of aluminum with copper for the use as a material for interconnects in electronic circuits. The chapter 1 concludes by proposing a novel approach of 'strained annealing' for the improvement of conductivity of Cu interconnects at nanoscale.

Chapter 2 gives an overview regarding the fundamentals of thin film electrodeposition by explaining the current-potential relationship during the thin film growth. This chapter further explains the electrodeposition of magnetic alloys emphasizing in particular the key concept of anomalous co-deposition applicable in electrodeposition of soft high moment magnetic (SHMM) alloys. The chapter 2

concludes by discussing the several factors contributing to the electrodeposition process of SHMM alloys.

Chapter 3 discusses the effect of additive incorporation on the mechanical and metallurgical properties of the electrodeposited CoFeNi alloys. By providing a reasonable explanation for the need of additives in electroplating solutions, the chapter provides a brief overview of saccharin as an additive and the mechanism for its incorporation in the deposit. The chapter 3 concludes by describing the effect of saccharin incorporation on the properties of the electrodeposited CoFeNi alloys.

Chapter 4 deals with the fundamentals of electrical resistivity and the factors affecting this physical characteristic at nanoscale. The chapter further provides an overview of the electrical properties of the SHMM alloys and the factors contributing to the same. The chapter 4 concludes by giving a detailed overview of the resistivity control in Cu nanostructures mainly used in electronic circuits.

Chapter 5 discusses the various experimental methods and setups designed for the material characterization and fabrication of the electrodeposited CoFeNi thin films and the Cu nanostructures. The basic principles underlying the working of the instruments and the construction of the experimental setups are described briefly in this chapter.

Chapter 6 enumerates the results for the characterization of electrodeposited CoFeNi alloys. This section also discusses the effect of saccharin on the properties of the CoFeNi thin films and signifies the additive effect on deposition stress by describing the in-situ stress measurements of the electrodeposited CoFeNi alloys. The latter part of the chapter deals with the model developed for resistivity measurements followed by the results obtained from sophisticated magnetic moment measurements. The chapter 6

concludes with microprobe measurements on interconnect samples which help to understand the effect of strained annealing on the resistivity of Cu interconnects.

Chapter 7 is the concluding part of the dissertation and it also lists some of the possible future work in this area that can aid in better improving the conductivity of Cu interconnects at nanoscale.

CHAPTER 2

ELECTRODEPOSITION OF SOFT HIGH MAGNETIC MOMENT ALLOYS

2.1. Introduction

Micro/Nano Electro Mechanical Systems (MEMS/ NEMS) devices are finding abundant applications in the semiconductor and magnetic industries due to their low power consumption and high reliability coupled with novel capabilities. MEMS devices such as microactuators, sensors and micromotors require the use of both soft and hard magnetic materials because electromagnetically actuated MEMS have proven to be more stable for high frequency applications [4]. There are many ways to deposit and integrate magnetic materials into MEMS/NEMS. Electrochemical processes like electrodeposition and electroless deposition are well suited to fulfill the requirements of high yield and cost effective processes. Electrodeposition has many advantages, including low energy requirements, room temperature and room pressure operations, high deposition rates, low cost, simple scale up and the ability to deposit structures with complex geometries. In addition, the properties of the materials deposited can be tailored by controlling the solution composition and deposition parameters. Due to these advantages, electroplated soft magnetic materials such as NiFe and CoFeNi have been widely used as recording materials for hard drives. This chapter revises the electrodeposition fundamentals by discussing the electrode kinetics in a typical electrodeposition experiment. The phenomenon of anomalous codeposition governing the iron group alloys is explained with suitable references acknowledging work done by previous researchers to explain the

codeposition of Ni, Fe and Co to form the an alloy [4,5]. In addition, the effect of plating parameters such as current density, plating solution, pH and substrate material on the electrodeposition process is explained in detail.

2.2. Electrodeposition - Fundamentals

Unlike many conventional methods of thin film deposition, the field of electrodeposition of magnetic materials exhibited a great development over the past few decades. Indeed, within the last ten years, the intensity of activity and applications in this area has reached its peak. Electrodeposition or electroplating is a process to coat the desired material from the electrolytic solution on a conductive substrate by passing a current through the solution [9]. The electrolytic solution contains positively charged ions (cations) and negatively charged ions (anions). Under the effect of an external electric field, cations migrate to the negatively charged electrode i.e. cathode and undergo reduction to form a deposit. Similarly, metal from the anode is oxidized into the solution to maintain the electrical neutrality.

To conduct such an electrodeposition experiment, a minimum of two electrodes is required. The electrode where the potential is applied for charge transfer to and from the electrolyte is called as the working electrode. A second electrode acts as the other half of the cell. This second electrode must have a known potential with reference to which the potential is applied at the working electrode. Furthermore it must balance the charge added or removed by the working electrode. While this is a feasible setup, it has a number of shortcomings. Most significantly, it is extremely difficult for an electrode to maintain a constant potential while passing a current to counter redox events at the working electrode. To solve this problem, the role of supplying electrons and referencing

the potential has been divided between two separate electrodes [9, 10]. The reference electrode is a standard half-cell with a known reduction potential. Its only purpose in the setup is to act as a reference in measuring and controlling the potential of the working electrode and not to pass any current. The auxiliary electrode popularly known as the counter electrode passes all the current needed to balance the current measured at the working electrode. The working, reference and counter electrodes make up the modern three electrode electrodeposition system as shown in Figure 4.

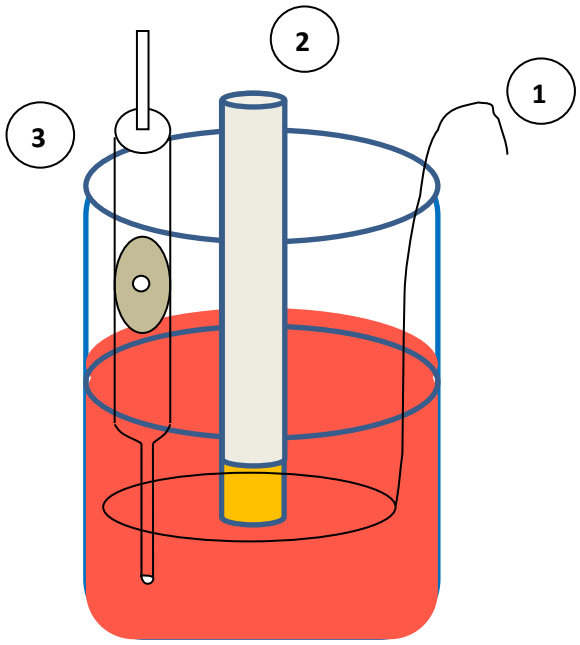

Figure 4. Three electrode electrodeposition set up (1) Counter electrode (nickel) (2) Working electrode (Au) (3) Reference electrode (SCE)

2.3. Current – Potential Relationship

The study of electrode kinetics is very essential to determine the dependence of the current on the potential during an electroplating cycle. Let E be the potential applied between the working and the reference electrodes in Figure 4 and I be the current flowing

in the circuit. Curve ‘a’ in Figure 5 represents the dependence of potential on the current when the electrodeposition process is controlled by the kinetics of the reaction alone. Curve b takes into account the effect of mass transport [10].

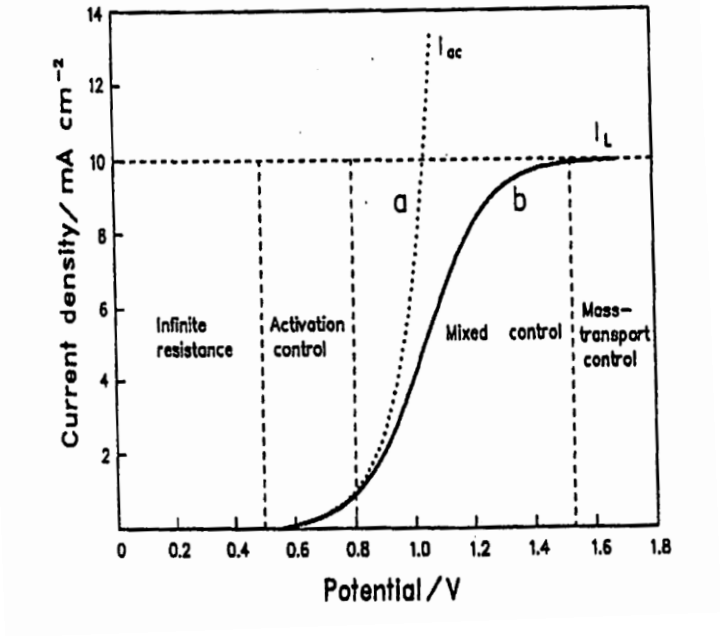

Figure 5. Current vs. Potential plot for the electrolysis of a dilute (0.01M) KI solution in H_2SO_4 using two Pt electrodes. The minimum potential for current flow is 0.59V [10].

As explained in the previous section, the potential E is measured versus a fixed reference potential and the current flow is measured between the working and the auxiliary electrode. From Figure 5, it is quite obvious that the current-potential relationship during an electrochemical deposition does not follow the widely accepted Ohm’s law. It is observed that up to a certain potential, the current is zero. This is not a matter of limited sensitivity of the measuring instrument but can be contributed to the infinite resistance at the metal-solution interface. The electrode kinetics could be explained by the transition from electronic to ionic conduction and the phenomenon associated with controlling this

process. Conduction in the solution is ionic, whereas in the connecting wiring it is electronic [10]. The transition from one mode to the other requires charge transfer across the interfaces which are controlled by the catalytic properties of the electrode surface, the chemisorption of the species, concentration of the electrolytic solution and the potential applied [10]. The rate of charge transfer between the interfaces can be accelerated using a right potential difference with an appropriate polarity. The exponential rise of the current with potential in the initial part of the curve in Figure 5 is governed by the charge transfer or activation controlled reaction. The horizontal part of line 'b' in Figure 5 represents the mass transport limitation. The deposition rate depends on the electrode potential and the electrolyte concentration given as [10],

$$\gamma_C = \frac{i_C}{nF} = k_C \cdot (C^s_{M^{n=}})^{P^M} \qquad \text{Equation 8}$$

and

$$k_C = k_{C,0} \cdot \exp(\frac{-\alpha_C F}{RT} \cdot E). \qquad \text{Equation 9}$$

The parameters in the Equation 8 and Equation 9 are defined as follows: γ_C is the reduction rate, i_C is the reduction current, n is the number of electrons transferred, F is the Faraday's constant (96485 C/mol), k_C is the reaction rate constant, $k_{C,0}$ is the rate constant value at zero potential, $C^s_{M^{n=}}$ is the surface concentration of the cation, P_M is the reaction order of the cation and $\frac{-\alpha_C F}{RT}$ is the Tafel slope describing the relation between kinetics of the reaction and potential applied [9,10]. The above two equations help us understand the relation between current and the applied potential. The overpotential η is

defined as the difference between the applied potential E and the equilibrium potential $E_{M^{n+}/M}$ which can be explained using the Nernst equation,

$$E_{M^{n+}/M} = E^{\theta} + \frac{RT}{nF}\log[(a_{M^{n+}})]. \qquad \text{Equation 10}$$

In Equation 10, E^{θ} is the equilibrium potential of an electrode at standard conditions (P^0 = 101kPa, T^0=298K) and $a_{M^{n+}}$ is the activity of species at the electrode surface with the reaction stoichiometry; positive for oxidized species and negative for reduced ones [9]. From Equation 9, we can conclude that the reduction reaction is under kinetic control when the applied over potential is low. The electrode surface concentration of the metal ions is same as the bulk concentration ($C^s = C^b$), when the potential applied is low and the current-potential dependence is linear [10]. When the overpotential becomes too negative, electrodeposition is mainly controlled by mass transfer. The surface metal ion concentration is less than in the bulk ($C^s < C^b$) and a gradient of ions is through the diffusion layer. As the surface concentration drops to zero, the concentration gradient reaches the maximum and the reaction rate cannot increase any further. This situation describes complete transport control and the current at which this occurs is called the limiting current [9, 10]. The equilibrium reversible potential (E^{θ}) is a characteristic property of every specific element. The more negative the value of E^{θ}, the less noble is the metal and it is very difficult to reduce the metal cation [9, 10]. The following table shows the E^{θ} for Nickel, Cobalt and Iron metals, constituents of magnetic alloys for different applications in the magnetic recording industry:

Table 1. Standard Reduction Potentials [10]

Metal	Electrochemical Reaction	Standard Equilibrium Potential (V) vs. SHE
Fe	$Fe^{2+} + 2e^- \longrightarrow Fe$	-0.44
Co	$Co^{2+} + 2e^- \longrightarrow Co$	-0.277
Ni	$Ni^{2+} + 2e^- \longrightarrow Ni$	-0.233
O_2	$O_2 + 4H^+ + 4e^- \longrightarrow 2H_2O$	1.229
H_2	$2H^+ + 2e^- \longrightarrow H_2$	0
H_2O	$2H_2O + 2e^- \rightarrow H_2 + 2OH^-$	-0.828

2.4. Electrodeposition of Magnetic Alloys

Electrodeposition of magnetic alloys is extremely advantageous compared to other vacuum deposition techniques. Hence, electrodeposited magnetic alloys are widely used in the recording industry due to their low cost production. Electrodeposition of iron group alloys has always been of much industrial interest due to the superior magnetic properties exhibited by the alloys which are highly essential for magnetic read-write heads [3, 4, and 11]. The electrodeposited soft magnetic alloys used in magnetic recording technology represent binary NiFe, CoFe and ternary CoFeNi alloys with different atomic percentages of Fe, Co and Ni. The percentages of Fe, Co and Ni in the alloy depend on the application in the magnetic recording industry. The common rule for designing the electroplating bath is that if the alloy needs to be rich in an element, for example Ni, then the plating solution should have the highest concentration of Ni^{2+} ion

[4, 11]. However, the ratios between the metals in the alloy and their ions in the solutions are never the same and hence, it is necessary to design an effective bath chemistry for electrodeposition of soft magnetic alloys. Hessami and Tobias [12] assumed hydrolysis product ions ($NiOH^+$, $FeOH^+$, $CoOH^+$) to be the dominant reactive species and explained the pH dependence on the following reactions. The steps in electrodeposition of Ni and Co are presented below, (M= Co, Ni)

$$M^{2+} + H_2O \rightarrow M[OH]^+_{ads} + H^+, \qquad \text{Equation 11}$$

$$M[OH]^+_{ads} + 2e^- \rightarrow M^0_{dep} + (OH)^-, \qquad \text{Equation 12}$$

and $$M^{2+} + 2e^- \rightarrow M_{dep}. \qquad \text{Equation 13}$$

If the pH of the plating solution is low (pH<2.5), the dominant pathway for Ni and Co deposition is described by Equation 13. At higher pH values (pH>3), a major part of the Co and Ni deposits according to Equation 11 and Equation 12 [4]. The kinetics of the steps in Equation 11 and Equation 12 are considered slower as compared to the direct metal reduction given in Equation 13, which implies faster deposition rates for Ni and Co at lower solution pH values. However, at lower pH values, the H^+ concentration increases which leads to dominant hydrogen evolution as a parallel reaction [4]. Hence, experimentally we observe lower deposition rates for Co and Ni for low pH values. However, the deposition of Fe occurs through a slightly different pathway as shown below,

$$Fe^{2+} + H_2O \rightarrow Fe[OH]^+ + H^+, \qquad \text{Equation 14}$$

$$Fe[OH]^+ + e^- \rightarrow Fe(OH)_{ads}, \qquad \text{Equation 15}$$

and $$Fe[OH]^+ + H^+ + e^- \rightarrow Fe_{dep} + H_2O. \qquad \text{Equation 16}$$

The formation of adsorbed Fe hydroxide on the metal surface is a slow process and is considered to be the rate limiting step in Fe deposition. The increase in the pH of the solution increases the kinetics of this step which overall increases the deposition rate of Fe [4]. These two effects of pH are observed by an overall increase in the deposition rate of the soft magnetic alloys and simultaneous increase of the Fe atomic percentage in the deposit. For this reason, the effects of pH on Co, Ni and Fe deposition have to be considered in relation to the pH value at the electrode – surface interface rather than the function of pH in the solution.

One of the most important phenomena influencing the plating solution design for electrodeposition of soft magnetic alloys is known as Anomalous Codeposition. This term was first introduced by Brenner [13] to describe the preferential deposition of the lesser noble metal in a binary system such as NiFe, NiCo and ZnNi. Among these binary alloys, the electrodeposition of NiFe alloy was widely studied to investigate this phenomenon. Ideally, it was expected that the more noble metal nickel would deposit faster than iron for an applied overpotential. However, it was found that the deposition process for nickel was 'retarded or slowed' whereas iron deposition was 'favored' in the alloy. As a result of this anomaly, the ratio of the less noble metal (Fe) to the more noble metal (Ni) is much higher in the deposits than in the electrolyte. Figure 6 shows the comparison of reduction potentials for Co, Ni and Fe with respect to standard hydrogen reduction potential.

Dahms and Croll [14] were the first ones to put forward an explanation for anomalous codeposition in NiFe binary alloys. Their model assumes that the hydroxide and hydroxyl ions discharge at the electrode surface. The pH associated with the iron

hydroxide adsorption on the electrode surface is relatively high. Iron hydroxide is adsorbed on the surface even before it is reduced. These adsorbed iron hydroxide sites act as inhibitors for the nickel reduction reaction and hence, lower nickel concentration in the deposit than in the solution is obtained [14].

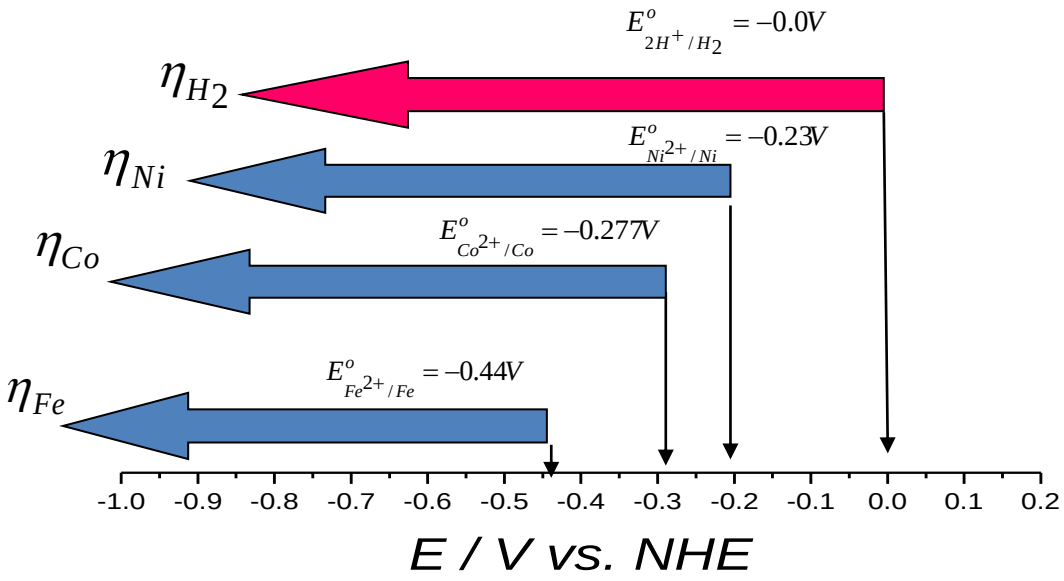

Figure 6. Standard reduction potentials for Fe, Co, Ni and H_2

Romnkiw [15] measured the surface pH during electrodeposition of nickel and iron both when deposited as single metals and as an alloy over a variety of conditions. Surface pH was found insufficient for metal hydroxide precipitation and the monohydroxyl ion (MOH^+) was proposed to be the species discharging at the electrode surface. Grande and Talbot [16] put forward a one-dimensional model explaining the discharge of monohydroxyl species on the electrode surface. This model explained that

the number of monohydroxyl species at the electrode surface depends directly on the deposition of the metal and is not dominated by any adsorption processes.

Matlosz [17] proposed a two-step mechanism in which nickel and iron are deposited as single metals. He believed that the metal ion is adsorbed and deposited on the electrode surface as a monovalent intermediate ion in the first step. This intermediate ion is then reduced to the metal state in the second step. This model could also be extended for the codeposition of nickel-ion alloys. The preferential adsorption of iron monovalent intermediate due to difference in Tafel constants for electrosorption explains the inhibition of Ni [17],

$$M^{++} + e^{-} \rightarrow M^{+}_{j,ads} \qquad \text{Equation 17}$$

and $$M^{+} + e^{-} \rightarrow M_{dep}. \qquad \text{Equation 18}$$

Baker and West [18, 19] examined this model with data obtained by impedance spectroscopy and showed that it was in complete agreement with Maltosz model. While all previous models focused on the inhibition of one metal reaction rate by another, Zech et al [20, 21] developed a model which described the enhancement of less noble metal reaction by introducing a catalytic mechanism. In the first step, a mixed metal complex is adsorbed on the electrode surface. In the second step, the complex is further reduced. Instead of generating two single atoms, it produces an atom of less noble metal and simultaneously releases a bivalent cation of more noble species acting as catalyst. To do

$$M_1^{++} + M_2^{++} + e^{-} \rightarrow [M_2M_1]^{++}_{ads} \qquad \text{Equation 19}$$

and $$[M_2M_1]^{++}_{ads} + e^{-} \rightarrow M_{2,dep} + M_1^{++}. \qquad \text{Equation 20}$$

Similar to the binary alloys codeposition, Zhuang and Podlaha [22, 23 and 24] explained the anomalous behavior of the CoFeNi ternary alloy system. The most noble metal (Nickel) deposition appeared inhibited whereas the least noble metal (Iron) deposition seemed to be enhanced as compared to the single metal (Ni, Co and Fe) depositions. Cobalt however, shows both catalytic and inhibited deposition effects depending on the potential range of the deposition. The deposition rate for Co is enhanced when the catalytic effect by Ni dominates and is suppressed when the inhibiting effect by Fe prevails. . High surface coverage by less noble Fe species is responsible for inhibited Ni and Co deposition rates. The deposition rate of Co lies between the most enhanced species, i.e. Fe and most inhibited species Ni. Their model assumes the formation of mixed metal intermediate species similar to Zech et al [20, 21] as explained earlier. Mixed metal intermediate species $FeCo(III)_{ad}$ and $FeNi(III)_{ad}$ are usually accounted for the enhanced Fe deposition rate and inhibited Ni and Co rates during the CoFeNi ternary alloy deposition. In order to predict and control the deposited alloy composition, the influence of metal concentration on the partial current densities needs to be understood. The rate determining feature of the ternary alloy deposition can be further explained with the detail understanding of the inhibition and enhancement effects on the deposition [24].

2.5. Effect of Electroplating Parameters

2.5.1. Electroplating Bath

An electroplating aqueous solution contains cations of the metal to be plated, anions to create suitable deposition conditions, buffers, additives and complexing agents for special purposes. The cations (metal ions) exist in the bath mainly as solvated ions and are present in higher concentrations. When a high cathode current is applied, a cation

depletion region occurs in the area near the electrode which is replenished by ion diffusion from the bulk solution [9, 10]. The diffusion rate is dependent on the difference in concentration between the bulk solution and depletion region. In the alloy electroplating, the composition of the deposit depends on the concentration of cations in the depletion region. Methods like agitation and pulse plating increase the concentration of the cations near the cathode surface influencing the depletion layer which indirectly affects the composition of the deposit [9, 25]. Of the three cations of main concern in this work, cobalt and iron (ferrous) ions are more readily reduced than nickel in the systems generally used for magnetic codeposition. Thus, the ion ratios of Co or Fe to Ni are kept small relative to the atom ratio desired in the deposit [4, 25].

The most commonly used anions are chlorides, sulfamates, hypophosphites and cyanides. The selection of the anion depends on the specific properties desired for the bath. For example, sulfamates are reported to plate with higher current efficiency as compared to chlorides resulting in less hydrogen evolution at the cathode. Chlorides minimize the anode dissolution problem which might occur with high nickel content electrodes [26]. Anions also affect the physical properties of the deposit such as internal stress, grain size and grain orientation. However, these effects can be countered by including suitable additives in the plating bath and therefore, the choice of anions in the plating solutions is usually not critical.

Additives are both organic and inorganic compounds. Their roles include wetting agents for better cathode and anode behavior, leveling, brightening, complexing and stress reduction [4, 26]. A great deal of study has been made of the activity of agents which level and brighten. These effects have not been of great direct concern in magnetic

material plating, and thus will not be taken up in this report. Wetting agents have been found to be most beneficial in reducing cathode pitting by increasing the tendency of the bath to wet the cathode thus removing hydrogen bubbles when they form. A similar action at the anode, especially, if oxygen is formed there is beneficial. Common wetting agents such as sodium lauryl sulfate (SLS) have been used to perform this task. Citrates, boric acid, ammonium chloride act as buffers to regulate the pH during electrodeposition. Complexing agents like sulfo –salicylic acids are used to keep the ferric ions coordinated in the solution thereby allowing them to be harmlessly deposited at the cathode. Thus, a complexing agent in the solution promotes the electrodeposition of an alloy with higher iron content with increased brightness and leveling [26]. Of all the additive actions, probably the one most beneficial for the electroplating of magnetic materials is that of the stress reducers. Because these materials not only reduce stress but simultaneously change crystal size and orientation, brighten and sometimes level, they are of interest to both the fundamental and applied work in magnetic films [25, 26]. Saccharin is one of the widely used additives in plating solutions for magnetic materials which will be reviewed in detail in the future chapters.

2.5.2. Current Density

The current applied during electroplating is one of the crucial parameters in obtaining electroplated magnetic alloys. Previous work by fellow researchers has shown that the increase in current density during electroplating improves the current efficiency and enhances the rate of the deposition [25]. Metallurgical properties such as grain size and residual stress also depend on the plating current density. With regards to the metal deposition reaction, the Fe deposition rate is favored with increase in current density.

Hence, depending on the desired composition, deposition rate and yield of the electroplated films, the current density for the deposition is aptly chosen.

2.5.3. pH of the solution

As discussed in the section 2.4, the reaction kinetics for iron, cobalt and nickel are pH dependent. The upper limit of hydrogen ion concentration in the acid baths is dictated by the tendency of this ion to compete for the electrons at the cathode. Thus, at some minimum pH a sufficient concentration of hydrogen ions are present so that the plating current efficiency begins to drop noticeably with further pH decrease [4, 25]. The upper limit of pH is more difficult to define. In depositing iron alloys, unless complexing agents are added, the oxidation of ferrous ions is increased, ferric hydroxide precipitates and finally ferrous hydroxide precipitates as the pH is increased. The changes observed with pH change include alloy composition, crystal orientation and size, hydroxide inclusion and stress [25, 26].

2.5.4. Substrate

The substrate used for electroplating needs to be strictly conductive for the current to flow in the circuit. The choice of the substrate material becomes crucial in order to achieve electroplated magnetic materials with lower coercivity. Roughened surfaces have shown to yield films of higher coercivity and lower saturation magnetization [4]. Other factor determining the substrate selection is the stress during thin film deposition. Substrates which lead to a greater mismatch with the electroplated film usually lead to high stresses resulting in film peel off [4, 26].

CHAPTER 3

ADDITIVE INCORPORATION

3.1. Need for an additive

Soft high moment magnetic materials are particularly useful in magnetic storage devices due to their high saturation magnetization and low coercivities. The shrinking in the device size has stimulated the research in the development of new magnetic materials which demonstrate unique mechanical, electronic and magnetic properties [4]. Although numerous soft or hard magnetic films are being fabricated via sputtering, evaporation and casting techniques, most of them cannot be applied to device fabrication due to low deposition rate, high internal stress, overly thick films, and coarse-grained films [5]. The electrodeposition technique has major advantages over other methods of thin-film production such as possibility of performing deposition at normal conditions of pressure and temperature. In addition, it is a relatively easy and inexpensive technique with many parameters (current, potential, temperature, bath composition, and additives) that can be adjusted in order to obtain better quality deposits [4, 5]. At nanoscale, the reliability and performance of the magnetic devices becomes critically dependent on the properties of the electrodeposited magnetic materials, their stability in different fabrication steps and their compatibility with other materials used in fabrication process [4, 5]. These materials also need to satisfy certain other properties such as low coercivity, low remanance, smooth and planar surface with low roughness exponent and low stress. In order to obtain magnetic alloys with low coercivity, different additives have been used in design of the electrodeposition solutions.

Saccharin is an organic additive that has been widely used for more than three decades for electrodeposition of magnetic alloys such as NiFe, CoFe and CoNiFe. The lasting use of saccharin as an organic additive in the industrial production of magnetic alloys is due to its valuable properties such as stress reliever, grain refiner and a brightening agent of the deposit [26]. This chapter demonstrates a novel fabrication approach of soft magnetic materials via electrodeposition from a chloride bath containing additive sodium saccharin. Different mechanisms of saccharin adsorption and electroreduction have been explained followed by the effect of saccharin incorporation on the metallurgical properties of the electrodeposited magnetic alloys.

3.2. Mechanism of Saccharin Electroreduction

Saccharin is an organic molecule with benzene and heterocyclic rings in its structure. The molecular formula for saccharin is $C_7H_5NO_3S$ and has the structure as shown below,

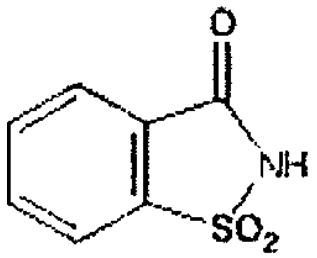

Figure 7: Saccharin Molecule [27]

During electrodeposition, saccharin is electroreduced to metal sulfides in four stages. In the first step, there is reductive cleavage of the C-S bond in saccharin molecule, Figure 8a, giving rise to benzamido sulfamate as indicated in Figure 8b. The carbonyl part (C=O) in the saccharin molecule acts as the electron withdrawing group and facilitates

the reductive cleavage of C-S bond [27]. The second step is desulfurization of the benzamido sulfamate, leading to protonated intermediate as shown in Figure 8c. This intermediate is then fragmented into sulfur dioxide and benzamide as in Figure 8d. The next step involves reduction of sulfur dioxide to hydrogen sulfide through six electrons and protons given by equation 8e. This conversion includes numerous chemical and electrochemical steps and could lead to formation of different intermediates like H_2SO_2, H_2SO_4, etc. [27]. Hence, the conversion from sulfur dioxide to hydrogen sulfide is the slowest step in the overall transformation and acts as the rate limiting step too. The last step is a fast reaction between hydrogen sulfide and the metal ions leading to metal sulfides which precipitate in the electrodeposited alloy presumably at the grain boundaries [26, 27]. The transformation of saccharin to sulfides is potential and pH dependent.

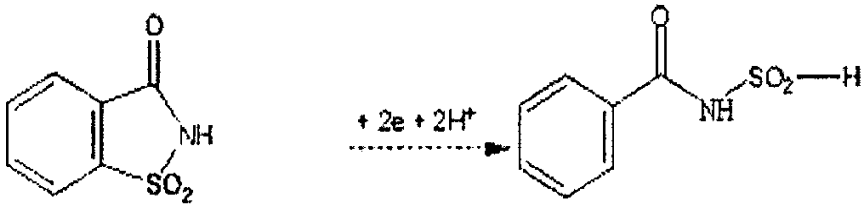

(a) (b)

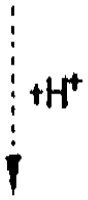

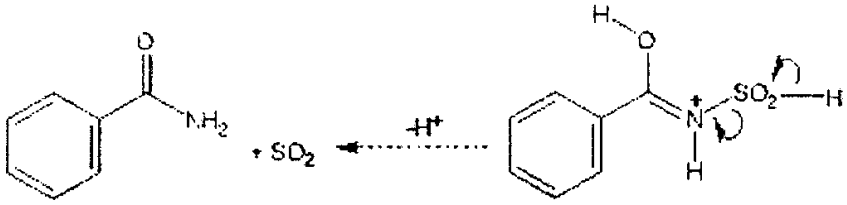

(d) (c)

$$SO_2 + 6e^- + 6H^+ \rightarrow H_2S + 2H_2O$$

(e)

$$H_2S + M^{2+} \rightarrow MS + 2H^+ \quad (M = Co, Ni, Fe)$$

(f)

Figure 8. (a) Saccharin molecule (b) Benzamido sulfinate (c) Protonated Intermediate (d) Sulfur Dioxide and Benzamide (e) Sulfur Dioxide Reduction to Hydrogen Sulfide (f) Metal Sulfide Formation [26, 27].

3.3. Mechanism of Saccharin Adsorption

Consider a situation when the electrode is maintained at potential other than potential of zero charge (PZC) and is attracting positively charged ions from the solution. The ions in the solution (ions in the solution are always assumed to be surrounded by water molecules, i.e. hydrated) experience a force pulling them towards the electrode surface. In short, when the applied potential is lower or higher than PZC, the electrode surface is densely packed with ions, water molecules and the net charge on the double layer is maximum. When an additive like saccharin is added to the solution, it has to compete with ions in the solution and water molecules to reach the electrode surface. The dipole moment of the saccharin molecule is very small [10, 26]. The force acting on a

dipole is proportional to its strength and hence saccharin molecule experiences lower forces when placed in an electrostatic field. To remove the ions or water molecule from the electrode, energy needs to be spent opposing the forces acting in the field. As every system tries to minimize the amount of energy spent, at potentials other than PZC, there is minimal or no adsorption of saccharin on the electrode surface [10]. Figure 9 depicts the electrode surface when applied potential (E) not equal to PZC.

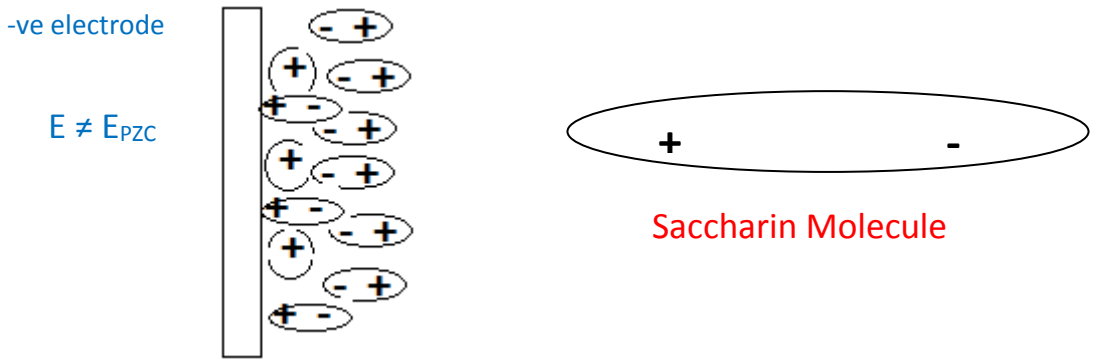

Figure 9. Electrode surface when potential not equal to PZC

When the applied potential is closer to the PZC, the electrostatic field is very weak or almost absent. The ions in the solution do not experience any force acting on them. The polarity of the water molecule near the electrode surface is also uncertain and hence water molecules are randomly oriented. The charge on the double layer in this case is almost zero. Now as there is no interaction between the electrode surface and the ions and water molecules, almost no energy is spent to separate them from the electrode surface. In this case, the saccharin molecule which had been struggling until now, easily manages to approach the surface and get adsorbed. Hence, when the applied potential is in a certain range close to PZC, saccharin adsorption is favored on the surface. The phase of

the saccharin adsorbed has a lower energy compared to phase of the saccharin molecule in water, because water molecule and the electrode surface have no interaction near PZC [5, 10, and 26]. More concentration of saccharin in the solution, denser layer of saccharin is adsorbed on the surface for the same range of potential near PZC. Figure 10 shows the electrode surface when potential is maintained near PZC.

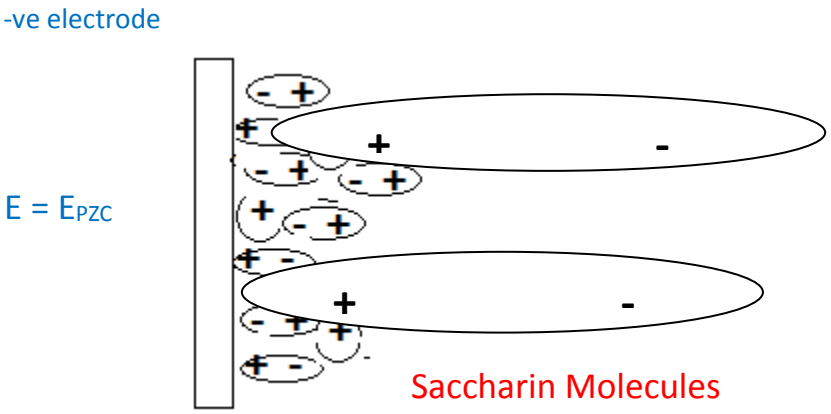

Figure 10. Electrode surface when potential equal to PZC

Hence, additive adsorption for saccharin is preferable when the electrode is maintained at PZC. Similarly, for other additives, the potential for adsorption would vary (E < PZC, E > PZC) depending on the molecular structure and the dipole moment [10].

3.4. Sulfur Incorporation Mechanisms

Consider electrodeposition of CoFe alloys from the plating solutions containing different concentration of saccharin. The sulfur incorporation into magnetic deposits from saccharin occurs either via saccharin adsorption – electroreduction or physical incorporation during the deposit growth as mentioned above. The first mechanism represents the chemical route by which saccharin is transformed into metal sulfides and

sulfur containing molecular fragments which get precipitated in the deposit [26, 27, and 28]. The electroreduction reaction of saccharin is a surface controlled reaction, whose rate can be calculated as,

$$\gamma_{ER} = kC_{Sac}^{S}, \qquad \text{Equation 21}$$

where k represents the reduction rate constant and C_{Sac}^{S} is the concentration of saccharin absorbed layer on the deposit surface [26]. This term can be further expressed as a function of saccharin coverage θ and surface concentration of the saccharin full monolayer Γ_{ML} as,

$$C_{Sac}^{S} = \Gamma_{ML} \cdot \theta \ . \qquad \text{Equation 22}$$

However, there is a possibility that not every atom of sulfur belonging to the initially electroreduced saccharin molecule gets incorporated into the deposit. Hence, while considering the contribution of sulfur due to electroreduction of saccharin, a factor χ is introduced as,

$$R_{ER} = \chi \cdot \gamma_{ER} = \chi \cdot k \cdot \Gamma_{ML} \cdot \theta . \qquad \text{Equation 23}$$

The second route represents the incorporation of entire molecules of saccharin having sulfur as an integral part [26, 27 and 28]. The physical incorporation of entire saccharin molecule in a deposit expressed in units of flux is defined as,

$$R_M = \frac{\Gamma_{ML} \cdot \Delta v}{d_{sac}} \cdot \theta(1-\theta), \qquad \text{Equation 24}$$

where Δv is difference in growth rate of the free deposit surface and growth rate of surface covered with saccharin, d_{sac} represents the diameter of saccharin molecule. In addition to additive related mechanisms, sulfur also gets incorporated due to entrapment of sulfur containing ions (SO_4, SO_3...) into the deposit [26]. Let the incorporation rate of

sulfur by this mechanism be noted as R_0. Now, the sulfur incorporation rates from all three mechanisms can be combined to calculate the total incorporation rate as [26],

$$R_T = R_0 + R_{ER} + R_M . \qquad \text{Equation 25}$$

Considering equations (22), (23) and (24), we can rewrite the equation (25) as,

$$R_T = R_0 + \chi \cdot k \cdot \Gamma_{ML} \cdot \theta + \frac{\Gamma_{ML} \cdot \Delta\nu}{d_{sac}} \cdot \theta(1-\theta) . \qquad \text{Equation 26}$$

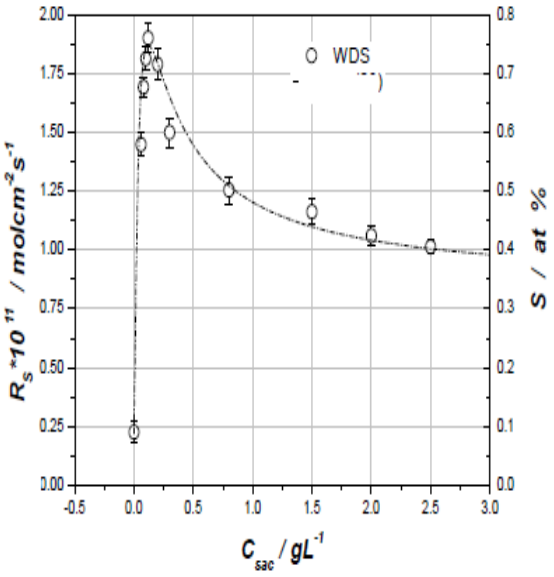

Figure 11. R_s (R_T) vs. C_{sac} dependence for direct current deposition of 2.4 T CoFe alloys. On the right ordinate, the corresponding atomic % of S in the deposit is indicated [26].

The saccharin adsorption can be expressed in terms of Langmuir formalism,

$$\theta = \frac{b \cdot C_{sac}}{1 + b \cdot C_{sac}} . \qquad \text{Equation 27}$$

The final form of the sulfur incorporation rate (R_s) as a function of saccharin concentration in the solution can be expressed as,

$$R_T = R_0 + \chi \cdot k \cdot \Gamma_{ML} \cdot \frac{b \cdot C_{sac}}{1 + b \cdot C_{sac}} + \frac{\Gamma_{ML} \cdot \Delta\nu}{d_{sac}} \cdot \frac{b \cdot C_{sac}}{(1 + b \cdot C_{sac})^2} . \qquad \text{Equation 28}$$

Hence, we can conclude from equation 28 that the total rate for saccharin incorporation in the deposit is a function of saccharin concentration, diameter of the saccharin molecule, adsorption constant, thickness of monolayer of saccharin and sulfur entrapment rate.

3.5. Effect of Saccharin on Deposition Rate

Several mechanisms have been proposed to explain the effect of additive incorporation on the rate of metal reduction during electrodeposition of magnetic alloys. However, these mechanisms differ not only from one metal to another but also due to the electrodeposition conditions and additives present. One of the direct methods to observe this effect is by measuring the current efficiency. Current efficiency of an electrochemical deposition reaction as given by equation 29, is the ratio of the charge during dissolution (Q_a) to the charge during deposition (Q_c) [4] expressed as

$$\%\eta = \frac{Q_a}{Q_c} * 100 \ . \qquad \text{Equation 29}$$

Ideally, the efficiency could be considered close to one. However, due to the hydrogen evolution reaction occurring simultaneously, some amount of the cathodic charge is used up [10, 26]. Hence, the net cathodic charge for deposition is not equal to the charge for metal reduction, but also account the charge used up for the hydrogen evolution reaction and is given as,

$$Q_c = Q_M + Q_H \ . \qquad \text{Equation 30}$$

Hence, we need to calculate the current efficiency. Empirical observations by research groups have showed that the current efficiency of metal reduction increases in the presence of additives in the electroplating bath.

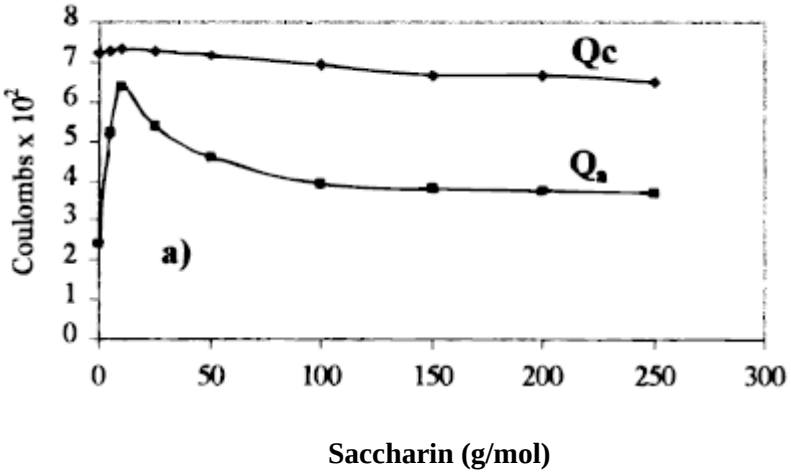

Figure 12. Effect of saccharin concentration on charge during electrodeposition (Q_c) and dissolution charges (Q_a) [27].

The presence of the additive shifts the potential for parasitic hydrogen evolution reaction cathodically and suppresses the hydrogen evolution. Figure 12 shows the charge transients for deposition and dissolution charges for an electrochemical deposition and stripping experiment. The ratio of Q_a to Q_c will yield us the efficiency corresponding to the concentration of saccharin in the electroplating bath. Figure 13 shows the effect of different additive concentrations on the current efficiency. Deposition rate can be calculated from the current efficiency as,

$$R = \frac{\eta * j}{2 * F * \xi} * 100 \ , \qquad \text{Equation 31}$$

where j is the current density (mA/cm^2) for the electrodeposition, F is the Faraday's constant (96485 C/mol) and ξ is the molar volume (mol/cm^3) [10, 28]. Increase in the efficiency of the electrodeposition results in faster metal deposition rate. For depositing thick films (> 500nm), electrodeposition thus serves to be a cheaper deposition technique by intelligent use of additives in the plating solution.

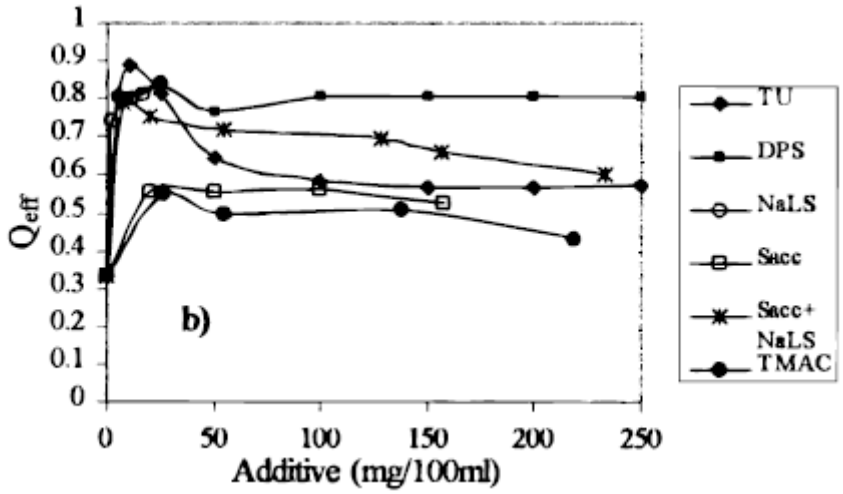

Figure 13. Effect of concentration of different additives on the current efficiency [27].

Hence, use of additives like saccharin in the electroplating solution helps in making the electrodeposition process far more convenient as compared to other conventional deposition processes like sputtering, evaporation and chemical vapor deposition.

3.6. Effect of Saccharin on the Stress during Electrodeposition

Recent trend in the magnetic recording systems indicate that the electrodeposited thin film magnetic materials are a material of choice for future magnetic devices and nanostructures [5, 29]. The general approach followed to electrodeposit high quality magnetic thin films with good properties is to incorporate different additives in the electroplating solution. Grain growth during thin film deposition or during annealing can play a dominant role in defining the microstructural properties of the thin film. Specifically, the yield stress of polycrystalline thin films increases with decreasing grain size and film thickness [30]. Hence, very thin and fine grained films have yield stresses of hundreds of MPa. This affects the performance and reliability of polycrystalline thin films with regards to application in devices and systems. Common practice indicates that

sulfur bearing additives are ideally effective as stress relieving agents during thin film growth.

3.6.1. Stress in thin Films

The thin film growth is characterized mainly by three different modes based on the affinity between the atoms of the substrate and the adatoms. According to literature, most of the polycrystalline film growth is characterized by the Volmer-Weber growth mode. Initially, the material deposits on the substrate in the form of small nuclei or clusters (popularly known as nucleation sites). These islands then grow and interact with each other, coalesce and establish aerial continuity [30, 31]. The polycrystalline films are formed through the sequence of steps as illustrated in Figure 14. Polycrystalline thin films have highly constrained grain structure. The grain geometry, average grain size and the distribution of grain orientations in polycrystalline films strongly affects their mechanical as well as other properties [31]. The stress evolution during thin film deposition can be explained with the help of a schematic as shown in Figure 15. The stress vs. thickness curve for most of the polycrystalline films follows a CTC (compressive, tensile and compressive) behavior. Region 1 in Figure 15 indicates the initial nucleation step, wherein the stress in the film is compressive in nature. The compressive stress can be explained by combination of two effects; firstly the surface stress acting on an unconstrained island induces equilibrium lattice spacing different than the bulk.

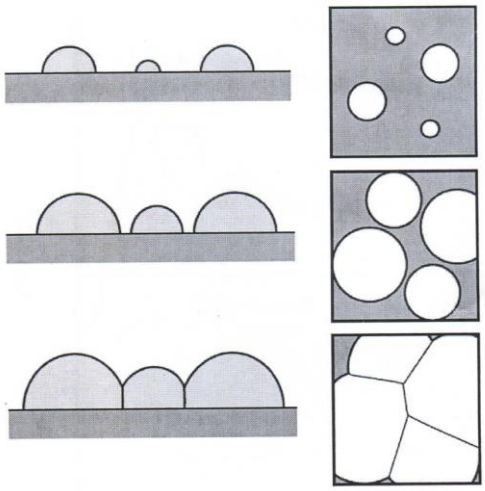

Figure 14. Nucleation, growth and coalescence to form a continuous thin film by Volmer Weber Growth [32, 33].

This difference in the force acting on the surface results in the stress being exerted on the substrate.

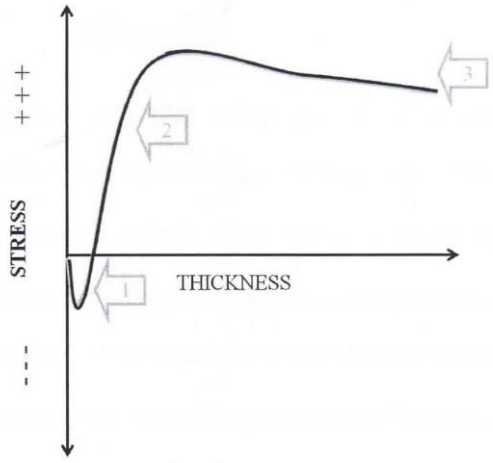

Figure 15. In- situ stress measured during thin film deposition as a function of the film thickness [30].

To maintain equilibrium, there has to be an internal stress acting within the crystallite which is assumed to be Laplace pressure ΔP, given as,

$$\Delta P = \sigma = \frac{-2f}{R}, \qquad \text{Equation 32}$$

where f is the surface stress R is the radius of the crystallite. Secondly, there is a maximum critical island size above which the island becomes impinged and does not affect the in-plane lattice spacing. As the deposition continues, the grain growth occurs by Volmer- Weber growth mode. As long as the radius of the crystallite is less than the critical radius (R_{crit}), the nucleation of new islands does not affect the internal stress [30, 31, and 32]. At a critical radius, the nucleus is locked down and the growth of the nucleus no longer affects the in-plane lattice spacing. Beyond the critical radius, strain due to mismatch of the lattice is prevented from relaxing. This strain produces traction at the film substrate interface leading to stress in the substrate given as [32],

$$\sigma = \frac{2f}{R_{crit}}\left(\frac{R_{crit}}{R} - 1\right). \qquad \text{Equation 33}$$

As the radius of the cluster grows larger, the ratio $R_{crit}/R \to 0$. Thus the compressive peak reaches maximum at $\frac{-2f}{R}$.

Region 2 in the Figure 15 corresponds to the tensile peak due to the island coalescence phenomenon. Nix and Clemens [33, 34, and 35] postulated that the islands continue to grow until they touch the adjacent island which eliminated the need for calculating the gap between the crystallites. They assumed that the crystallites instantly snap on as the grain boundary energy is less than the free surface energy. This process is known as the "zipping effect". Thus, the driving force for the coalescence is the minimization of energy [30, 33]. The tensile stress is then function of the average grain boundary formed, grain size, surface diffusivity and the growth flux. Freud and Chason

designed a model based on the Hertz contact theory, wherein they assumed that the islands were hemispherical in shape and all of the same radius R, arranged with center to center spacing of 2R [30]. These islands are initially formed with radii smaller than R, which gradually grow to reach R, thereby spontaneously forming cohesion areas between the islands leading to coalescence as shown in Figure 16.

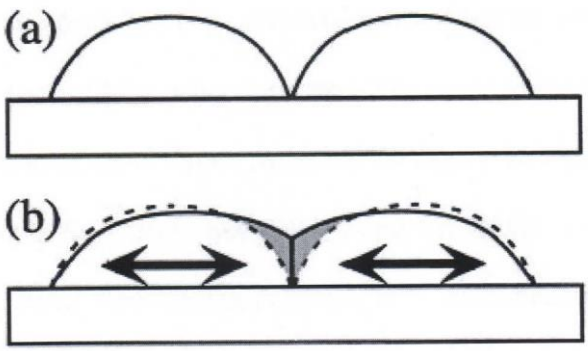

Figure 16. (a) Islands on the substrate (b) Tensile stress due to coalescence of islands during the zipping process [30, 32].

The tensile force generated due to the traction between the film and the substrate induces an average tensile stress in the film given as [5, 32],

$$\sigma_{avg} = \frac{4\Delta\gamma}{R} \qquad \text{Equation 34}$$

and $$\Delta\gamma = \gamma_s - 0.5\gamma_{GB} \ , \qquad \text{Equation 35}$$

where $\Delta\gamma$ is the driving force for the grain zipping process. It represents the difference between the free surface energy of coalescing grains and half of the energy pertaining to the grain boundary newly formed.

Region 3 in Figure 15 corresponds to the state of stress as the film deposition continues. The stress thickness dependence on the material type. Type1 materials are high

melting point or low adatom mobility refractory metals like Ti, W and Fe. The atoms having a low mobility, attach to the strained crystal at the point of arrival on the substrate, allow the crystal to grow in a strained state. In this case, the tensile stress increases with increase in the film thickness indicating columnar growth. Type2 materials are low melting point or high adatom mobility metals like Ni wherein the resulting film stress is compressive as the film thickness increases [32]. The high mobility helps the atoms to move freely to preferential sites which results in relaxation, causing a reduction in the stress. The preferential sites for the adatoms to incorporate are the grain boundaries. As the formation of grain boundaries results in elastically strained crystallites, these extra adatoms can deposit at the grain boundaries, reducing the stress.

3.6.2. Role of Saccharin

Additives adsorb on the electrode surface during electrodeposition and modify the thermodynamics of the nucleation process, grain structure and the grain boundary formation. Additives incorporate in the magnetic films in the form of a low surface energy phase such as sulfur related additives, molecular fragments or intermetallic compounds. Saccharin segregates at the grain boundaries affecting the specific energy and acting as stress reliever during the grain zipping process [4, 5, 36, and 37]. During electrodeposition, small amounts of hydrogen get incorporated in the deposit which is a known cause for post deposition tensile stress. Additive adsorption suppresses the hydrogen incorporation in the deposit, thus reducing the levels of tensile stress during deposition and aging.

For low surface mobility metals like Co and Fe, the maximum tensile stress is mainly during the grain zipping process resulting in the grain boundary formation. To

explain the effect of stress reduction due to additive incorporation, let's consider an example of electrodeposited CoFe alloy. Figures 17a and 17b show the schematics of the grain boundary zipping process for clean CoFe surface and saccharin covered CoFe surface respectively.

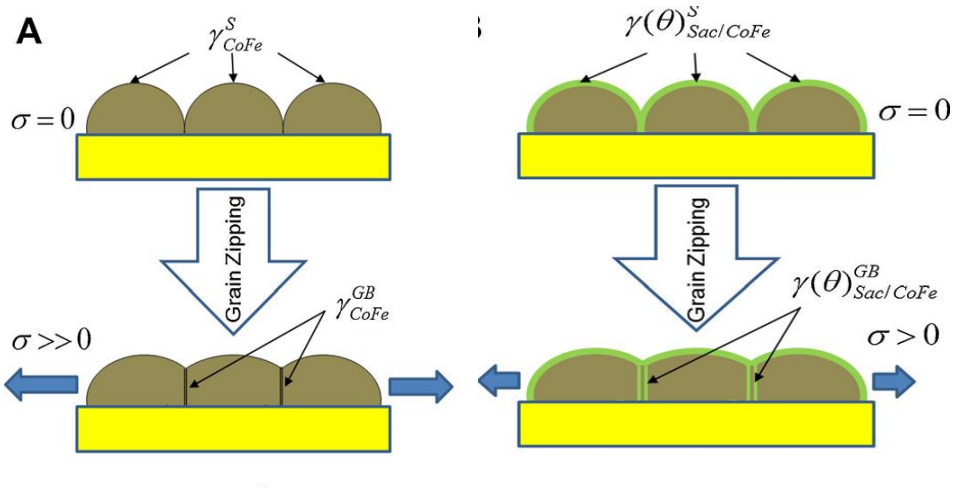

(a) (b)

Figure 17. (a) Grain zipping process for clean CoFe surface (b) grain zipping process for saccharin covered CoFe surface [5].

The value of the average maximum tensile stress is given as,

$$\sigma^{\max}_{avg,CoFe} = 8\frac{\Delta\gamma_{CoFe}}{d_G}, \qquad \text{Equation 36}$$

where d_G represents the average diameter of the grains while $\Delta\gamma_{CoFe}$ is the driving force for the grain zipping process [5]. The addition of saccharin to the plating solution significantly lowers the maximum tensile stress in the CoFe films as shown in Figures 18a and 18b. Saccharin which adsorbs on the growing CoFe surface modifies the surface

energy and grain boundary energy during the zipping process. The extent of this effect is dependent on the coverage of the adsorbed saccharin, θ.

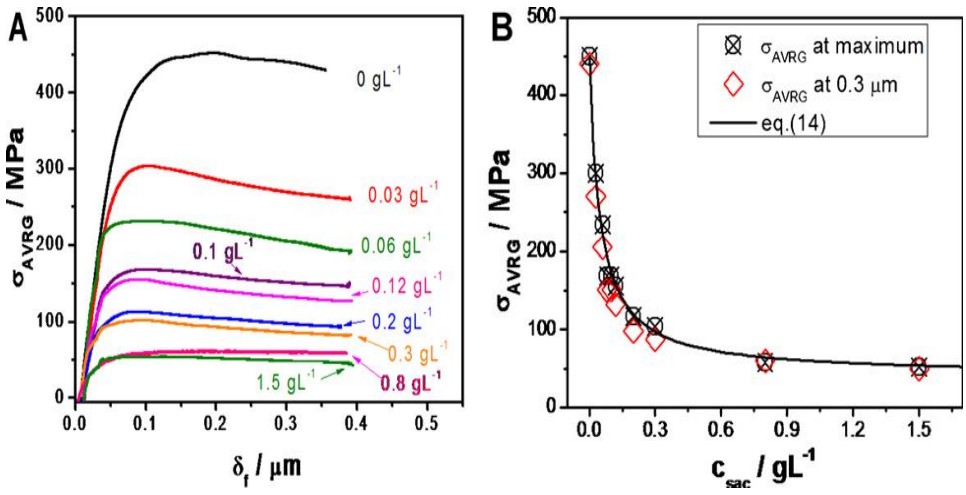

(a) (b)

Figure 18. (a) In-situ stress measurements (b) Maximum average stress and average stress at 0.3µm thickness a function of saccharin concentration in the solution [5].

The surface energy of the CoFe grains with adsorbed saccharin phase, $\gamma(\theta)^{S}_{Sac/CoFe}$ can be expressed as linear combination of the surface energy of the CoFe grains without adsorbed saccharin γ^{S}_{CoFe} and surface energy of the CoFe grains with maximum saccharin coverage $\gamma^{S}_{Sac/CoFe}(\theta=1)$ as [5],

$$\gamma(\theta)^{S}_{Sac/CoFe} = \theta \cdot \gamma^{S}_{Sac/CoFe} + (1-\theta) \cdot \gamma^{S}_{CoFe}. \qquad \text{Equation 37}$$

Considering the same analogy, the energy of grain boundaries formed after zipping process of the grains with arbitrary saccharin coverage $\gamma(\theta)^{GB}_{Sac/CoFe}$ [5],

$$\gamma(\theta)^{GB}_{Sac/CoFe} = \theta \cdot \gamma^{GB}_{Sac/CoFe} + (1-\theta) \cdot \gamma^{GB}_{CoFe}. \qquad \text{Equation 38}$$

Here, the term $\gamma^{GB}_{Sac/CoFe}$ represents the energy of the grain boundary formed by zipping two CoFe grains with maximum saccharin coverage $(\theta = 1)$. We can define the driving force for zipping process of CoFe grains with arbitrary coverage (θ) of saccharin [5],

$$\Delta\gamma(\theta) = \gamma(\theta)^{S}_{Sac/CoFe} - \frac{1}{2}\cdot\gamma(\theta)^{GB}_{CoFe}. \qquad \text{Equation 39}$$

Substituting equations 37 and 38 in equation 39,

$$\Delta\gamma(\theta) = \Delta\gamma_{CoFe} - \theta\cdot(\Delta\gamma_{CoFe} - \Delta\gamma_{Sac/CoFe}). \qquad \text{Equation 40}$$

Here, the term $\Delta\gamma_{Sac/CoFe}$ represents the driving force for grain zipping process where saccharin coverage of the grain surface is maximum. Thus, we can conclude that the driving force for zipping process with adsorbed saccharin is a strong function of saccharin coverage. Combining equations 36-40, the final form for the analytical model for the maximum tensile stress in electrodeposited CoFe films can be represented as [5],

$$\sigma^{\max}_{avg}(\theta) = \sigma^{\max}_{avg,CoFe} - 8\frac{\Delta\gamma^{*}}{d_G}\cdot\theta \ . \qquad \text{Equation 41}$$

Here, $\Delta\gamma^{*}$ is the difference in the driving force for zipping of CoFe grains with saccharin free surface and CoFe grains with maximum coverage of adsorbed saccharin phase (θ=1). For practical purposes, it is convenient to express the saccharin coverage as a function of saccharin concentration in the solution. Brankovic et al [5, 34] have used Langmuir adsorption formula to represent saccharin adsorption on the CoFe surface,

$$\theta = \frac{B\cdot C_{Sac}}{(1 + B\cdot C_{Sac})}, \qquad \text{Equation 42}$$

Here, B is the equilibrium adsorption constant and C_{Sac} is the saccharin concentration in the solution. Combining equations 41 and 42, the final expression for the model can be written as [5, 36, and 37],

$$\sigma_{avg}^{\max}(\theta) = \sigma_{avg,CoFe}^{\max} - 8\frac{\Delta\gamma^{*}}{d_G} \cdot \frac{B \cdot C_{Sac}}{(1 + B \cdot C_{Sac})} \quad . \qquad \text{Equation 43}$$

The extracted value of $\Delta\gamma^{*}$ from the model fits the data well and is smaller than $\Delta\gamma_{CoFe}$, which implies that the adsorbed saccharin phase significantly lowers the driving force for the grain zipping process. The CoFe surface with adsorbed saccharin molecules is likely to have surface bonds saturated by adsorption process reducing the CoFe surface energy. However, the grain boundaries formed during the zipping process of CoFe surfaces covered with saccharin have higher grain boundary energy as compared to grain boundary formed during the zipping process of clean CoFe surface [5, 36, and 37]. Therefore, we can conclude that the impact of saccharin on stress reduction is thermodynamic in nature.

3.7. Effect of Saccharin on Coercivity

Soft magnetic materials have become an important aspect of the modern electrical and electronics technology through their ability to concentrate and shape the magnetic flux with greater efficiency. Magnetic materials are termed “soft”, if they have lower coercivity, i.e. the critical field strength to flip the direction of magnetization [4]. The substitution of the conventional materials by the soft magnetic materials has demonstrated the reduction in the core losses leading to the improved device efficiency. Soft magnetic materials are a central component of electromagnetic devices such as stepper motors, magnetic sensors and read-write magnetic heads. Fabrication and

processing of these devices using thin film technology helps to extend the use of soft magnetic materials to more sophisticated technologies. Scaling down the size of these devices requires materials that can develop high saturation flux density, B_s, so that the necessary flux densities can be preserved even after reducing device dimensions while simultaneously achieving lower coercivity [4, 5, and 36]. Common high Bs soft magnetic films currently in use are electroplated CoFe and CoFeNi alloys. The favorable properties are achieved by incorporating organic additives in the electroplating solution, which also typically reduce the internal stress during electrodeposition.

There are many authors who have tried to explain the effect of additive incorporation on the coercivity of the electrodeposited magnetic films. The use of saccharin as an additive in the electroplating solution for CoFe, NiFe and CoFeNi alloys has been widely studied by many groups. The typical data showing CoFe alloy coercivity dependence on saccharin concentration is shown in Figure 19a. Brankovic et al [36] have reported a different dependence from one studied for NiFe and CoFeNi films. Rather than monotonous decrease in coercivity (H_c) for an increasing the saccharin concentration (C_{sac}), a more complex dependence is observed as shown in Figure 19a. The largest value of H_c is obtained for CoFe films electrodeposited from saccharin free solution. A small addition of saccharin in the electroplating solution shows a significant decrease in H_c. The lowest coercivity is achieved for a certain threshold concentration of the saccharin concentration ($0.12gL^{-1}$), after which an increasing saccharin concentration results in CoFe films with higher H_c values. The initial decrease in the coercivity can be attributed to the reduction in stress levels during the electrodeposition of CoFe with small additions of saccharin in the electroplating solution. The reduced stress levels result in smaller

contribution of magnetoelastic anisotropy energy to the total anisotropy energy thereby leading to electrodepositing lower coercivity CoFe films [36]. However, with increasing saccharin concentration beyond a particular threshold, the coercivity of the CoFe films increases. This cannot be related to the stress related to magnetic anisotropy energy change. The apt explanation for this effect could be the additive incorporation mechanism during electrodeposition of the magnetic alloy.

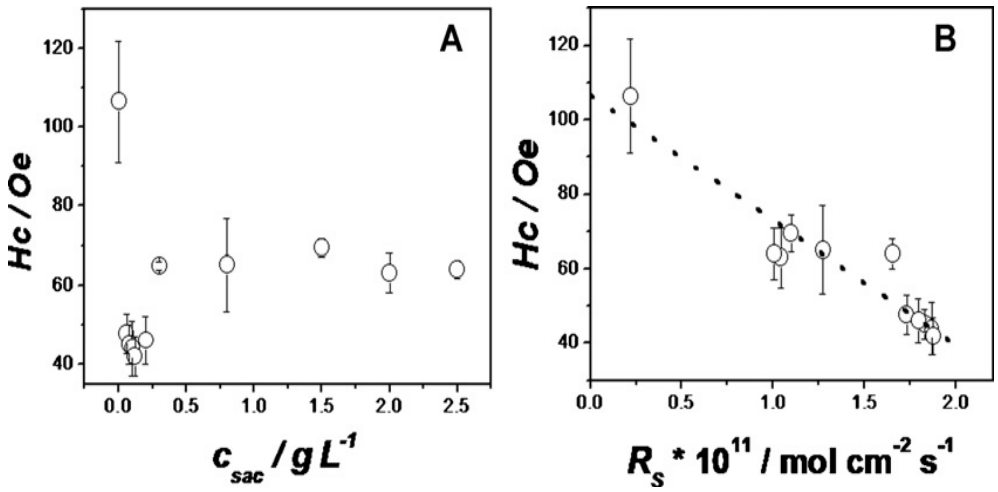

(a) (b)

Figure 19. (a) Coercivity of the electrodeposited CoFe alloy as a function of saccharin concentration in the solution (b) Coercivity of the electrodeposited CoFe alloy as a function of the sulfur incorporation rate [36].

The magnetic decoupling of the grains due to the additive related precipitation at the grain boundaries is an antagonistic effect on coercivity of the CoFe films. The two opposite effects of saccharin on the coercivity of CoFe films result due to the observed dependence of coercivity on the average as deposited stress leading to an optimum value of saccharin concentration producing the CoFe films with the lowest coercivity values [36]. Figure 19b explains the dependence of the coercivity of the CoFe films on the sulfur

incorporation rate coming from saccharin incorporation phenomenon. From this analysis, it is obvious that the higher incorporation rates of the sulfur decrease the CoFe alloy's coercivity [36].

Similar to the study of saccharin incorporation on the magnetic properties of the electrodeposited CoFe alloys, Tetsuya et al [37] carried out similar experiments to study the additive incorporation effect on electrodeposited CoFeNi alloys.

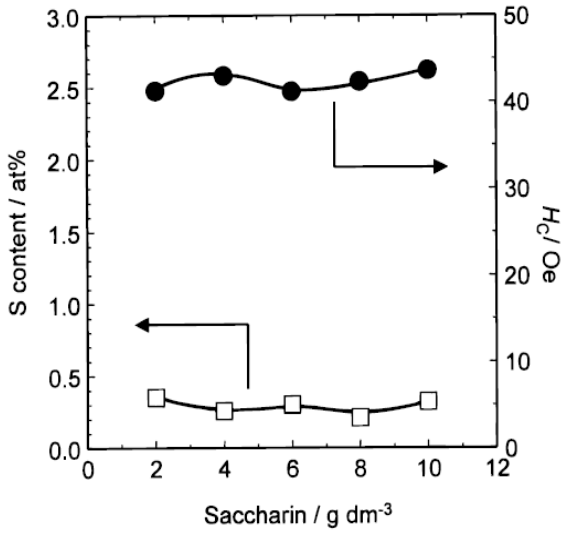

Figure 20. Sulfur content in the electrodeposited alloy as a function of saccharin concentration [37]

Figure 20 shows the dependence of coercivity and sulfur percentage in the deposit on the saccharin concentration in the electroplating solution. With the increasing saccharin concentration in the electroplating bath, the sulfur content in the deposit was invariantly consistent at 0.3±0.005 atom% whereas the coercivity was nearly constant at 42±2 Oe [36, 37].

CHAPTER 4

RESISTIVITY CONTROL IN MAGNETIC FILMS AND COPPER NANOSTRUCTRUES

The electrical resistance or resistivity of a conducting material can be experimentally determined without much difficulty. For many years, it has been used as a research tool to study various microstructural and physical phenomena. However, unlike conventional techniques which are capable of mapping out scattering intensities in two or three dimensional space, the electrical resistivity measurements give a single value representing an average over all directions of conduction electron scattering. As there is no means of performing the back-transform from the average value, the analysis of the resistivity data must include all factors contributing to the resistivity of the material [38]. These include the conduction electron scattering at the surface, from grain boundaries, interfaces and from the impurities in the crystal lattice. Such studies make use of the sensitivity of the conduction electron scattering process to the atomic level and provide a more convenient analysis of the resistivity over the volume of a sample. The electrical properties of metals and their alloys are of great practical importance especially in applications involving heating, temperature measurement, signal and power transmission, switching devices, semiconductor and thin film devices. However, understanding the physical processes that determine the electrical resistivity of metals and metallic alloys is a daunting task because of the large number of possible contributions that could be involved [38]. This chapter explains the phenomenon of electrical resistivity in solids and the parameters contributing to the same. It further discusses the effect of additive

incorporation, annealing and grain growth on the resistivity of the electrodeposited magnetic alloys and copper nanostructures.

4.1. Motivation of study

It has been long known that the resistivity of a conductor increases sharply as its dimensions are comparable to the electron mean free path which is the average distance that an electron travels before it is scattered by lattice thermal vibrations (phonons). The importance of this effect to polycrystalline metal interconnects in silicon technology was first identified in 1988 by Chen and Gardner [39]. Their observation had a major impact on the microelectronics industry as shown in Figure 21.

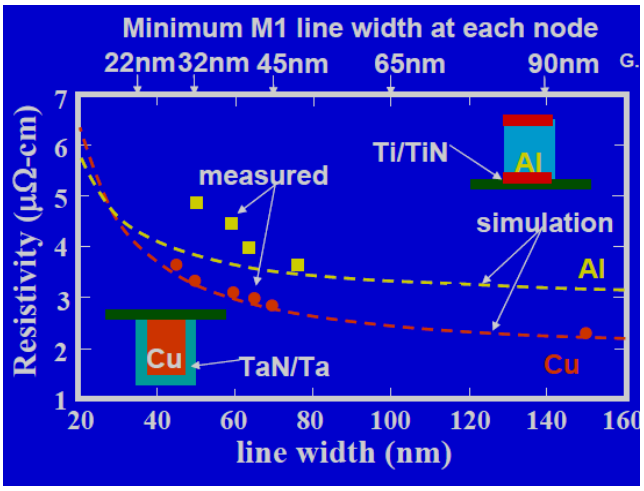

Figure 21. Effect of device scaling on resistivity [39]

The ITRS (International Technology Roadmap for Semiconductors) predicts that the typical line width for the first layer of wiring in the back-end-of –the-line interconnects will be 32nm in 2014 and the grain size effect is expected to cause a 2X increase in the line resistivity [40, 41]. Such an increase in line resistivity will severely limit the

interconnect conductance and negatively impact the integrated circuit performance [42, 43]. Further, as the microelectronics industry scales the Metal 1 Wiring Pitch towards 64nm by 2014, the need to overcome the resistivity size effect becomes more urgent [44]. Consequently, the size effect in Cu conductors has been identified by ITRS as "Grand Challenge" problem to be solved in this decade. To enable optimum scaling of high performance nano-interconnects for VLSI applications below the 45nm design node, it is important to gain insight into the physical origin of the conductivity degradation.

4.2. Phenomenon of Electrical Conduction

The Boltzmann transport theory is a useful context for understanding the basic of electrical conduction in metals and will be discussed in brief. Within a metal, the conduction electrons at the Fermi surface are moving at the Fermi velocity, which is 1.57 x 10^6 m/s in Cu [44]. Electrons at lower energy states within the Fermi surface are also moving, but at lower velocities. As all of the electrons are moving in all possible directions, the net velocity of the distribution of the electrons is zero (i.e. for each electron moving to the left, there is a comparable state with an equal probability of an electron moving to the right). In momentum space, the shape of the Fermi surface is commonly assumed to be spherical (this is a reasonable approximation for Cu) as depicted in Figure 22a. If the metal is subjected to an applied electric field, all of the electrons will accelerate at a constant rate and the net effect would be an indefinitely increasing displacement of the Fermi sphere to the opposite direction. However, at room temperature, the lattice vibrations in metals (phonons) or impurities and other defects scatter the electrons between states and result in a net shift of electrons from the non-equilibrium higher energy states on the right edge of the shifted sphere into the lower

energy states on the left edge on the shifted sphere, acting to restore the Fermi sphere to its equilibrium condition [44, 45]. As a result of this scattering, the extent of the shift of the Fermi sphere does not increase indefinitely and reaches a steady state condition where the effect of electric field to shift of the sphere is balanced by the electron scattering events as shown in Figure 22a. The steady state net current that results from the displacement of the Fermi sphere is a result of the electrons on the right edge with positive x-axis momentum not being matched by electrons in occupied states on the left edge. Qualitatively, for the same applied electric field, less frequent scattering (weaker restoring force) allows a greater steady state shift of the Fermi sphere and hence, a greater net electric current.

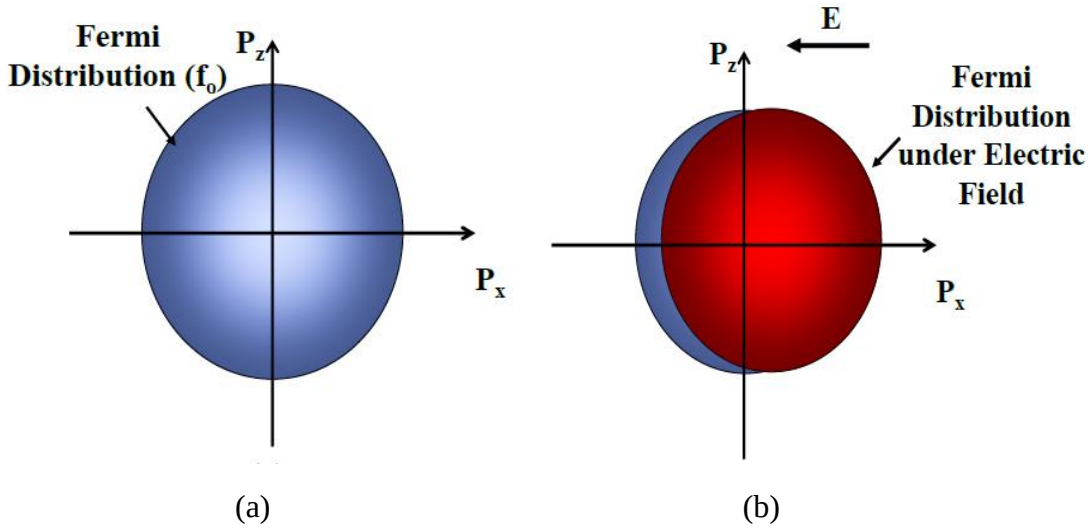

Figure 22. Schematic of the Fermi surface (a) under no electric field (b) under an electric field [39].

Thus, a material's electrical conductivity can be related to shape and density of state near its Fermi surface, and the extent to which the Fermi surface may be shifted in the presence of an electric field. When the electric field is turned off, the Fermi sphere will

be returned to its original equilibrium position by the electron scattering (as shown in Figure 22a) and the net current will cease [39, 1, 2]. Quantitatively, this model of transport of electrons in metals is commonly described by the Boltzmann Transport as expressed in Equation 44 as

$$\frac{\partial f}{\partial t} = -v_x \frac{\partial f}{\partial z} + \frac{q\varepsilon_x}{h}\frac{\partial f}{\partial k_x} + \frac{\partial f}{\partial t}\Big|coll\,, \qquad \text{Equation 44}$$

where f is the Fermi distribution, t is time, v_x is the velocity of the electron along the x direction, ε_x is the electric field along x direction, k_x is the wave vector along the x direction and h is the Planck's constant and $\frac{\partial f}{\partial t}\Big|coll$ is the change of the Fermi distribution. The Fermi distribution is a function of the three electron momentum components and time. As a result, the Fermi distribution describes the states which are occupied or not and hence can be used to calculate the net current. At equilibrium in normal metals, the Fermi distribution is symmetric and there is no net current. Changes in the distribution function are driven by changes in electron concentration and kinetic energy, by the acceleration of the electrons due to an applied electric field and by scattering events. In steady state conditions, these effects necessarily balance and $\frac{\partial f}{\partial t}$ equals to zero.

4.3. Factors affecting resistivity of thin polycrystalline films

Thin metal films have received widespread attention for technical applications like conducting connections in microelectronics, optical elements or supported adsorbents in and informative quantity to characterize the material. K. Fuchs predicted in 1938 that the electrical resistivity of thin metal films increases with decreasing thickness [2]. The

scattering of the conduction electrons at the film surface was considered to be the factor responsible for this phenomenon. Initially, a significant experimental data was obtained to support the hypothesis and the interpretation was not questioned. Later, however, it became obvious that grain boundary scattering played a decisive role in the resistivity behavior of the polycrystalline thin films. The corresponding extension of the Fuchs' theory lead to the scattering hypothesis where not only surface scattering, but also the crystalline boundary scattering, surface roughness and adsorption phenomenon were taken into consideration [1, 2]. The scattering hypothesis is based on the assumption that Matthiessen's rule can be applied, i.e. all scattering contributions combine additively, given as [2],

$$\rho_T = \rho_0 + \rho_{GB} + \rho_{SS} + \rho_{SR} . \qquad \text{Equation 45}$$

With the grain boundary scattering contribution given as,

$$\rho_{GB} = \rho_0 \frac{K}{D} . \qquad \text{Equation 46}$$

The surface scattering contribution given as,

$$\rho_{SS} = \rho_0 \frac{C}{h} . \qquad \text{Equation 47}$$

And the surface roughness contribution given as,

$$\rho_{SR} = \rho_0 \frac{CB^2}{h^3} \ , \qquad \text{Equation 48}$$

where h is the film thickness and D is the grain dimension parallel to the plane of the film, ρ_0 is the bulk metal resistivity, K and C are the scattering constants and hence proportional to the mean free path (λ) of the electrons and B is a measure of the surface roughness. In the proceeding sections, each scattering mechanism will be discussed along

with a model explaining its contribution to the overall resistivity of the polycrystalline thin film [2].

4.3.1. Surface Scattering

The main factor contributing to the resistivity in metals at room temperature is the scattering of conduction electrons by phonons (lattice vibrations). This scattering results in the loss of the additional energy and the momentum the electron might have gained from an applied electric field; hence impeding the electron response to the applied field leading to metallic resistivity. The average distance that an electron travels between such scattering events is termed as the electron mean free path (λ). Electron scattering may also be contributed to impurities, linear and planar defects in the crystal lattice, grain boundaries and the conductor's external surfaces. As the smallest dimension of the conductor is reduced to the order of its electron mean free path, the electric field induced momentum loss due to scattering of electrons by the external surfaces of the conductor (or other defects) increases and gives rise to the classical resistivity size effect. Fuchs was the first to explain and model the effect in the context of scattering at the top and bottom surfaces of thin polycrystalline films [2]. Sondheimer later extended Fuchs' work to narrow metal lines [46]. Collectively, their theory of surface scattering is known as the Fuchs-Sondheimer (FS) model. This model is derived from the Boltzmann transport equations and takes into consideration all scattering events at the conductor surfaces (either specular or diffuse). The FS model assigns a fixed probability 'p' for specular scattering events to occur and '1-p' for diffuse scattering events. This specular scattering probability is the sole characteristic of the external surface considered by the model. In a diffuse scattering event, any additional field induced velocity of the electron is lost upon

collision of the surface and electron. In terms of the displacement of the Fermi sphere, diffuse scattering has a similar result to that of phonon scattering, in that electrons from the higher energy states of the shifted Fermi surface (right edge in Figure 22b) are scattered into lower energy states (left edge) and thus the net shift of the Fermi surface is reduced [1, 2]. However, it should be noted that the phonon scattering is effectively isotropic in polycrystalline metals, while diffuse scattering is not.

Specifically, if the external surface of the film is parallel to the x-y plane, then it can be expected that the diffuse scattering will affect the electrons with significant z-axis momentum while electrons with nearly zero z-axis momentum will travel parallel to the surfaces and only affect the surface infrequently [2]. In a specular scattering event, a conduction electron incident on the surface is reflected with no change in its energy while its momentum perpendicular to the plane of the film is reversed. In terms of the Fermi sphere, such scattering results in a change in the sign of electron's z-axis momentum, but does not serve to restore the position of the Fermi sphere to equilibrium as it does not change the x-axis momentum of electron momentum. Figure 23 shows the schematic of the conduction electron scattering when passing through a Cu interconnect. TaN/ Ta has been used as a barrier layer within a SiO_2 and Si_3N_4 matrix [47]. The blue arrows at the top of the Cu line illustrate the two possible scattering events at the surface. The electron incident on the surface is illustrated by the first dark blue arrow and specularly scattered electron trajectory is shown by the second dark blue arrow. The shorter light blue arrows pointing towards various directions are possible electron trajectories for the cause of diffuse scattering from the surface. Researchers have shown a noticeable increase in the

resistivity in thin films due to the diffusion surface scattering as explained by the FS model.

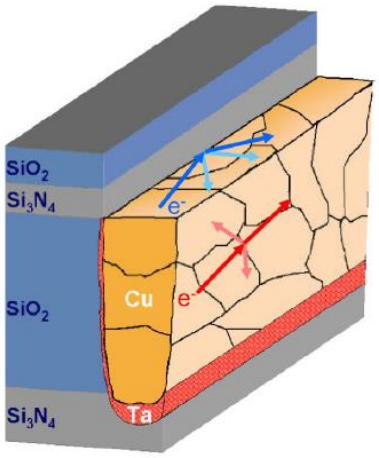

Figure 23. Schematic of e- scattering events through a Cu interconnect [47].

As the Cu interconnects become narrower, the number of surface scattering events increase and their contribution to the total conductor resistivity increases as shown in Figure 24 [40, 47]. Fuchs and Sondheimer's (FS) model of surface scattering, derived from the Boltzmann transport equation, considered a semi-classical approach of Somerfield's description in which electrons would have a limited mean free path as a result of phonon and impurity scattering. It is important to note the model is highly artificial and ignores the microstructural details and non-extreme cases of scattering at the surface. The FS model describes the resistivity (ρ_{FS}) of a thin film as [2, 47],

$$\rho_{FS} = \rho_i \left[1 - \left(\frac{3}{2k} \right) (1-p) \int_1^{\infty} \left(\frac{1}{t^3} - \frac{1}{t^5} \right) \frac{1-\exp(-kt)}{1-p\exp(-kt)} dt \right]^{-1}, \qquad \text{Equation 49}$$

where $k = \frac{h}{\lambda}$, p is the probability of the specular scattering and ρ_i is the bulk resistivity of the material.

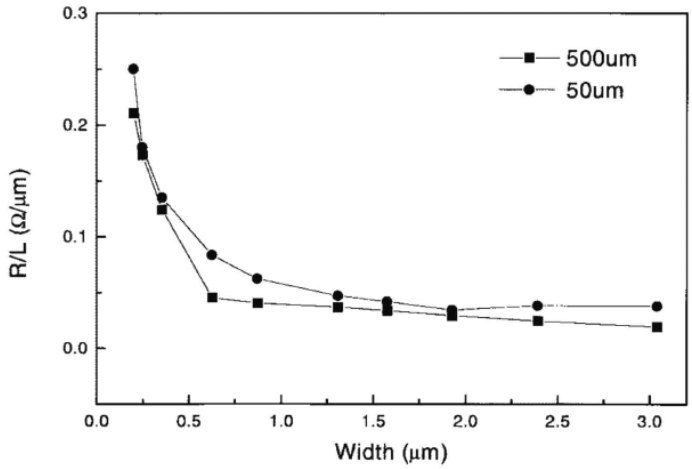

Figure 24. Increase in resistance with decrease in the Cu interconnect width [40].

At room temperatures, the bulk resistivity is primarily determined by the phonon scattering while at low temperatures (4.2 K), it is primarily determined by residual crystalline defects. By applying limits of *k* to the above Equation [49],

$$\rho_{FS} = \rho_i \left[1 + \left(\frac{3}{8} \right) \frac{\lambda}{h} (1 - p) \right]. \qquad \text{Equation 50}$$

Equation 50 is often used for the analysis of the empirical resistivity versus thickness (h) data. In this chapter, it is convenient to consider the resistivity increase predicted by this model as $\Delta\rho_{FS}$, given as $\Delta\rho_{FS}=\rho_{FS}-\rho_i$.

4.3.2. Roughness Induced Surface Scattering in Thin Films

The FS model uses the specular reflection probability, p, as a characteristic of the conductor's external surface that can be varied to fit the experimental data, but does not explicitly include the roughness of the surface. Soffer introduced a surface scattering

model that incorporates the contribution of surface scattering to calculate an angle-dependent specular reflection probability [48]. For a thin film with top surface (*1*) and bottom surface (2), having separate root mean square roughness *r1* and *r2*, the Soffer specular reflection probability for each surface is given by [48],

$$\left.\begin{aligned}\rho_1(\cos\theta) &= \exp\left[-\left(\frac{4\pi r_1}{\lambda_F}\right)^2 \cos^2\theta\right] \\ \rho_2(\cos\theta) &= \exp\left[-\left(\frac{4\pi r_2}{\lambda_F}\right)^2 \cos^2\theta\right],\end{aligned}\right\} \qquad \text{Equation 51}$$

where θ is the angle of incidence of the electrons to the conductor's surface and λ_F is the electron wavelength at the Fermi surface (about 0.5nm for Cu). The average specularity parameter for the top and bottom surfaces in the Soffer model is given as [48],

$$\overline{p\cos\theta} = \frac{1}{2}\left[p1(\cos\theta) - p2(\cos\theta)\right]. \qquad \text{Equation 52}$$

Soffer's resistivity model is expressed as,

$$\rho_{Soffer} = \rho_i\left[1-\left(\frac{3}{2k}\right)\int_0^1 \frac{\left(u-u^3\right)\left[1-\exp\left(-\frac{k}{u}\right)\right]\left\{1-\bar{p}(u)+\left[\bar{p}(u)-p_1(u)p_2(u)\right]\exp\left(-\frac{k}{u}\right)\right\}}{\left[1-p_1(u)p_2(u)\exp\left(-\frac{2k}{u}\right)\right]}du\right]^{-1},$$

Equation 53

Using this model, the increase in resistivity due to surface roughness induced scattering is thus,

$$\Delta\rho_{Soffer} = \rho_i - \rho_{Soffer}. \qquad \text{Equation 54}$$

More recently, Rossnagel and Kuan (RK) proposed a semi empirical extension of the FS model to include surface roughness explicitly [42]. Based on the Monte-Carlo simulations of electron trajectories near a rough surface, the resistivity model is given as,

$$\rho_{RK} = \rho_i + \Delta\rho_{FS}\left(1+\frac{r_1}{n}\right), \qquad \text{Equation 55}$$

where n incorporates the conductor thickness and the Fermi wavelength and is determined by the Monte-Carlo simulations of electron trajectories. This model continues to use the specularity coefficient of the FS model as a single fitting parameter and allows for larger resistivity increase than the FS model [42].

4.3.3. Grain Boundary scattering

For more than 30 years, the surface or roughness induced surface scattering were considered the only mechanisms contributing the classical size effect. In 1970, Mayadas and Shatzkes observed that the resistivity effect was more significant in polycrystalline conductors in comparison to that in single crystals [49, 50]. A more recent example of the same is shown in Figure 25 from the work of Rossnagel and Kuan [42]. It is evident that there is an additional 30% resistivity increase in polycrystalline Cu films deposited on SiO_2 over that of single crystal (100) Cu films deposited on (100) Si. Mayadas and Shatzkes (MS) explained and modeled this additional resistivity effect in terms of the grain boundary scattering, i.e. the grain boundaries in polycrystalline conductors can also scatter electrons and contribute to the film resistivity. When the grain size of the polycrystalline film is of the order of the electron mean free path, it may be scattered by the grain boundaries that separate crystals with different orientation in polycrystalline materials [49, 50]. Figure 24 shows an electron incident upon a grain boundary as a dark

red arrow and the transmitted emitted electron trajectory as a second dark red arrow. Transmitted electrons maintain their electric field induced momentum and hence do not contribute to the resistivity of the film. Reflected electrons lose their field induced momentum and contribute to an increase in the resistivity when the grain size of the film is reduced.

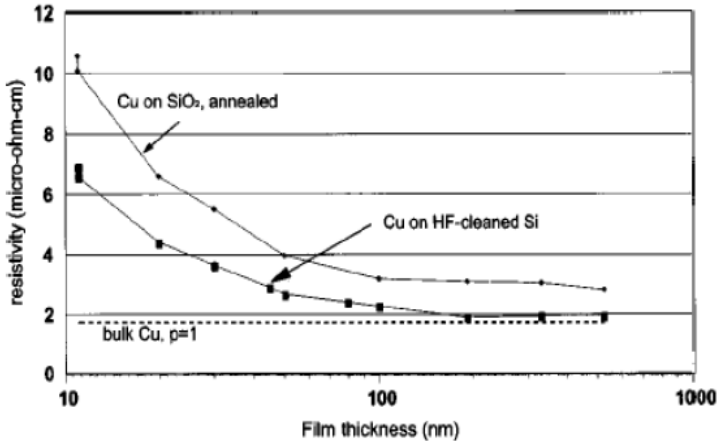

Figure 25. Electrical resistivity of Cu films as a function of thickness. Cu deposited on the SiO_2 is a polycrystalline film, while that deposited on HF cleaned Si is composed of large (100) oriented grains [42].

In terms of the Fermi sphere displacement, the reflected electrons are scattered similar to the electrons scattered by phonon, in that they are considered to be scattered from the high energy states (right edge in Figure 22b) to the lower energy states (left edge) and this serve to restore the equilibrium Fermi distribution. Grain boundary scattering is also not isotropic and as modeled, primarily scatters electrons with momentum components parallel to applied field.

Mayadas and Shatzkes developed an extension of the Boltzmann transport theory to include reflection and transmission of the conduction electrons at the grain boundaries of a polycrystalline metal [49, 50].

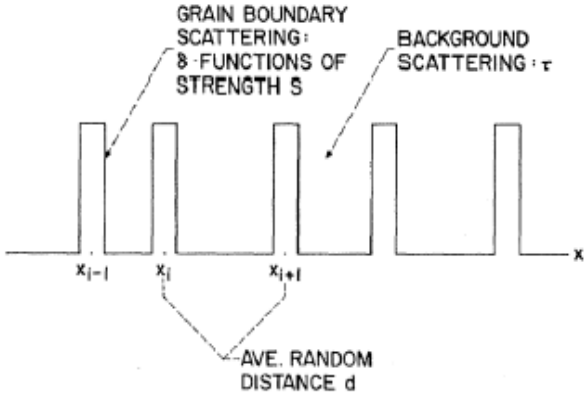

Figure 26. Schematic of Mayadas and Shatzkes (MS) where electrons are scattered by step potentials of strength S while grain boundaries parallel to the electric field only scatter specularly [49].

Their model assumes that grain boundaries are all either parallel or perpendicular to the direction of the current flow and that electrons incident upon the parallel grain boundaries are only specularly reflected, i.e. the parallel grain boundaries have no contribution to the resistivity effect. Each perpendicular grain boundary is treated as an internal surface, and when a conduction electron collides with the grain boundary, it has a probability of transmission or reflected quantified by a reflection coefficient R as shown in Figure 26. The coefficient is allowed to take values between 0 and 1 and is continuously varied to fit the experimental data. The important length scales for this model are the average grain size, g, and the electron mean free path (λ). The parameters R, g and λ are conveniently combined as [50],

$$\alpha = \left(\frac{\lambda}{g}\right)\frac{R}{1-R}. \qquad \text{Equation 56}$$

The Mayadas and Shatzkes (MS) model describes the resistivity (ρ_{MS}) of the film as [14],

$$\rho_{MS} = \rho_i \left[1 - \frac{3}{2}\alpha + 3\alpha^2 - 3\alpha^3 \ln\left(1 + \frac{1}{\alpha}\right) \right]^{-1} . \qquad \text{Equation 57}$$

In the limits of small α, Equation 57 is reduced to,

$$\rho_{MS} = \rho_i \left[1 + \frac{3}{2}\left(\frac{\lambda}{g}\right)\frac{R}{1-R} \right] . \qquad \text{Equation 58}$$

Using the MS model, the increase in resistivity due to the grain boundary scattering is,

$$\Delta\rho_{MS} = \rho_{MS} - \rho_i . \qquad \text{Equation 59}$$

Equation 51 and Equation 59 have the same fundamental form, namely

$$\rho(x) = \rho_i + \frac{A}{x}, \qquad \text{Equation 60}$$

where *x* is the experimentally varied size parameter (grain size or film thickness) and A is a constant, typically determined by fitting the experimental data [49, 50].

4.3.4. Impurity Scattering

In addition to the surface and grain boundary scattering, the resistivity of the polycrystalline films can be also increased due to the presence of impurities and voids. These impurities get incorporated mainly during the fabrication steps and get trapped near the grain boundaries. These impurity sites act as electron scattering units and lead to increase in the resistivity of the film. Higher concentration of impurities such as carbon (C), sulfur (S), oxygen (O) have been observed in spectroscopy results on polycrystalline thin films. A typical resistivity increase attributed to impurity scattering in a high purity (99.999%) Cu interconnect has been reported to be around 0.01μΩ-cm [49]. Voids are also observed in thin films which are mainly formed during the film processing and fabrication. While not directly affecting the resistivity, voids contribute to the errors in the measurement of sheet resistance used to calculate the resistivity experimentally [51].

4.3.5. Interface scattering and substrate effect

The contribution of the interface scattering to the resistivity of the material is usually neglected as it does not have a significant impact like the other scattering mechanisms. However, when the film thickness is of the orders of few nanometers, the scattering at the interfaces also contributes to the conduction electron scattering. Interfacial scattering is mainly caused due to the mismatch in crystal structure of two layers leading to interstitial and vacancy sites which scatter the conduction electrons [2].

While measuring the resistivity of a thin film (orders of a micron, thickness less than the distance between two probes in a four point probe head) deposited on a substrate, using the four point probe method, the seed resistivity also influences the thin film resistivity measurements. The current passed through the two probes of the four point probe head is divided into two layers; the thin film and the seed. The seed layer acts as a parallel resistor and shunts the resistivity of the thin film. Hence, it would be expected to see that the resistivity of a thin film measured on a copper seed is less than the resistivity of the same film measured on a Permalloy or tantalum seed.

4.4. Resistivity Control in electrodeposited magnetic alloys

Electrodeposition has been a feasible technique for fabrication of thin film magnetic recording heads [4]. An electrodeposited magnetic thin film with saturation magnetization (B_s) as high as 2.0 T, coercivity (H_c) < 2Oe and resistivity (ρ)> 20$\mu\Omega$-cm is an attractive candidate for write head core materials; thus meeting the demand of the tremendously increasing magnetic recording density [4, 5]. In order to meet the demand for high frequency recording, the electrodeposited magnetic alloy need to have a higher resistivity (ρ>100$\mu\Omega$-cm) along with high magnetization to minimize the eddy current

losses. For this purpose, several methods have been tried out to increase the resistivity of the electrodeposited alloys. This section discusses the effect of additive incorporation, ternary and quaternary alloy electrodeposition and annealing on the resistivity of the electrodeposited magnetic alloys.

4.4.1. Effect of additive incorporation on the resistivity

As explained in Chapter 3, additives like saccharin, Thiourea, EDTA etc. are introduced in the electroplating solution to minimize the stress during electrodeposition, to improve the softness of the magnetic alloy (lower coercivity) and yield a smooth, shiny surface of the electrodeposited magnetic thin film [27, 29]. For the application of these magnetic thin films in the magnetic recording industry, a higher resistivity film is needed to suppress the eddy current losses occurring at high frequencies. In these situations, the inclusion of additives in the electroplating solution has proven to be effective. The presence of additives in the electroplating solutions results in their incorporation into the magnetic deposit [52]. If the amount of additive incorporated is small, it is generally considered as beneficial to achieve the desired electrical and magnetic properties of the magnetic deposit. Osaka and colleagues studied the effect of additive incorporation on the resistivity of the electrodeposited CoFeNi alloys. A micron thin CoFeNi films were prepared by electrodeposition using a rotating disk electrode and a paddle cell. Additives such as Thiourea, saccharin, sodium glutamate, sodium citrate, sodium tartrate and EDTA were added in the basic bath as a source of impurity elements [53]. The electrical and magnetic properties were measured by the four point probe and the vibrating sample magnetometer respectively.

Figures 27a and 27b show the effect of sulfur containing additives on the electrical and magnetic properties of the electrodeposited CoFeNi thin films. An increase in the sulfur content in the deposit shows to increase the resistivity of the CoFeNi film by sacrificing its magnetic properties (reduction in the magnetization and increase in the coercivity). This effect can be attributed to two factors: one, an increase in the impurity concentration due to sulfur adsorption at the grain boundaries, second, the inclusion of sulfur at the grain boundaries reduces the grain size leading to increase in electron scattering at the grain boundaries [53]. The grain boundaries formed by zipping of the grains/surfaces covered with adsorbed saccharin phase are likely to have more defects; less atom-atom coordination and lower atom packing density contributing to the increase in conduction electron scattering [5, 27, and 29]. Due to increase in sulfur adsorption at the grain boundaries, a non-magnetic phase is formed resulting in increase in the coercive energy and reducing the magnetization as shown in Figure 27b. Figures 28a and 28b show the effect of carbon containing additives on the electrical and magnetic properties of the electrodeposited CoFeNi thin films. An effect similar to sulfur inclusion is observed with increasing carbon content in the deposit. This effect can be attributed to the amorphous like structure formed due to the increasing carbon content and decrease in the grain size of the deposited film [53]. Additives glutamate and EDTA show different trends from citrate and tartrate. From the view point of the molecular structure, the former additives have amino group (-NH) whereas the latter additives have carboxyl group (-COOH). Such functional groups play an important role in adsorption on metal surfaces in complex formation with the metal ions [52, 53]. Compositional analysis clarified that the CoFeNiC film contained traces of nitrogen and oxygen implying that decomposition of amino and

carboxyl groups resulted in such inclusions because no nitrogen and oxygen were observed in the pure CoFeNi film.

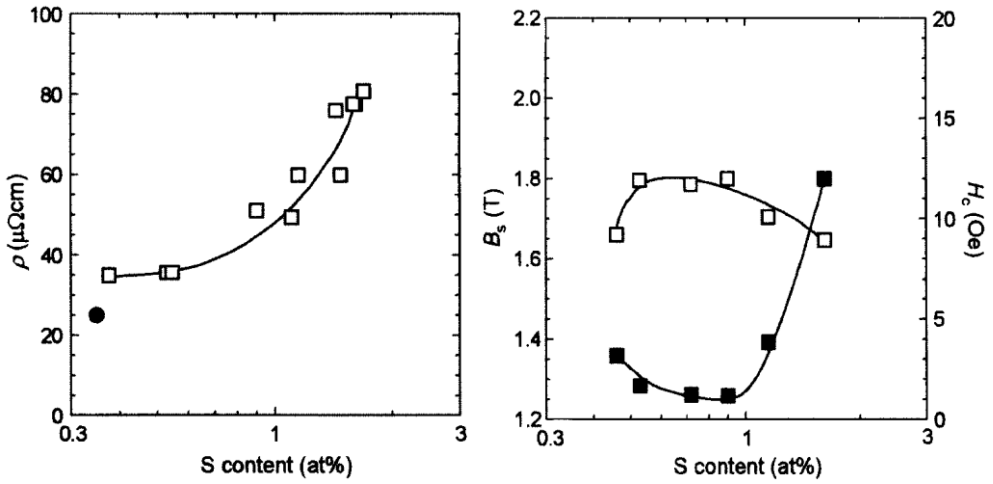

(a) (b)

Figure 27. (a) Resistivity as a function of sulfur content. (b) Coercivity and Magnetic flux density as a function of sulfur content [53].

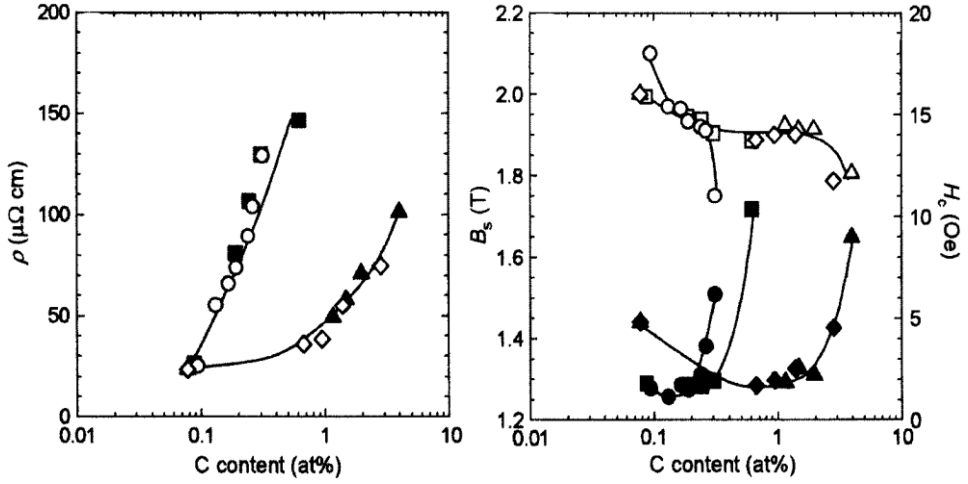

(a) (b)

Figure 28. (a) Resistivity as a function of carbon content. (b) Coercivity and Magnetic flux density as a function of carbon content [53].

4.4.2. Resistivity control in ternary, quaternary alloys

Electrodeposited Permalloy (Ni80Fe20) has been the alloy of choice in the thin film recording heads. However, as the areal density of computer drives has increased significantly (~60% per year), there has been a need to investigate new, high performance magnetic materials [54]. Andricacos and Robertson reviewed the requirements for improved thin film magnetic recording heads which included high magnetic saturation, high permeability, low coercivity, high electrical resistivity and good corrosion resistance [54]. Various binary, ternary and quaternary alloys have been studied to meet the challenges of improved resistivity with superior soft magnetic properties. The alloys studied include CoFeB, CoFeCr, CoFeP, CoNiFeS, CoNiFeCr and CoNiFeB. These alloys were electrodeposited from plating solutions containing saccharin as an additive to relieve the stress during electrodeposition and ascorbic acid to minimize the Fe oxidation.

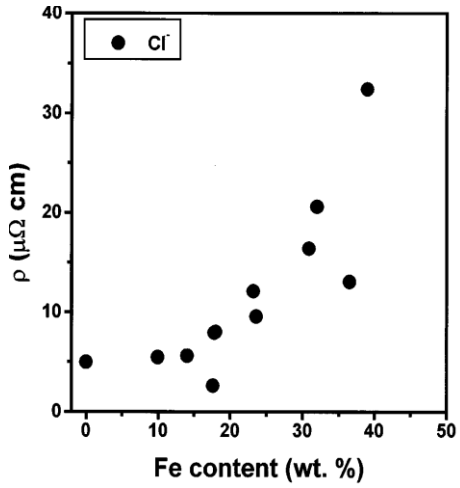

Figure 29. Effect of increasing Fe content on the resistivity of the NiFeX alloy [53, 54].

Solution pH was maintained 3 and all the deposition experiments were conducted at room temperature with no stirring. The electrical resistivity measurements on electrodeposited NiFeCr alloys showed an increase in the resistivity from 5.5 μΩ-cm to 32 μΩ-cm as the Fe content increased in the deposit. The resulting phase structure of the ternary alloy was a fcc-bcc mixed phase structure leading to more defects and interstitials, thereby explaining the increase in resistivity with the ternary alloy. Similarly, CoNiFeB alloys showed higher resistivity as compared to CoNiFe alloys due to the additional impurity incorporation (boron) resulted in higher electron scattering. The resistivity measurements could not be carried out on CoFeB and CoFeP thin films due to huge stresses leading to peeling of the deposits [53].

4.4.3. Effect of annealing on the resistivity of magnetic thin films

Metal crystals are usually never free from imperfections. When a thin film is electrodeposited on a conducting substrate at room temperature, there is significant diffusion through the surface or grain boundary and one would expect the vacancy or void concentration to be much larger than at equilibrium [54, 55]. When the thin film is annealed, these vacancies are subsequently annihilated at the grain boundaries, changing the grain boundary area per unit volume. As the annealing temperature goes higher, other effects such as grain boundary diffusion, vacancy annihilation and grain growth contribute to change the volume of the grain boundary per unit area. Every time a vacancy annihilates, a volume reduction (Ω-Ωv) takes place [54, 55]. If ΔC vacancies are annihilated per unit volume, then the volume average strain in the film is given by,

$$\varepsilon = \Delta C\left(\Omega - \Omega_v\right). \qquad \text{Equation 61}$$

Grain boundary diffusion is a process by which the system redistributes the mass among the grains via grain boundaries [55, 56]. Whereas, grain growth is the mechanism of the grain boundary minimization to form larger grains in order to reduce free energy associated with the grain boundaries. These processes are temperature dependent as grain boundary diffusion is usually dominant at lower temperatures while the grain growth is favored at high temperatures. Diffusion in the crystals is explained by assuming that the vacancies move through the lattice, when atoms hop from vacancy to vacancy [56, 57, and 58]. The vacancies in the film are diffused during grain boundary diffusion. The annihilation of vacancies at the grain boundary minimizes the electron scattering thereby improving the conductivity of the film.

4.5. Resistivity Control in Cu nanostructures

In 1965 Gordon Moore, cofounder of Intel Corp., predicted that the number of transistors in an integrated circuit (IC) would double every year for the next 10 years. This time frame was later changed to doubling every 18 months, but the essence of the prediction sustained and became widely known as the " Moore's law" [59, 60]. One of the parameters contributing to the success of Moore's prediction is the ongoing shrinking in size of transistors and the conducting wires, known as interconnects [60]. The ever-continuing drive to miniaturize the semiconductor devices and interconnects inevitably brought many fabrication processes to be implemented at nanometer scale.

The Cu interconnects for these future devices/microchips are becoming true nanostructures with critical dimensions of the order of few nanometers. The Cu grain size in the interconnect scales with the half of the width of the interconnect lines. Considering that these dimensions are approaching few orders of nanometers, ~10nm, the grain

boundary area per unit volume of interconnects becomes much larger as compared to the Cu thin films. Consequently, the resistivity of the Cu interconnects is higher due to the enhanced electron scattering from the grain boundaries (smaller grain size leads to more number of grain boundaries enhancing the conduction electron scattering at the grain boundaries) [60]. This leads to increase in the power dissipation in the interconnect lines thereby reducing the lifetime of the devices and hampering their performance. One way to improve the conductivity of interconnects is to promote the grain growth via the grain boundary densification process (GBD) [61]. This section mainly discusses the approach to promote grain growth via GBD process when the Cu interconnects are annealed in the mid temperature range (200C, 250 C and 300 C).

4.5.1. Grain Boundary Densification

In a polycrystalline thin film, the density of a region containing a grain boundary is usually different from a region containing no boundary. It is generally accepted that for most materials, the density is reduced by the presence of the grain boundaries. As the grain growth proceeds, two boundaries coalesce to produce a single boundary [57, 61]. If the average value of ‘w’ is assigned to each boundary, the coalescence of two boundaries produces a change ‘2w’. Local atomic forces at the grain boundary try to minimize ‘2w’ to ‘w+a’, where ‘a’ is the atomic diameter. This reduction generates an elastic distortion in the film resulting in a tensile strain in the grains. As the stress produced during coalescence of two boundaries is tensile, it follows that grain growth cannot relax tensile stresses in the thin film. The equation for the total energy change during the grain growth via GBD can be written as [61],

$$\Delta W_{Total} = 4\gamma_{GB} \cdot \left(\frac{1}{d} - \frac{1}{d_0}\right) + \frac{E}{1-\nu} \cdot \left[\Delta a\left(\frac{1}{d} - \frac{1}{d_0}\right) + \varepsilon_0\right]^2 - \frac{E}{1-\nu}\varepsilon_0^2 \ , \qquad \text{Equation 62}$$

where γ_{GB} is the grain boundary energy per unit area, d is the initial grain diameter, d_0 is the final grain diameter, E is the Young's modulus, ν is the Poisson's ratio, Δa is the grain boundary volume per unit area, and ε_0 is the initial strain in the film. This energy needs to be minimized for the grain growth to occur [8, 61]. The energy balance of Equation 62 is maintained by reduction in the grain boundary energy per unit area and an increase in the strain energy due to the increasing strain in the Cu grains. The reduction in the grain boundary area per unit volume (increase grain boundary densification) will improve the conductivity of interconnect. The thermodynamic criteria used to predict whether the grain growth will occur via GBD is derived based on energy minimization principle which can be derived from Equation 62 as [8, 61],

$$d_0 > d_0^{crit} = \frac{E_{Cu}(\Delta a_{Cu})^2}{2\gamma_{GB}(1-\nu_{Cu}) - \varepsilon_0 E_{Cu} \cdot \Delta a_{Cu}} \ , \qquad \text{Equation 63}$$

where d_0 and d_0^{crit} are initial diameter of the Cu grains and critical diameter of the Cu grain above which the grain growth will occur via GBD process. The E_{Cu}, ν_{Cu} are Young's module and Poisson's ratio of Cu, while γ_{GB} and Δa_{Cu} are grain boundary energy and grain boundary volume per unit area for Cu. The above criteria suggests that for a fixed initial strain of Cu grains, ε_0, there is a critical size of the grains, d_0^{crit}, beyond which the grain growth via GBD will occur always until the grain boundary grooving stops the process [8, 61, 62]. In this case there is no practical minimum in total energy change and the total energy will always decrease as the grain grows. For initial compressive strain in the grains ($\varepsilon_0<0$), the d_0^{crit} is very small and the grains will always

grow via GBD process [61]. For initial strain being tensile, ($\varepsilon_0>0$), d_0^{crit} is much larger, and thus, whether the grains will grow or not depends on satisfaction of the $d_0 > d_0^{crit}$ criterion. If $\varepsilon_0 \geq 2\gamma_{GB}(1-\nu_{Cu})/E_{Cu}\Delta a$, (for typical metals > 1%) the grain growth will never occur due to a large strain energy accumulated in the grains independent on their size ($d_0^{crit} \rightarrow \infty$) [8, 61]. Figure 30 shows the relation between the critical grain size and the initial strain in the grains as a function of the interconnect width. The size of the Cu grains scales approximately with the half of the interconnect width. For this reason, in Figure 30, the three different interconnect widths are indicated and their intersects with the lines representing the model calculation show the limiting strain below which the GBD will occur, and above which it will not for a given grain size. In this analysis, the initial grain size is considered fixed and function of the Cu-interconnect design.

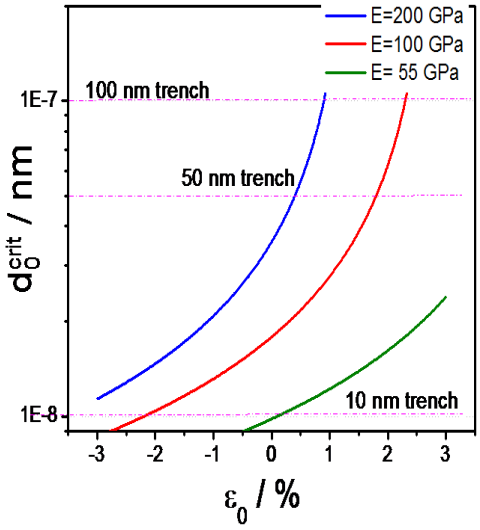

Figure 30: Calculations are done for three typical values of Young's modulus used for electrodeposited Cu. Each curve represents the boundary between the regions where the grain growth via GBD process is possible (above the curve) and where it is not (below the curve) [62].

The initial strain in the Cu grains, ε_0, during annealing is a function of several separate contributions which can be expressed as [8, 63]

$$\varepsilon_0 = \varepsilon_i + \varepsilon_{th} \quad , \qquad \text{Equation 64}$$

where the growth strain ε_i and the thermal strain ε_{th} are the dominant ones. The growth strain in the Cu grains largely depends on the growth mechanism (like superfill, dual damascene) and can be evaluated using existing models in the literature based for grain zipping process [8, 63]. Using the grain size to be equal to the ½ of the width of Cu-interconnect, typical values of growth strain measured in Cu grains are $\varepsilon_i \approx 0.1 \pm 1.4$ %. The ε_{th} in Cu interconnect is more difficult to be evaluated due to complexity of the materials in the microchip hetero-structure. However, the basic estimate can be made using the Cu and Si as two materials with dissimilar coefficients of thermal expansion. This analysis predicts the ε_{th} to be in the range of -0.14 ± -0.7 %. Using these calculations the initial strain in Cu interconnects during annealing can be evaluated as $\varepsilon_0 \approx$ -0.5 % to 1.3%. However, this level of initial strain will not been sufficient to promote the grain growth via GBD for interconnect with critical dimensions below 50nm [8, 61].

For this reason, the approach of strained annealing is used to externally control the initial strain in the grains by applying a controlled curvature on the cantilever with the fabricated Cu interconnects as shown in Figure 31a. During annealing, cantilevers are under biaxial state of stress, and the externally imposed strain ε_{rr} and $\varepsilon_{\theta\theta}$ ($\varepsilon_{\theta\theta}=-\varepsilon_{rr}$) can be algebraically summed with initial strain existing in Cu grains ε_0. Due to geometry of the cantilever bending and position of the Cu interconnects, the $\varepsilon_{rr}>0$ and $\varepsilon_{\theta\theta}<0$ situation always applies. This means that resulting strain in Cu grains during annealing,

$\Delta\varepsilon_{rr} = \varepsilon_{rr} + \varepsilon_0$, was such that $\Delta\varepsilon_{rr} > \varepsilon_0$ and $\Delta\varepsilon_{\theta\theta} < \varepsilon_0$ are always achieved [8, 34, 61]. The schematics of the strain sign and orientation in Cu-interconnects are illustrated in Figure 31b.

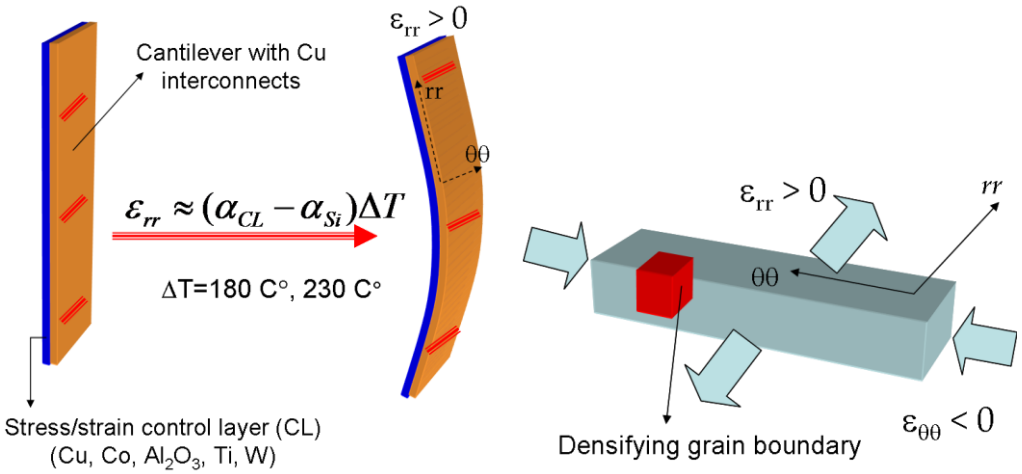

(a) (b)

Figure 31. (a) Strained annealing of the Cu interconnect by growing a strained layer (control layer) on the back of the cantilever (b) Grain boundary densification along θθ direction [8].

As one sees, the strain in θθ direction is effectively reduced by bending of the cantilever which is expected to promote densification of the grain boundaries with surface vector parallel to θθ direction, thus improving the conductivity of the interconnect.

CHAPTER 5

EXPERIMENTAL METHODS

The literature discussed in the previous chapters proved significant in designing the experimental methods and procedures to carry out the experiments for the detailed analysis of electroplated magnetic films and copper nanostructures. The physical properties of the electrodeposited CoFeNi alloys have been studied using several characterization techniques. The first part of the Chapter 5 discusses the various experimental setups designed for the characterization of the electrodeposited films. The procedure for the stepwise implementation of the setups is explained with detailed information of the setup components. The later part of the Chapter 5 focuses on various experimental methods and techniques used for the characterization and fabrication of the CoFeNi magnetic alloys and the Cu nanostructures. The basic principles underlying the working and construction of these instruments are described briefly to provide the reader a general overview of the experimental methods used.

5.1. EXPERIMENTAL SETUPS

5.1.1. Vibrating Sample Magnetometer (VSM)

A Vibrating Sample Magnetometer (VSM) measures the magnetic moment of a sample when it is vibrated perpendicular to a uniform magnetizing field [3]. The VSM is a simple, inexpensive and versatile research tool that provides precise magnetic moment measurements. In addition to convenient measurements using a laboratory electromagnet, this instrument minimizes the sources of errors in the other methods. This instrument is

used to detect changes as small as 10^{-4} to 10^{-6} emu with stability of one part in 10^{4} emu. The working principle and mechanical design of the VSM is explained in this section.

5.1.1.1. Principle

The Vibrating Sample Magnetometer operates on the principle of Faraday's law of electromagnetic induction. According to Faraday, when a coil of wire is placed in an alternating magnetic field, an emf is induced in the coil. In the VSM, the sample is vibrated in a direction perpendicular to the magnetic field. The oscillating magnetic field of the vibrating sample induces an emf in the stationary detecting coils [3, 64]. This emf is compared with the measured emf of a reference sample. Ideally the VSM should be calibrated with a known standard that has the same shape and size of the sample to be measured. Typically a 99.999% pure Ni spherical ball, fabricated by NIST, is used as a standard. The mass of the sample and the emf induced in the coils is measured. This helps to calculate the magnetic moment of the sample and the calibration constant of the instrument used for measurement. This calibration constant is then used to accurately determine the magnetic moment of the unknown sample.

5.1.1.2. Mechanical Design

Moment measurements were done performed on a Lakeshore 7400 series VSM, to determine the coercivity of the electrodeposited magnetic alloys. Figure 33 shows the schematic of a typical VSM. The sample, commonly spherical in shape, is attached to the end of a nonmagnetic rod. The other end of the rod is fixed to a mechanical vibrator, typically a loudspeaker cone as shown in Figure 32. The oscillating magnetic field of the moving sample induces an alternating emf in the detection coils (pick up coils), whose magnitude is proportional to the magnetic moment of the sample. The alternating emf is

amplified using a lock-in amplifier which is sensitive only to the signals at a particular frequency (i.e. vibration frequency). The detection coil arrangement shown in Figure 32 is one of the several possible ones described by Foner [64]. The vibrating frequency is around 100 Hz and the amplitude is of the order of few millimeters.

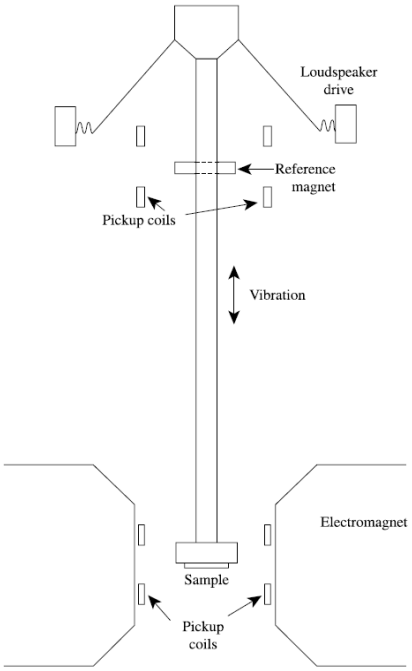

Figure 32. Schematic of a Vibrating Sample Magnetometer [3, 64]

The amplitude of the sample varies depending on the mass of the sample. The apparatus in Figure 32 is calibrated with a specimen of known magnetic moment, which must be of the same size and shape as the sample to be the measured.

5.1.1.3. Operation

The measurements are position sensitive; to the exact sample position between the pair of coils. To begin with, a step by step procedure, known as saddling, is used to ensure that the sample is accurately placed in the center of the magnetic field [64, 65].

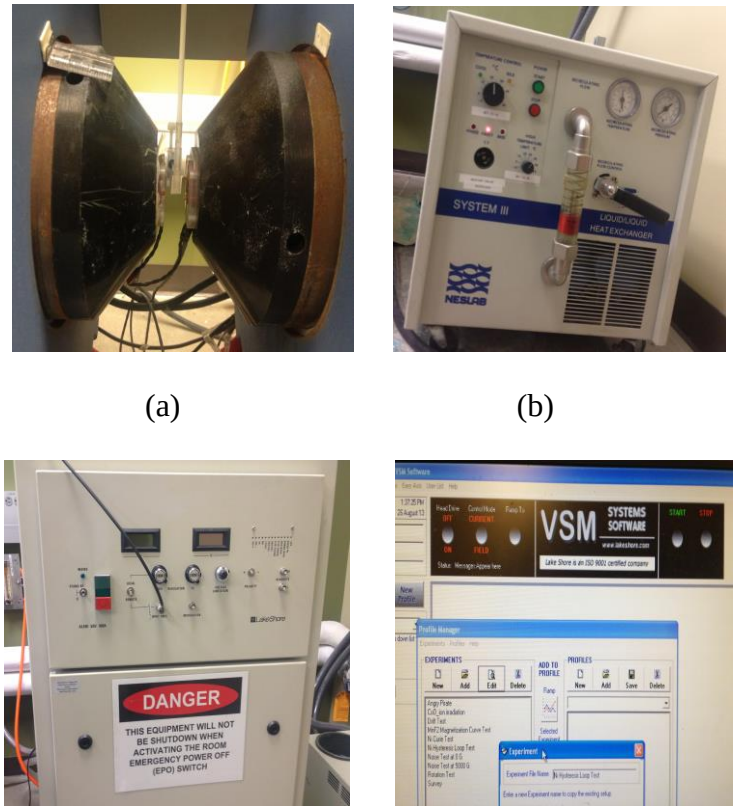

(a) (b)

(c) (d)

Figure 33. (a) Saddle point located on a Lakeshore 7400 series VSM (b) Chilled water source (heat exchanger) (c) Power Supply to drive the electromagnets (d) GUI software provided by Lakeshore for moment measurements.

The sample is first centrally positioned by visual inspection. The sample coils are then rotated about the z-axis for maximum signal output. The coils are then translated along X-axis for a minimum output, and along the Y-axis (perpendicular to the paper) for maximum output. The sample is now located at a "saddle" point wherein the output signal is independent of small displacements of the sample in any direction. Figure 33a shows the saddle point located on a Lakeshore 7400 series VSM. The sample is placed on rod which vibrates at the given frequency. Figures 33b and 33c show the chilled water setup and power supply to drive the magnets respectively. In Figure 33d, a typical

experiment for moment measurement has been shown with the experimental parameters in a GUI provided by Lakeshore. The X, Y and Z screws are used to move the sample along the respective axes. The location of the saddle point is confirmed by obtaining a graph of variation in magnetic field as a function of distance between the coils in X, Y and Z axes. Figure 34 shows the typical graphs obtained for X, Y and Z axes.

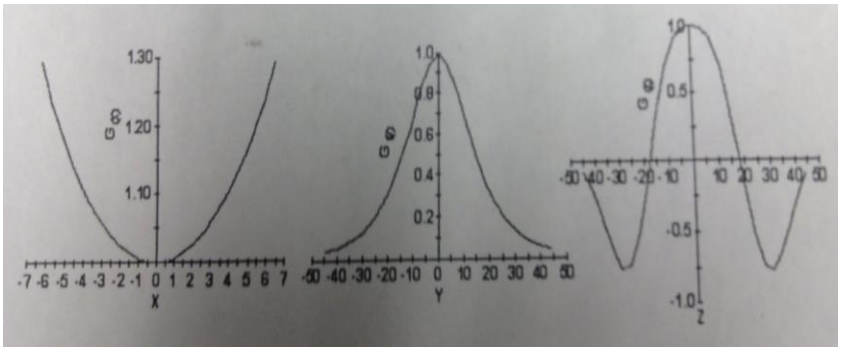

Figure 34. Typical graphs when the sample location is saddled along X, Y and Z axes to obtain the saddling point.

After obtaining the saddle point, the moment measurements were performed by selecting a sweep field (range of -50,000 G to +50,000G). With the help of the Lakeshore User Interface Software, the parameters for the moment measurement are selected and then the field is applied by turning on the power supply driving the magnets. A typical MH loop for one such CoFeNi film electrodeposited from bath containing 2g/L saccharin is shown in Figure 35. The moment is measured at several steps when the field is swept from a particular positive range to a negative range. The field value at which the magnetic moment becomes zero is known as the coercivity or coercive field. The magnetic moment saturates beyond a particular sweeping field and is known as the saturation magnetic moment or saturation magnetization.

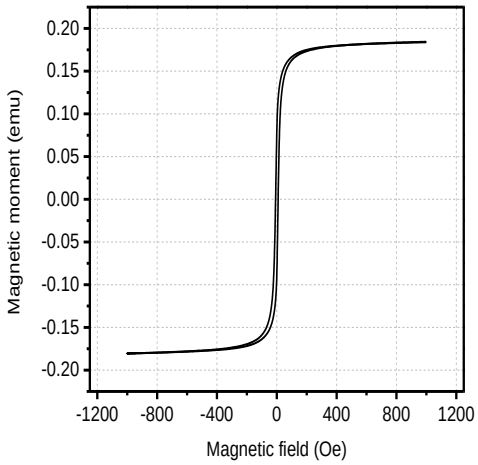

Figure 35. M-H loop for CoFeNi film electrodeposited from solution containing 2g/L saccharin.

5.1.2. Four Point Probe Resistivity Measurements

The presented research involving the development of new magnetic materials for reducing the energy transfer losses intends to design a magnetic material with high resistivity, high saturation magnetic moment, high permeability, low coercivity and other physical and metallurgical properties. As explained in section 5.1.1, Vibrating Sample Magnetometer is used to measure the magnetic properties of the electrodeposited CoFeNi alloy. The equipment used for measuring the resistivity of the electrodeposited CoFeNi thin films is a four-point probe setup. This section discusses the principle and method of resistivity measurement of the thin film electrodeposited magnetic alloys.

5.1.2.1. Principle

The conductivity (σ) of a material is defined to be the current density (J) divided by the applied electric field (E) given as,

$$\sigma = \frac{J}{E} \ . \qquad \text{Equation 65}$$

Since the current density equals the product of the charge of the mobile carriers, their density and velocity it can be expressed as a function of the electric field using the mobility. To include the contribution of the electrons as well as holes to the conductivity of the material, the current density due to the holes and electrons is added together [1, 2]. The total current density can be expressed as,

$$J = q \cdot n \cdot v_e + q \cdot p \cdot v_h \ , \qquad \text{Equation 66}$$

where q is the charge on the carrier, n is the number of electrons, p is the number of holes, v_e is the drift velocity of the electrons and v_h is the drift velocity of the holes. Now, drift velocity (v_d) can be written in terms of the mobility of the charge carriers (μ) and the electric field (E) as,

$$v_d = \mu \cdot E \ . \qquad \text{Equation 67}$$

Substituting Equation 67 in Equation 66, the total current density can be expressed as [1, 2],

$$J = q \cdot (n \cdot \mu_n + p \cdot \mu_h) \cdot E \, . \qquad \text{Equation 68}$$

Substituting Equation 68 in Equation 65, the conductivity of the material in terms of the mobility of the charge carriers and the applied electric field can be written as,

$$\sigma = \frac{J}{E} = q \cdot (n \cdot \mu_n + p \cdot \mu_h) \ . \qquad \text{Equation 69}$$

The resistivity (ρ) is defined as the inverse of the conductivity [2, 66], namely:

$$\rho = \frac{1}{\sigma} = \frac{1}{q \cdot (n \cdot \mu_n + p \cdot \mu_h)} \, . \qquad \text{Equation 70}$$

The sheet resistance (R_{sh}) of the material can be calculated from the resistivity calculated in Equation 70. By measuring the material length (l), width (w) and area of cross section (A), the sheet resistance can be calculated as,

$$R_{sh} = \rho \cdot \frac{l}{A} = \rho \cdot \frac{l}{w \cdot t_f}\,. \qquad \text{Equation 71}$$

The sheet resistance of the material is measured with the four point probe setup. Knowing the physical properties of the material (length, width and thickness), the resistivity of the material can be calculated.

5.1.2.2. Method of measurement

The schematic of a four point probe measurement setup is shown in Figure 36. The outer two probes force a current (*I*) through the material while the inner two probes measure a voltage (*V*) across the sample. The distance between the two probes is 'S' and should be ideally less than the thickness of the material whose resistance is to be measured. The resistance measurements can be done by using just two probes as well; however, the contact resistance and the current spreading problems associated with the probes leads to a large measurement error. Figure 37 shows the equivalent circuit diagram for a two point probe measurement system. R_x is the unknown resistance of the material, $R_{x\,(measured)}$ is the measured resistance of the material and R_c is the contact resistance of the two probes. Let *V* be the measured voltage across the material when a current *I* is forced into the material. Using Ohm's law, the resistance $R_{x\,(measured)}$ can be calculated as,

$$R_{x(measured)} = \frac{V}{I}\,. \qquad \text{Equation 72}$$

The current forced through the material can be calculated as,

$$I = \frac{V}{(R_x + R_c + R_c)}\,. \qquad \text{Equation 73}$$

Substituting Equation 73 into Equation 72 and solving for unknown resistance $R_{x(measured)}$,

$$R_{x(measured)} = \frac{V(R_x + 2R_c)}{V} = R_x + 2R_c . \qquad \text{Equation 74}$$

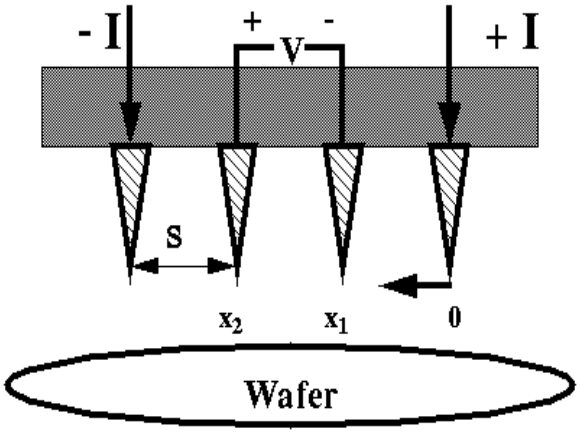

Figure 36. Four point probe measurement schematic [66]

From Equation 74, we can conclude that the material resistance measured with the two point probe setup will be off by a huge margin if the contact resistance is high.

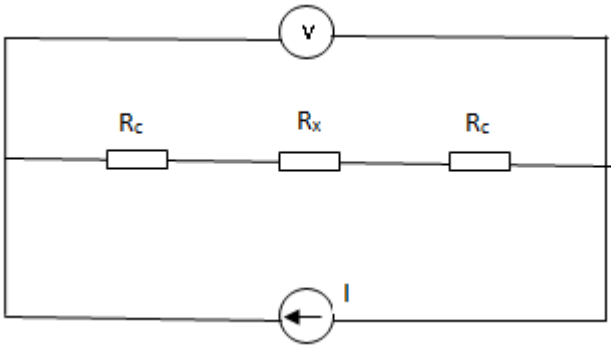

Figure 37. Equivalent circuit for a two point probe measurement system

Typically, the contact resistance is small and can be neglected; however, if the material resistance is not large, then the contact resistance cannot be ignored. The error due to the

contact resistance influencing the two point probe resistance measurement method can be eliminated by using a four point probe measurement. Figure 38 shows the equivalent circuit diagram for a four point probe measurement system. Let the resistance of the voltmeter be indicated as R_m and is ideally considered to be infinite as voltmeter draws zero current. In the circuit shown in Figure 38, the resistance measured can be expressed in terms of the Ohm's law as,

$$R_{x(measured)} = \frac{V_{R_x}}{I} = \frac{I_x \cdot R_x}{I}. \qquad \text{Equation 75}$$

Using the current divider rule, I_x can be calculated as,

$$I_x = \frac{I \cdot (2R_c + R_m)}{(2R_c + R_m + R_x)}. \qquad \text{Equation 76}$$

Substituting Equation 76 into Equation 75,

$$R_{x(measured)} = \frac{I \cdot (2R_c + R_m) \cdot R_x}{(2R_c + R_m + R_x) \cdot I}. \qquad \text{Equation 77}$$

Since R_m is an infinitely large resistance with respect to the resistors in the circuit (voltmeter has very large resistance), the ratio $\frac{(2R_c + R_m)}{(2R_c + R_m + R_x)} \sim 1$ ($R_m >> R_c$); thus the source of error due to contact resistance is minimal which implies $R_{x(measured)} \sim R_x$. The four point probe measurement technique completely eliminates the error in the measurement due to contact resistance; hence, is used predominantly in the industry for resistance measurement. Now, calculating the expression for resistance measurement using four point probe method in terms of the applied voltage and the current measured. Consider a thin material of the order of few nanometers on which the measurements are done as shown in Figure 36. Let the distance over which the current flows in the material

be x, the thickness of the material be ‘t’, the spacing between the probes be s.

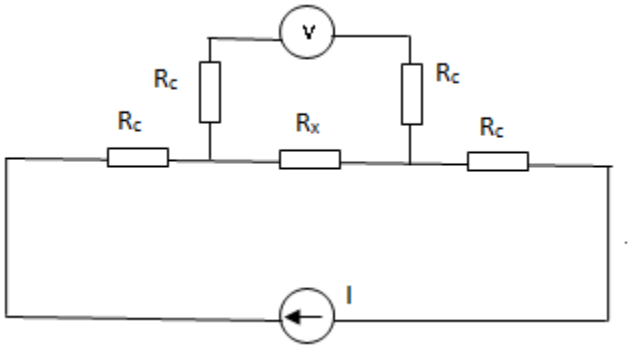

Figure 38. Equivalent circuit for a four point probe measurement system

From the given parameters, the cross section area of the material can be calculated as $A \sim 2\pi \cdot x \cdot t$. Integrating the equation for the sheet resistance over the total area of the material [2, 66],

$$R_{sh} = \int_{s}^{2s} \frac{\rho \cdot dx}{2\pi \cdot x \cdot t} \quad . \qquad \text{Equation 78}$$

Substituting the limits of integration the sheet resistance over the total area of the material can be calculated as,

$$R_{sh} = \frac{\rho \cdot \ln 2}{2\pi \cdot t} \quad . \qquad \text{Equation 79}$$

Similarly, by applying superposition at the probes,

$$R_{sh} = \frac{V}{2I} \quad . \qquad \text{Equation 80}$$

Combining Equations 79 and 80, we can derive the equation for the resistivity of the material measured using the four point probe measurement setup as,

$$\rho = \frac{\pi \cdot t \cdot V}{\ln 2 \cdot I} \quad . \qquad \text{Equation 81}$$

Sheet resistance per unit length of a material can be derived from the resistivity by the formula,

$$R_{sh} = \frac{\rho}{t} \quad . \qquad \text{Equation 82}$$

Substituting Equation 81 into Equation 82, we obtain the final expression for sheet resistance measured using the four point probe which is given as [2, 66],

$$R_{sh} = 4.532 \cdot \frac{V}{I} \quad . \qquad \text{Equation 83}$$

5.2. IN-SITU STRESS MEASUREMENT SYSTEM

An in-situ stress measurement setup was designed to measure the stress evolving during electrodeposition and annealing of magnetic materials, namely NiFe, CoFe and CoFeNi soft high moment magnetic alloys [67]. This section will begin with an outline of the stepwise preparation of the samples for stress measurements followed by an explanation of the design of the in-situ stress measurement system.

5.2.1. Steps for Sample Preparation

There are capacitive and curvature methods to measure the in-situ stress developed in thin films. Stoney, in 1909 proved that the intrinsic stress in thin films can be measured by change in the curve of the substrate [68, 69]. Stoney's equation was used to calculate the in-situ stress from the measurements of the laser light reflected back from bending of a cantilever. Glass cantilevers 50mm long, 4mm wide and 0.21 mm thick, manufactured by Precision Glassware, are used as substrates to measure the stress

evolved in electrodeposited thin films. Initially, these cantilevers are cleaned in boiling piranha solution (90 C) for 1 hour to remove any traces of organic contaminants. These cantilevers are then sonicated for 15min in ethyl alcohol, rinsed thoroughly with DI water (18.5 MΩ) and dried in nitrogen ambient to obtain an ultra-clean surface [55, 67]. Cleaned glass cantilevers are then coated with conductive materials to provide a contact for electrodeposition. Typically, 5nm of Titanium (Ti) and 100 nm of Gold (Au) are deposited on the cantilevers using thermal evaporation. Titanium (or tantalum at times) is used as an adhesive layer for the Gold to stick on the glass substrate and prevent the peeling of the Gold layer during electrodeposition [55, 67].

5.2.2. Stress measurement during electrodeposition

The system is based on a similar system built by Gerry Stafford at NIST [68]. The curvature of the film is measured using an optical system assembled on a vibration isolation table as shown in Figure 39. The light source used in the optical system is a 10mW, JDSU 632.8nm, He-Ne (red) laser. The laser delivers a polarized beam of light onto a 1" circular reflecting mirror at an angle of 45^{o} to the incident beam. The reflected beam falls on the collimator, an iris with a narrow opening to allow maximum intensity of the laser to pass through. A beam splitter is used to split the maximum intensity laser beam into two parts. One part of the beam falls on the electrodeposition/ annealing cell whereas the other part of the beam is not used. The beam falling on the cell is reflected from the backside of the cantilever, which again passes through the beam splitter. One part of it falls on the photo-sensitive detector (PSD) while the other part is blocked by the collimator.

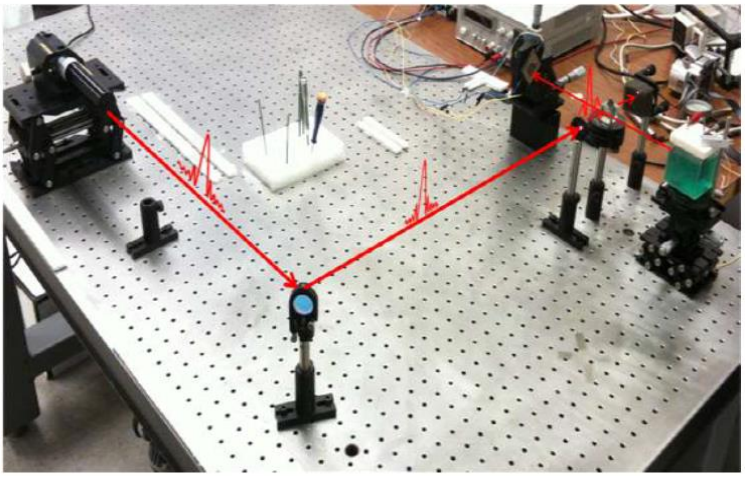

Figure 39. Optical in-situ stress measurement setup [67, 68]

A duo-lateral PSD from OSI Optoelectronics with an active area of 20mm by 20mm is used. As the film is deposited, the cantilever bends due to stress built up in the electrodeposited film; thus causing the laser spot reflected from the cantilever to move along the vertical axis [67].

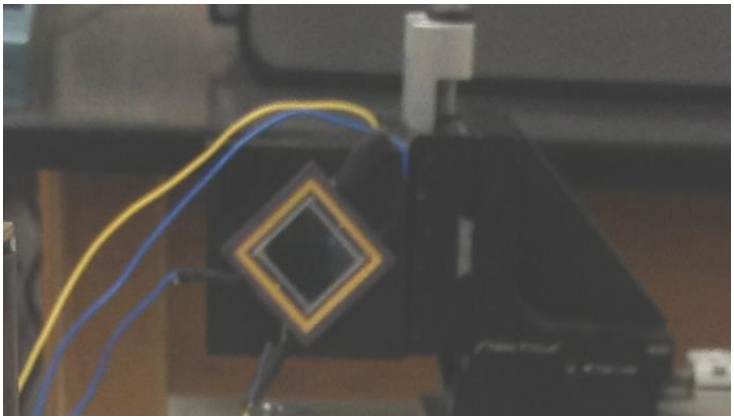

Figure 40. PSD kept in the diagonal position (maximum vertical length).

The PSD is kept in the diagonal position to use the maximum vertical length (diagonal =28.28mm) as shown in Figure 40. The PSD works on the principle of a photo diode.

When a light shines on the PSD, it generates current in its four electrodes proportional to the position and intensity of the laser spot on the PSD. The current output of the PSD is of the order of few μA. Calculating the displacements from input of such small currents leads to a very noisy displacement data; thus, a transresistance amplifier circuit is used to convert the current to a voltage (amplified), in the range from 0 to 5V [67, 68]. The schematic of the amplifier circuit is shown in Figure 41 (a) and the actual circuit implemented as shown in Figure 41 (b).

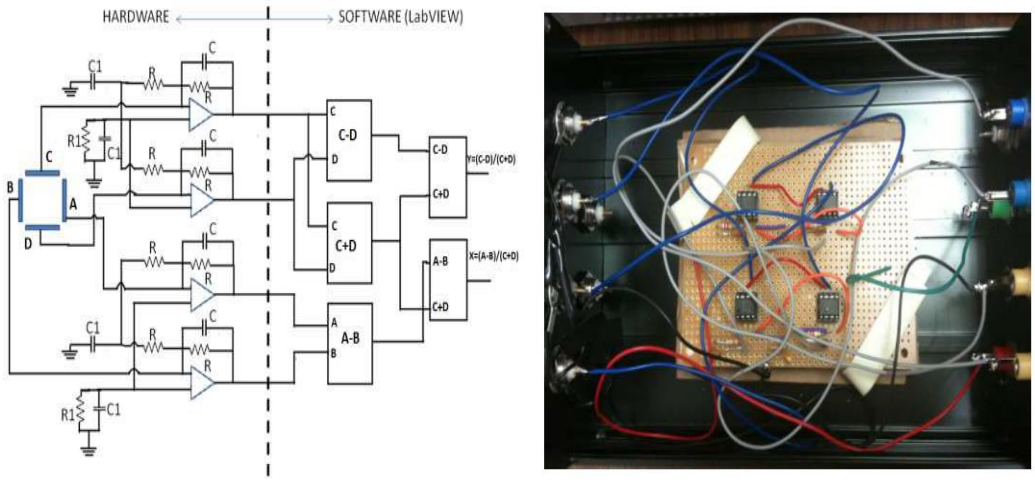

(a) (b)

Figure 41. (a) Schematic of the transresistance amplifier (b) Circuit implemented with IC 741 op-amp on a breadboard [55, 67].

The circuit is made up of four operational amplifiers, popularly known as op-amps. The gain of the amplifier is adjusted such that the output of the PSD is compatible with the data acquisition (DAQ) system. The DAQ system consists of the National Instruments board (NI PCI 6143 S-Series) and LABVIEW as the interface software for data collection. The particular board was selected based on number of channels required,

sampling rate, and precision and input voltage rage. The position of the laser on the PSD is calculated as [55, 67],

$$X = \frac{A-B}{A+B} \times \frac{L}{2} \qquad \text{Equation 84}$$

and

$$Y = \frac{A-B}{A+B} \times \frac{L}{2} \ . \qquad \text{Equation 85}$$

where A, B are the anode voltages and C, D voltages are the cathode voltages respectively, length of the side of the PSD (20mm in our case). From this, we calculate the displacement of the laser on the PSD as [55, 67, and 68],

$$d_{PSD} = \sqrt{(X - X_o)^2 + (Y - Y_o)^2} \ . \qquad \text{Equation 86}$$

This corresponds to the curvature of the film. Here, (X_o, Y_o) indicate the co-ordinates of the initial position of the laser on the PSD. Then using Stoney's equation, the force per unit width acting on the film was calculated as [55, 67, and 69],

$$F/w = \left(\frac{E}{1-\nu}\right)_s \frac{t_s^2 * \eta_{air} * d_{PSD}}{6 * 2 * L * \eta_{solution} * D_{PSD}} \ , \qquad \text{Equation 87}$$

where E_s is the Young's modulus of the glass cantilever (72.96 GPa), t_s is the thickness of the cantilever (0.21mm), ν_s is the Poisson's ratio of the cantilever (0.028), η_{air} is the refractive index of air (1) and $\eta_{solution}$ is the refractive index of the plating solution (1.33) since the solution is aqueous. The thickness of the electrodeposited film can be calculated by the following expression [55, 67],

$$Thickness = \int_0^t \frac{I * \gamma * t * \nu_m}{A * n * F} dt \ , \qquad \text{Equation 88}$$

where I is the deposition current, γ is the current efficiency (calculated using cyclic voltammetry), t is the time of deposition, ν_m is the molar volume of the film ($6.667*10^{-6}$

moles/m^3), A is the surface area of the substrate, n is the number of electrons exchanged (2) and F is the Faraday's constant (96500 C/mol). From Equation 87 and 88, the average stress (σ) can be calculated as,

$$Stress(\sigma) = \frac{F/w}{Thickness}[Pa]. \qquad \text{Equation 89}$$

The sensitivity of the stress measurement system can be defined as the smallest change in the measurement, which the system can resolve. Using Stoney's equation, the stress in the film can be expressed as [67, 68, and 69],

$$Stress(\sigma) = \left(\frac{E}{1-v}\right)_s \frac{t_s^2}{6r \cdot t_f} \ . \qquad \text{Equation 90}$$

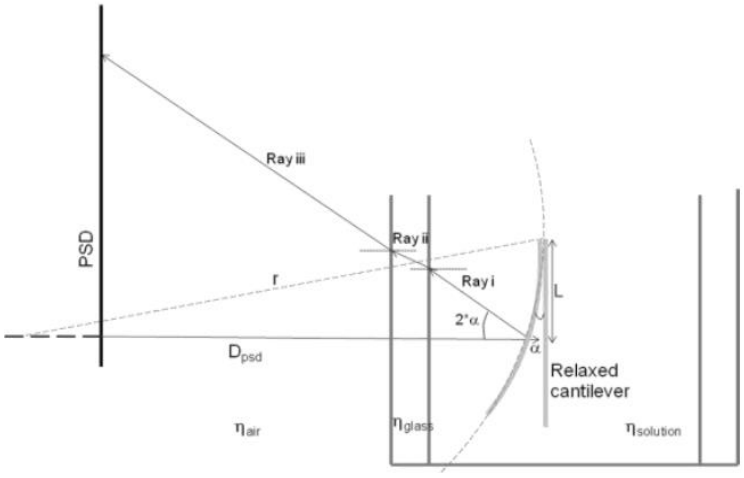

Figure 42. Schematic of the reflected laser beam from the cantilever and the geometry used for the conversion of the radius of the curvature to measureable entities (stress, force per unit width) [67, 68].

The product of the stress and the thickness gives the force exerted per unit width of the cantilever which can be derived as,

$$F/w = \sigma_f * t_f = \left(\frac{E}{1-v}\right)_s \frac{t_s^2}{6r} \quad , \qquad \text{Equation 91}$$

where r is the radius of the curvature, formed by the cantilever due to the internal stress in the film. The schematic is shown in Figure 42. If we assume that the angle formed between the stressed state and the relaxed state of the cantilever is α, then the angle between the incident ray and the reflected ray from the cantilever (indicated by Ray i) is 2α. Let η_{air}, η_{glass} and $\eta_{solution}$ be the refractive indices of air, glass and solution respectively. Let us assume the length of the cantilever to be L and the distance between the PSD and the cantilever to be D_{PSD}. Now since α is very small, then we can assume $\sin\alpha = \alpha$. Thus, the radius of curvature can be written as [8, 9],

$$r = \frac{L}{\alpha} \quad . \qquad \text{Equation 92}$$

Now, by using Snell's law of refraction, for Ray i and Ray ii,

$$\frac{2\alpha}{\theta_i} = \frac{\eta_{glass}}{\eta_{substrate}} \quad , \qquad \text{Equation 93}$$

where θ_i (not shown in the figure) is the angle between the Ray ii and normal. Similarly, Snell's law of refraction, for Ray ii and Ray iii can be written as,

$$\frac{\theta}{\theta_i} = \frac{\eta_{glass}}{\eta_{air}} \quad . \qquad \text{Equation 94}$$

Combining Equation 93 and 94,

$$\alpha = \frac{\eta_{air} * \theta}{2 * \eta_{solution}} \quad . \qquad \text{Equation 95}$$

Substituting value of α into Equation 92,

$$r = \frac{2 * L * \eta_{solution}}{\eta_{air} * \theta} \quad , \qquad \text{Equation 96}$$

where θ is the ratio of the displacement of the laser spot on the PSD (d_{PSD}) to the distance between the cantilever and the PSD (D_{PSD}). Thus, the final equation for radius of curvature can be obtained as,

$$r = \frac{2 * L * D_{PSD} * \eta_{solution}}{\eta_{air} * d_{PSD}} \ . \qquad \text{Equation 97}$$

Substituting Equation 97 into Equation 91 to obtain the final expression for force per unit width as,

$$\sigma_f = (\frac{E}{1-v})_s \frac{t_s^2 * \eta_{air} * d_{PSD}}{12 * L * D_{PSD} * \eta_{solution} * t_f} . \qquad \text{Equation 98}$$

The typical values of the parameters in Equation 98 are, L = 34mm, D_{PSD} = 300mm, η_{air} =1 and $\eta_{solution}$ = 1.33 (for water). The resolution of the PSD is 1μm (d_{PSD}). For the substrate, the Young's modulus (E) = 72.9 GPa, Poisson's ratio (v) = 0.208 and the thickness of the substrate (t_s) = 0.21mm. Thus, theoretically, the maximum radius of curvature which can be measured is 31.92 km and the smallest value of F/w = 0.0211 N/m; but practically the resolution of the setup for F/w ~ 0.5N/m [55, 67, 68, 69].

5.2.3. Stress measurement during annealing

The stress measurement during annealing is also based on the laser curvature method explained in section 5.2.2. The curvature of the film is measured as a function of the annealing temperature and the corresponding stress evolution in the film is calculated. The annealing system consists of a heat source, a temperature sensor, a quartz enclosure and a controller (PID controller). The films to be annealed are usually deposited on glass cantilevers using electrodeposition as explained in the previous section. These thin films are annealed in inert atmosphere at temperatures 200 C, 250 C and 300C. The curvature of the film is measured using an optical system assembled on a vibration isolation table

as shown in Figure 43. In the following sub-sections, each component of the annealing system is explained in detail along with the specific selection criteria.

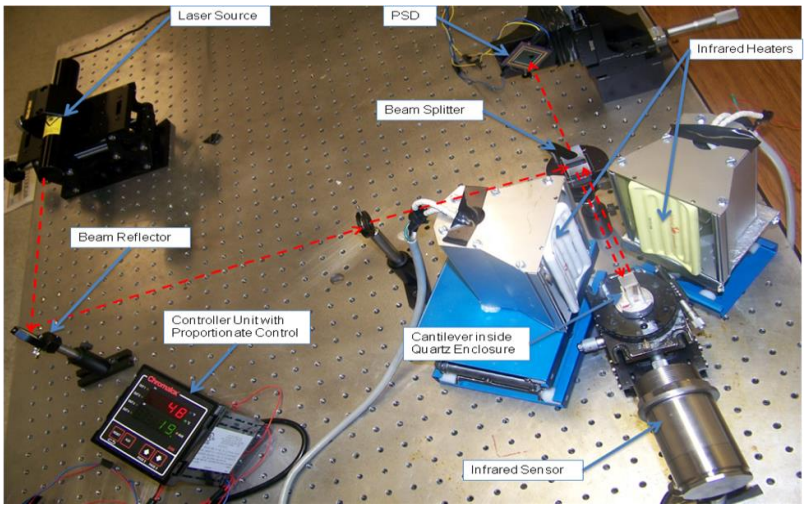

Figure 43. In-situ stress measurement system during annealing comprising of the heat source, temperature sensor, quartz enclosure, PID controller and an optical system to calculate the curvature as function of the annealing temperature [55].

i. Heat Source

Infrared heaters were selected as a heat source in the annealing system. Infrared energy provides the most efficient heat transfer without contact between the heat source and the work piece. It's a radiant energy which passes through space in the form of electromagnetic waves. Electromagnetic waves are result of a disturbance in electric and magnetic field of charged particles due to atomic motion. Whenever an object is heated, it radiates electromagnetic waves. When that electromagnetic wave reaches another object maintained at room temperature (relatively cool), the changing electric and magnetic fields of the electromagnetic wave will act on the charged particle in the atoms of the cool object [55, 70]. Thus, the energy transfer from a hot object to a cool object occurs

without physical contact and a medium for transfer. Infrared radiation is part of a broad electromagnetic spectrum as shown in Figure 44 [71]. The electromagnetic spectrum shows the variety of wavelengths and frequencies of the electromagnetic waves.

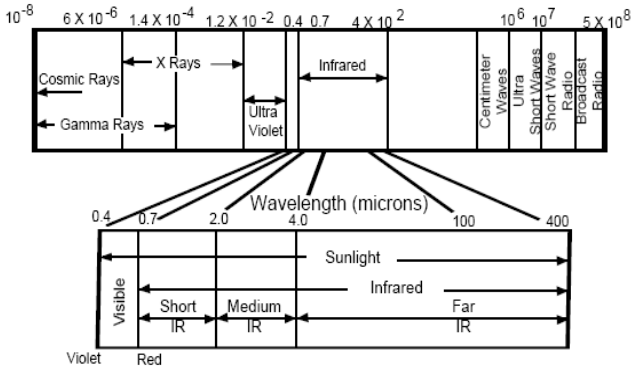

Figure 44. The electromagnetic spectrum [71]

When any form of electromagnetic radiation strikes an object (shown in Figure 45), the radiant energy is either absorbed, transmitted or reflected from the object surface. The energy absorbed by the object contributes to heat the object.

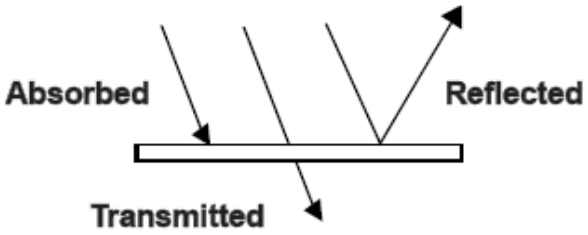

Figure 45. Law of Conservation of Energy

If an object absorbs (emits) 100% of the incident radiant energy, it is called a 'black body'. Emissivity of an object is defined as the ratio of the radiant energy emitted by the

object at a given temperature to the radiant energy emitted by a 'black body' at the same temperature [71, 72]. Emissivity can be expressed mathematically as [71, 72],

$$\varepsilon = \frac{W_o}{W_{BB}}, \qquad \text{Equation 99}$$

where ε is the emissivity of the object, W_o is the radiant energy emitted by the object at temperature T and W_{BB} is the radiant energy emitted by a 'black body' at the temperature T. From Equation 99, the emissivity of a 'black body is calculated to be 1. All real surfaces have emissivities less than one. In general non-metallic surfaces have good emissivities (close to 1) and shiny metallic surfaces have low emissivities (close to 0) as they are good reflectors. Electrodeposited thin films have low emissivities because they transmit a large part of the incident energy striking the surface. The emissivity of these thin films depends largely on the film thickness, the annealing temperature and the wavelength of the incident energy [72].

While selecting an infrared heat source, factors to be considered are the object to be heated, physical dimensions of the object, surface coating, infrared absorption characteristics, the power level requirements, starting work temperature, final work temperature and the time-temperature relationship. The main advantage of radiant heating technique over alternative heating methods of conduction and convection are the ability to produce heat in the object without physically contacting it [72, 73, and 74]. This can be helpful when the object needs to be heated while or motion or when a physical contact would contaminate or damage the object's surface. Also, infrared heaters are fast and highly efficient. The energy radiated is concentrated and focused which greatly reduces the energy losses. Additionally, the infrared heaters provide controlled temperature

accuracy and lower cost of energy [74]. Figure 46 shows the infrared heaters implemented in the annealing system. It consists of Ceramic Heating Element operating at 120 V, 500W power [74, 75].

Figure 46. Infrared Heaters (Salamander Ceramic Infrared Heating Element)

ii. Temperature Sensor

The previous section discussed about the electromagnetic spectrum and basic theories of infrared energy transfer. In this section, the principle and working of the infrared temperature sensor will be discussed. As explained before, any object with temperature above absolute zero will emit an electromagnetic radiation from its surface, which is proportional to its temperature [55, 75, and 76]. With the help of an optical system, this radiation is focused on a detector which generates an electrical signal proportional to the radiation. The signal is amplified and processed into an output signal proportional to the object temperature. An infrared sensor is made up of collecting optics, lenses, fiber optics, special filtering and a detector element. Depending on the material

chosen for the lenses, these optics can only allow a certain range of infrared wavelengths only [75, 76]. This property can be used to detect different target materials corresponding to a specific wavelength. The most important part of the infrared sensor is the detector element, which receives the radiation. These are thermal detectors made of temperature sensitive elements which absorb energy as a form of the electromagnetic radiation [55, 76]. The factors to be considered while selecting an infrared sensor are the temperature range, geometry of the surface, lens focal length, measuring angle, surface morphology, and emissivity of the material, spectral range of the measurement and thickness of the material. Thermal radiation in the environment surrounding the target should also be considered. To prevent inaccuracy in the measurement, the infrared sensor compensates the influence of ambient temperatures by measuring the temperature of the optical head and surrounding by a second detector [76]. To improve the accuracy of the measurement, the target is placed in the field of view (FOV) of the instrument.

Several advantages offered by the use of infrared sensors include noncontact temperature sensing, fast response, no risk of contamination, high temperature measurements (3000°C) and facilitating the measurement of hazardous or physically inaccessible objects. Figure 47 (a) shows the infrared temperature sensor deployed in the annealing system. The infrared sensor has two laser guided beams which merge at a specific length (focal length) on the heated object for precise measurement. This sensor is specifically designed to measure temperature of metals or shiny targets having low emissivity (Model: CTLM-3LCF1-60-C3). This sensor has an added advantage of reading temperature of targets through the quartz enclosures [75, 76]. A quartz enclosure has been used in the setup to reduce noise in the stress signal and reduce the temperature

losses due to convection. The quartz cell used is a rectangular spectrophotometer cell by Starna Cells (Model: 1/I/20). Figure 47 (b) shows the quartz cell enclosure with the sample to be annealed [55].

(a) (b)

Figure 47. (a) Infrared sensor deployed in the annealing system to read the temperature from the surface of the annealed sample. (b) Quartz enclosure

iii. PID Controller

The controller unit consists of the infrared sensor electronics which sense the temperature and provided a feedback input to the PID Controller. Figure 48 a shows the front panel view of the controller unit whereas Figure 48 b shows the sensor electronics (where we set the parameters such as emissivity). The output from the PID controller is a relay (on-off switch) which controls the power supply of the infrared heat source. The controller is programmed by setting parameters such as SV (set value) which is automatically tracked by PV (present value) according to the provided ramping parameters such as ramp time, hold time and number of cycles [77].

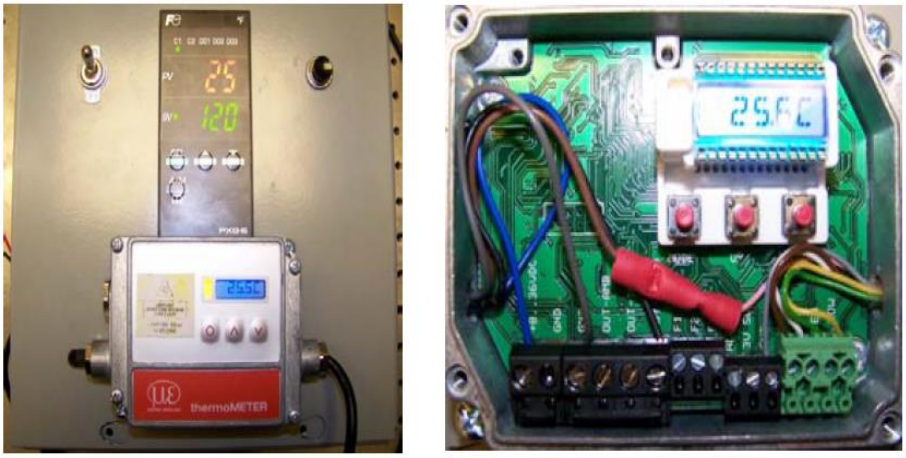

(a) (b)

Figure 48. (a), (b) PID controller comprising of the Infrared sensor electronics.

The on-off relay control is a simple negative feedback control. When the process variable (PV) is less than the set point (SP), the controller output is switched ON and PV goes above SP. Conversely, when PV is above SP, the controller output is switched OFF. The sinusoidal cycling is a typically used on-off control which can be used in systems where the periodic time is large (the system operation is slow) [77, 78]. The improvement in the control system with regards to signal to noise ratio and speed of operation can be done by the use of a proportional control. In proportionate control, the error signal is taken into account while considering the feedback. Proportional control stabilizes the error, does not remove it. So, in order to restore the process to the set point after a disturbance (interruption), the proportional action is sufficient. The additional control signal known as reset is used to reset the process to the set point [55, 77, and 78]. Mathematically, reset signal is an integration of the error signal to zero. Hence, a combination of the

proportional and reset control is known as proportional integration or PI control. Figure 49 shows the PI controller deployed in the system.

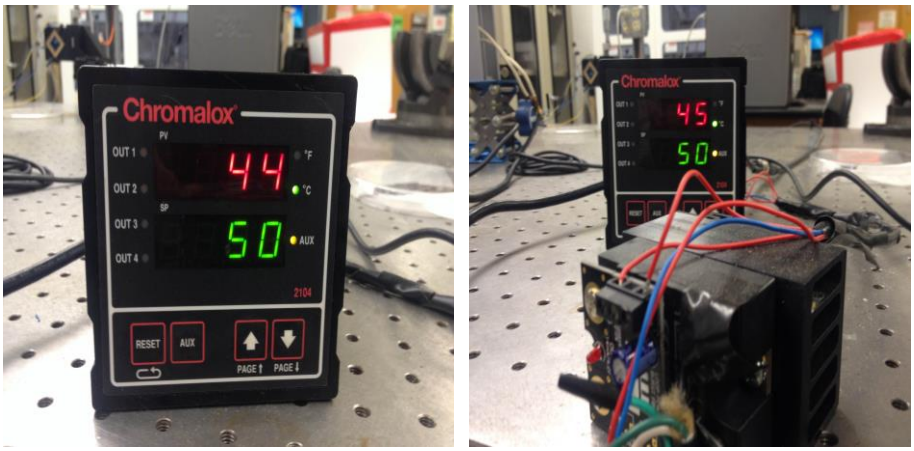

(a) (b)

Figure 49. (a), (b) PID controller with the user interface module

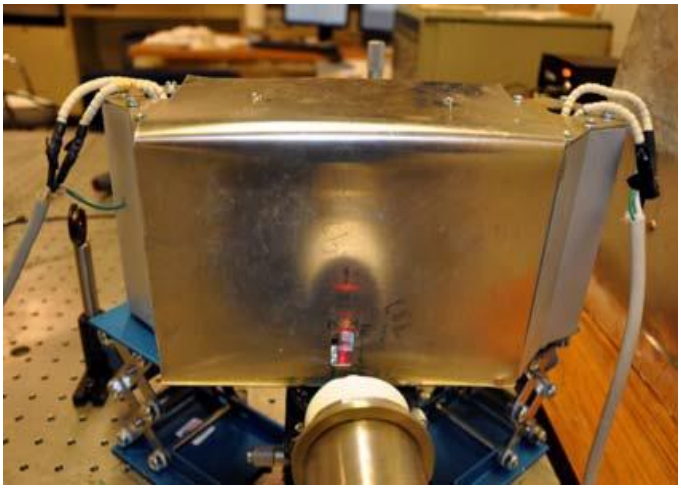

Figure 50. Infrared heat source and the quartz cell enclosed in a shield.

The further improvement in the annealing setup is achieved by shielding the infrared heaters and the quartz enclosure as shown in Figure 50. The accuracy of the infrared

temperature sensor is calculated by using a thermocouple as another temperature sensor in the annealing system.

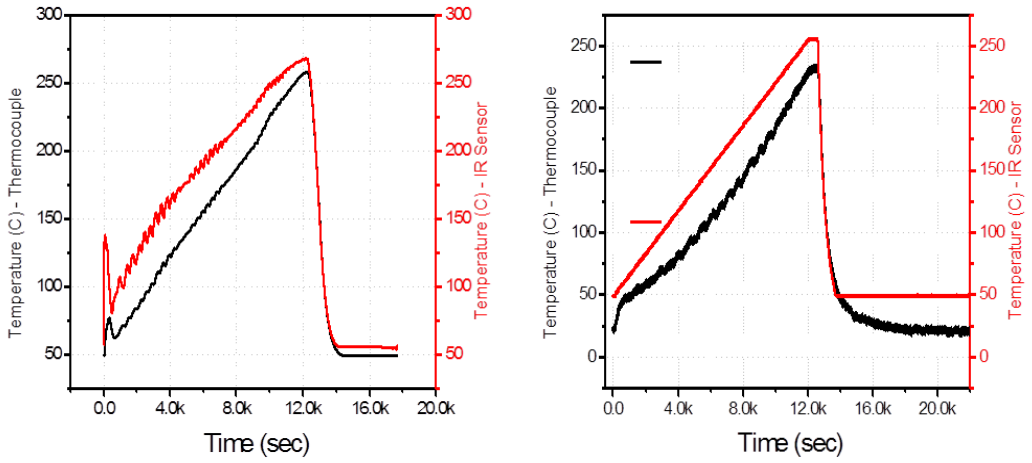

(a) (b)

Figure 51. (a) Thermocouple provides the feedback control (b) Infrared sensor provides the feedback control (Ramp rate for both annealing experiments is 1 C).

Results show that the temperature offset becomes negligible when the sensors are shielded as shown in Figure 50. The slight difference between the temperature reading from the IR sensor and the thermocouple is due to the slow response time of the thermocouple. Figure 51a shows the comparison of temperature measurements when the feedback to the controller is by the thermocouple. Figure 51b shows the comparison of the temperature measurements when the feedback to the controller is by the infrared sensor.

5.3. EXPERIMENTAL PARAMETERS AND TECHNIQUES FOR QUALIFICATION

5.3.1. Design of electroplating solution and process parameters

The first step in the fabrication of ferromagnetic CoFeNi alloys is the design of an optimum electroplating solution to yield alloys with desired physical and metallurgical properties. This section discusses the various parameters considered and optimized during the electroplating solution design.

5.3.1.1. Varying the buffers

As explained in Chapter 2, buffers are used in the electroplating solution to regulate the pH during electrodeposition [25]. Boric acid (H_3BO_3) and ammonium chloride (NH_4Cl) are the traditionally used buffers in the electroplating solution used to fabricate ferromagnetic alloys. However, boric acid is not an environmental friendly chemical and can cause potential risks to humans if subjected to longer exposure. Hence, there is a need to study different chemicals which can substitute boric acid in the plating solution. Different buffers such as acetic acid, citric acid, sodium acetate, sodium chloride are studied and their on the magnetic, crystallographic and electrical properties of the electrodeposited CoFeNi is investigated. Once the right pair of buffers is selected, the buffer concentration is adjusted in order to accurately yield the desired pH value of the solution.

5.3.1.2. Varying the metal ion concentration

The phenomenon governing the electrodeposition of the binary and ternary ferromagnetic alloys is known as anomalous co-deposition [14, 15, and 20]. As explained in Chapter 2,

this phenomenon largely affects the composition and the properties of the alloy. The salts of metals, namely iron chloride tetra hydrate ($FeCl_2$. $4H_2O$), cobalt chloride hexahydrate ($CoCl_2.6H_2O$) and nickel chloride hexahydrate ($NiCl_2.6H_2O$) are used as source of metal ions in the CoFeNi plating solution. Varying the concentration of these metal ions in the solution directly affects the composition of the electrodeposited CoFeNi alloy. In addition, the magnetic, electrical and crystallographic properties also vary depending on the composition of the CoFeNi alloy.

Initially, the concentration of Ni, Co and Fe salts used in the solution is 45g/L, 45g/L and 9g/L respectively. The concentration of Ni is varied from 45g/L to 80g/L and its effect on the composition and metallurgical properties of the CoFeNi is investigated. Similarly, Fe and Co concentrations are varied from 9g/L to 30g/L and 45g/L to 60g/L respectively and the impact on the properties of the electrodeposited CoFeNi alloys is studied.

5.3.1.3. Varying the additive concentration

The role of additives in the electroplating solution is well explained in Chapter 3. Saccharin is a commonly used additive in the electroplating solution to fabricate ferromagnetic alloys [15, 20, and 29]. The other widely used additives are Thiourea, EDTA and L-Cysteine. The concentration of additives in the electroplating solution needs to be optimum in order to have the desired effects on the properties of the deposited alloy.

For designing the plating bath for CoFeNi alloys, saccharin is the preferred additive. Saccharin concentration in the electroplating solution is varied from 0g/L to 2g/L and its effect on the deposited stress, composition, physical and metallurgical

properties of the CoFeNi alloys is investigated. The effect of incorporation of other additives such as Thiourea and EDTA is also studied and an optimum additive concentration is used in the plating bath to achieve the desired properties of the CoFeNi alloys.

5.3.1.4. Varying Current Density

Various researchers have studied the effect of the applied current density on the physical and metallurgical properties of the electroplated ferromagnetic alloys. According to Faraday's law, the relation between the applied current density and the plating rate is given by,

$$Rate = \frac{j \cdot t}{c \cdot F} \quad . \qquad \text{Equation 100}$$

Here, j is the current density in mA/cm^2, t is the time in seconds, c is the ionic charge in the solution and F is the Faraday's constant (96485 C/mol). From Equation 100, it can be derived that an increase in the applied current density improves the deposition rate. For industrial applications, low deposition rate is undesirable because of the increase in operating and manufacturing cost [29]. Hence, controlling the current density can help in achieving higher deposition rates. Also, Horkans et al have attempted to explain the effect of current density on the Fe composition in NiFe alloy [79]. Their study shows that the Fe % in the NiFe alloy increases with increase in the plating current density. However, it is important to note that the current density is not the only parameter that affects the composition. As explained previously, parameters such as pH, agitation also have a significant impact on the composition of the alloy.

Considering the influence of the applied current density on the properties of the electrodeposited alloys; the current density is varied from 5.4mA/cm^2 to 12mA/cm^2 in

steps of 0.6mA/cm^2 during the fabrication of CoFeNi alloys. Potentiostat 273 A is used to control the current density during the deposition and the potential transients are recorded using a Picoscope 2000 DAQ card. The magnetic, electrical and the metallurgical properties of the plated CoFeNi films are studied corresponding to the current density.

5.3.1.5. Varying pH

As explained in Chapter 2, the reaction rate for Co, Fe and Ni reduction is pH dependent. At pH 3.5 or higher, undesirable precipitation of iron hydroxide may occur and for pH below 2.0, the current efficiency of the CoFeNi electrodeposition is undesirably low to due to hydrogen evolution at the cathode [4]. Hence, the pH of the CoFeNi plating solution is usually maintained between 2.0 to 3.5. Typically, the pH during electrodeposition is tightly controlled by use of the buffers in the plating solution as explained in Chapter 2. In this study, the pH of the plating solution is varied between 2.7 and 3.5 and its effect on the properties of the electrodeposited CoFeNi alloys is investigated. The instrument used for pH measurements is the pH meter manufactured by Mettler Toledo Inc. Before every pH measurement, the meter is first calibrated using a three point reference method; wherein the pH of three standard buffer solutions, buffer 4.0, buffer 7.0 and buffer 10 is used to calibrate the pH meter. The reference buffer solutions are changed every two weeks to obtain a high level calibration of the pH meter.

5.3.2. Thin Film Thickness Determination

The electrodeposition rate of the CoFeNi alloy is determined by the charge stripping calculations using the linear sweep voltammetry technique. The film thickness is further verified by milling a cross section of the deposited film using Focused Ion Beam (FIB).

5.3.2.1. Linear Sweep Voltammetry

Linear sweep voltammetry is an electrochemical technique used to detect the change in the current when the potential applied to the working electrode is swept in a given limit [9]. The potential of the working electrode is varied linearly with time between the limiting values, i.e., the initial potential (E_0) and the final potential (E_f). The voltammetry depends on the rate of the electron transfer reaction, the chemical reactivity of the electroactive species and the scan rate. In this research, the voltammetry technique is used to measure the deposition rate and apparently the film thickness during electrodeposition.

5.3.2.2. Charge Stripping Voltammetry

The film thickness can be determined by using the linear sweep voltammetry technique and is called as the charge stripping measurements. In this method, it is assumed that the total mass deposited is proportional to the charge passed through the solution. The total charge during electrodeposition is used up for two reactions occurring parallel, metal reduction and hydrogen evolution. As explained in chapter 2, hydrogen evolution during electrodeposition significantly reduces the current efficiency ($\gamma<1$). Charge during deposition can be calculated as,

$$Q_{dep} = J_{dep} \cdot t \quad . \qquad \text{Equation 101}$$

Here, J_{dep} is the current density during deposition and t is the time of the electrodeposition. This charge is combination of charge due to metal deposition and hydrogen evolution reaction given as,

$$Q_{dep} = Q_M + Q_{H_2} \quad . \qquad \text{Equation 102}$$

To calculate the charge during deposition for CoFeNi alloy, a constant current density of 9.6mA/cm^2 is applied to the working electrode using a Princeton E&G 273 Potentiostat. The working electrode for this experiment is a Pt (RDE) electrode. The counter electrode is 99.99% pure nickel electrode. The time for deposition is set to 20 minutes. Figure 52 shows a typical potential transient recorded by Picoscope 2000.

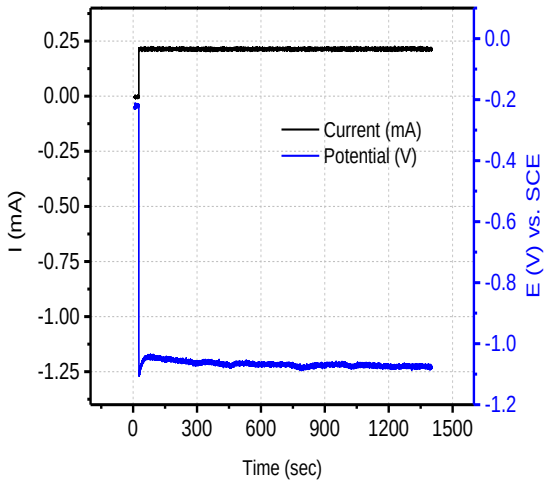

Figure 52. Transients for Galvanostatic Electrodeposition

The CoFeNi alloy deposited on the Pt (RDE) electrode by galvanostatic electrodeposition is then stripped in the same electroplating solution by applying a sweep potential from -700 to +600mV. The scan rate for the applied sweep is 5mV/s. eDAQ software is used to record the charge stripping curve as shown in Figure 53. The stripping charge is the integral of the curve shown in Figure 54 and can be written as [8],

$$Q_{strip} = \int \frac{I \cdot dE}{Scan\ rate} \ . \qquad \text{Equation 103}$$

As explained in Chapter 2, current efficiency can be defined as the ratio of charge during stripping to the charge during deposition. It can be expressed as,

$$\gamma = \frac{Q_{strip}}{Q_{dep}} \ . \qquad \text{Equation 104}$$

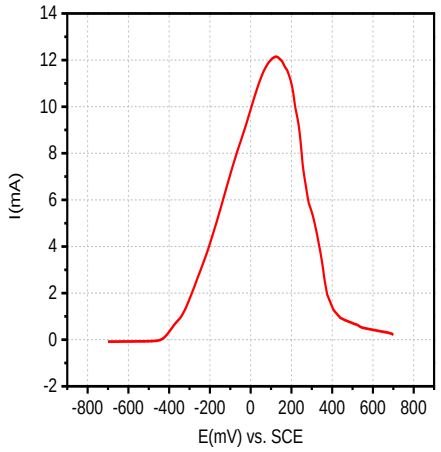

Figure 53. CoFeNi alloy charge Stripping Curve

The film thickness is calculated once the current efficiency is obtained. The total film thickness can be expressed in terms of the current efficiency and the current density as,

$$Film\ Thickness(T) = \frac{J_{dep} \cdot \gamma \cdot t \cdot v_m}{n_e \cdot F} \ . \qquad \text{Equation 105}$$

Here, t is the time of electrodeposition, v_m is the molar volume, n_e is the number of electrons transferred during the reaction and F is the Faraday's constant.

5.3.2.3. Film Thickness Verification by Focused Ion Beam

The film thickness measured by charge stripping voltammetry is confirmed by making a cross section on the film using FIB. Several cross sections are made on one film and then the average thickness is calculated. The FIB used for thickness measurements is a Dual

beam FEI with gallium (Ga^{2+}) ion source. In order to measure the thickness, we image a cross section at a particular location of the film by milling a certain area (few microns) of the sample [80].

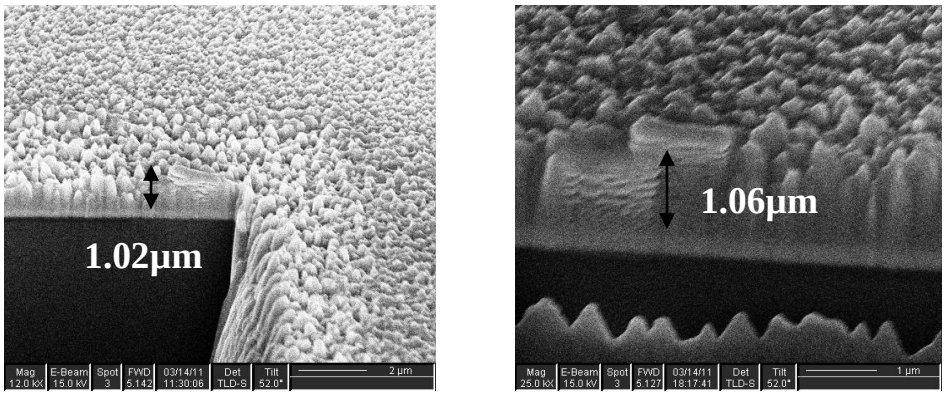

(a) (b)

Figure 54. Film thickness verification using FIB (a) Cross section at one location of CoFeNi film electrodeposited with thickness of 1µm (b) Cross section at second location of the same film.

For this step, a high ion beam current, typically 20nA – 50nA is used. The next step in this process is to do a cleaning cross section by using a slightly lower beam current of about 50pA. In order to be able to distinguish between several layers in the image and making the measurements more accurate, a thin layer of Pt (few orders of nanometers) may be deposited. An electron beam powered at 15kV is used to image the cross section. With the help of the joystick, the focus is adjusted and a clear, detailed image of the cross section is obtained. The electron and the ion beam are at an angle of 52^{o} and hence, it is necessary to consider the tilt angle correction while calculating the dimensions from the cross section. Figures 54a and 54b are SEM images of the cross section of electrodeposited CoFeNi film at two different locations on the film. The deposition rate of the alloy was calculated using charge stripping measurement and hence, the alloy was

the deposited accordingly to yield a thickness of 1μm. The error in the thickness analysis recorded is about 5%.

5.3.3. Varying Resistivity Measurements

The Jandel HM-21 four- point probe measurement set up has been used for measuring the sheet resistance of the electrodeposited CoFeNi films. Figure 55a shows the four point probe head. The probe head is a handheld instrument, which needs to be pressed on the sample to measure its resistivity. The outer two probes apply a constant current whereas the inner two probes measure the voltage drop across the sample surface. Figure 55b shows the way in which Jandel HM-21 reads data from the four-point probe.

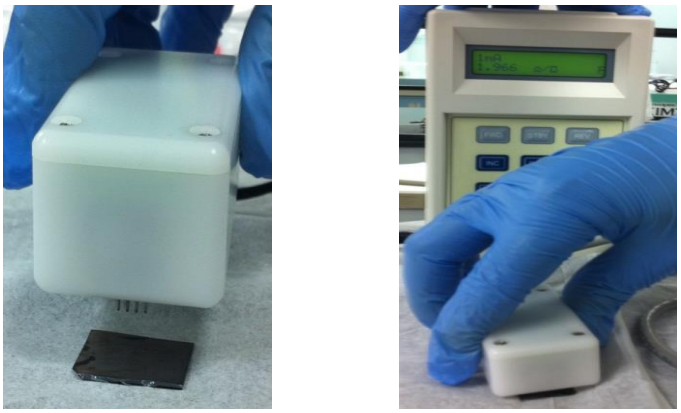

(a) (b)

Figure 55. Jandel HM-21 four point probe setup (a) four point probe head (b) probe head pressing on the sample and the Jandel HM-21 meter recording the sheet resistance.

Every time before it is used, the set-up is calibrated with a standard 13.2mΩ provided by Jandel. The thickness of the sample is measured using the charge stripping method and is

verified by the focused ion beam (FIB). As the CoFeNi thin film is highly conductive, a higher current range of 10mA is selected for measuring the sheet resistivity. The probe head is pressed on the sample and the sheet resistance is recorded. As the thickness of the sample is non-uniform due to the stagnant electrodeposition, accurate value of resistivity cannot be determined by measuring sheet resistance at one place on the sample. Hence, to improve the accuracy of the measurement, 50 measurements are done on the sample at different places. A histogram is plotted to show the distribution of the sheet resistance on the sample as shown in Figure 56.

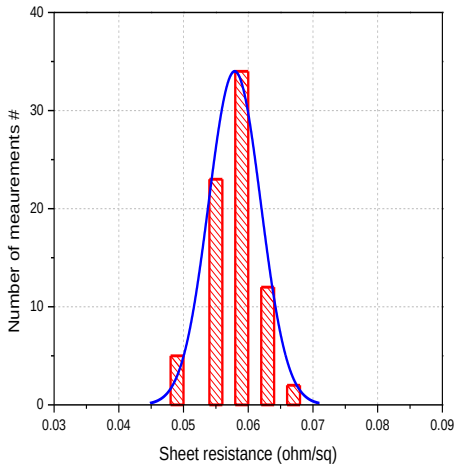

Figure 56. Distribution of sheet resistance over the sample surface.

The distribution shows that the sheet resistance of the thin film is not a uniform property along its dimensions but varies significantly with the thickness of the film. Understanding that the film is deposited by stagnant electrodeposition technique, one can assume a non-uniformity in the film thickness around the film edges. The plot shown in Figure 56 well explains the dependence of sheet resistance on the thickness of the electrodeposited film. Knowing the physical properties of the sample (CoFeNi film), namely the length, width

and the thickness, the resistivity can be from the sheet resistance by the formula derived in Chapter 4.

5.3.4. Composition Characterization by EDX

The composition of electrodeposited CoFeNi alloy largely influences its magnetic, electrical and structural properties. Thus, knowing the exact composition of the alloy is very crucial to achieve the desired physical and metallurgical properties. Energy Dispersive X-ray Spectroscopy (EDS) is an analytical technique used for composition characterization in this research [81]. The EDS makes use of the X-rays emitted by a solid sample bombarded with high energy focused beam of electrons to obtain chemical analysis. Elements with atomic numbers 4(Be) to 92(U) can be detected using this technique, though not all instruments are equipped to trace 'light' elements (typically with atomic number < 10) [81].

5.3.4.1. Principle and Working

The composition characterization technique in electron microscopy is based on Moseley's law, $v = 2.46*10^{15}(Z-1)^2$ which relates the frequency of the emitted X-ray radiation to the atomic number of the element [81, 82]. When a high energy electron beam is incident on the sample surface, the electrons from the lower energy level are excited and get ejected from the shell. The vacancy so formed in the lower energy level is filled by an electron from a higher energy level releasing energy during this process. This energy difference between the two levels is released in the form of X-rays and is detected by the EDS detector attached to the SEM.

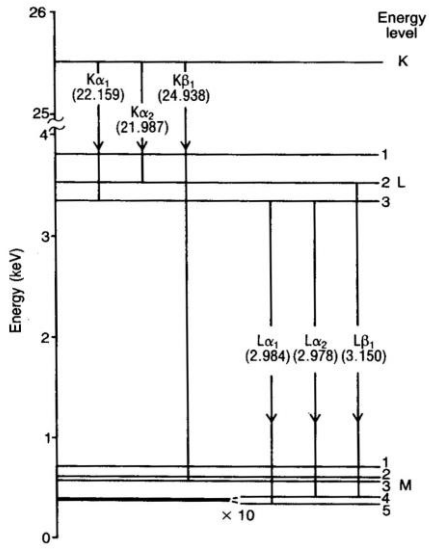

Figure 57. Energy level diagram for Ag showing transitions [82].

The detector typically used for X-ray detection purpose is a Lithium drifted silicon solid state X-ray detector. X-ray lines are identified by a capital Roman letter indicating the shell containing the inner vacancy (K, L or M), a Greek letter specifying the group which the line belongs in order of decreasing importance α, β etc. and a number denoting the intensity of the line within the group in descending order (1,2, etc.). Thus, the Kα1 line is more intense than Kα2 line and hence is rarely resolved. Characteristic spectra may be understood by reference to the energy level diagram as shown in Figure 57. The horizontal lines represent the energy of the atom with an electron removed from the shell. An electron transition associated with an X-ray emission can be considered as transfer of a vacancy from one shell to another. Energies are measured in electron-volts (eV), 1 eV being the energy corresponding to a change of 1V in the potential of an electron ($1.602*10^{-19}$ J). The specific energy of each characteristic peak is compared with the reference peak information. One of the main advantages of EDS is that the spectrum of X-rays is obtained in a very short time. However, the relatively poor energy resolution of

the EDS (as compared to WDS) causes frequent spectral interference problems. Also, the inability to separate peaks at lower energies adds to the limitations of the EDS. For elements having the peak energy above 3eV, the energy separation of the family members is such that despite the peak broadening, it is possible to recognize more than one peak, even if they are not completely separated as shown in Figure 58a [82]. The X-ray spectrum for Tantalum showed greater separation of peaks resolved as shown in Figure 58a, while Silicon showed only on peak with Kα and Kβ peaks unresolved.

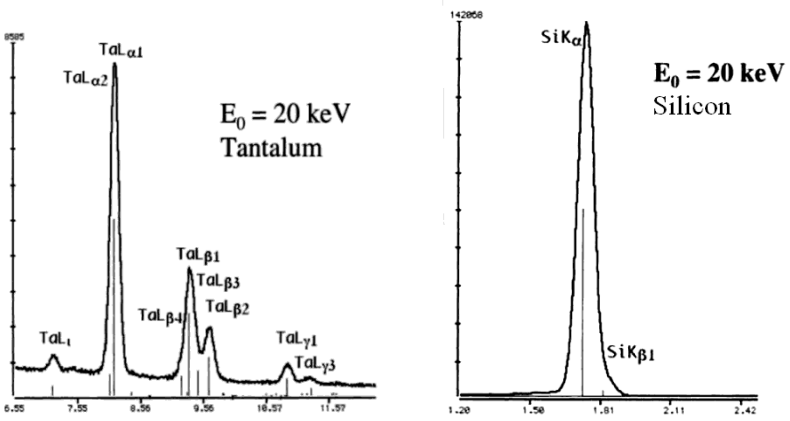

(a) (b)

Figure 58. (a) X-ray spectrum for Tantalum showing resolved, distinct peaks (b) X-ray spectrum for Silicon showing only one peak with Kα and Kβ unresolved [81].

The following spectrum shown in Figure 59 is obtained during composition analysis of a CoFeNi thin film. The analysis is done using a JEOL JSM 6330 Field Emission SEM. The accelerating voltage for the electrons is 15keV and the working distance used for imaging is 15mm.

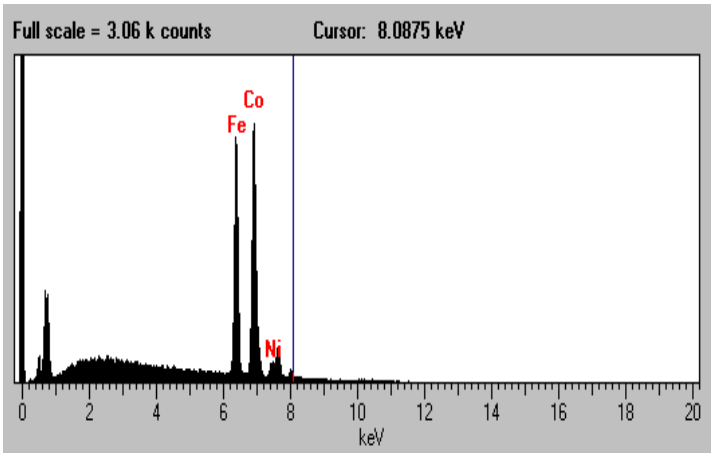

Figure 59. EDS spectrum for CoFeNi alloy electrodeposited from a solution containing 2g/L additive Saccharin.

The X-ray energy level is a characteristic of a particular element which helps to identify the element present. The intensity of the peak is used to determine the composition or the atomic percentages of the elements present. Figure 8 shows peaks for different elements (including some impurities) corresponding to different yet distinct energy levels. In Figure 59, the peak corresponding to energy of 6.3keV is iron, 6.9keV is cobalt and the peak corresponding to energy of 7.5keV is nickel. The composition analysis is done at several locations on the sample, to check the uniformity in the composition. The signals are collected for 100seconds at each location on the sample.

5.3.5. X- Ray Diffractometer – grain size and crystal structure

X-rays were discovered in 1895 by a German physicist Roentgen and were so named because their nature was unknown at that time. Unlike ordinary light, these rays are invisible, but they traveled in straight lines and affected photographic films in the same way as light. On the other hand, they are much more penetrating than light and could easily pass through human body, wood, thick metal pieces and other opaque

objects [83]. Due to their penetration capabilities, X-rays are used for research purposes to study different characteristics of a material by a technique known as X-ray diffraction. This technique was first used in von Laue's discovery in 1912 to show that crystals diffract X-rays and the manner of diffraction depends on the structure of the crystal. Earlier, this technique was used only to study the crystal structure of a material. Later on, however, the application of this technique was extended to diverse problems such as grain size determination, stress measurement and chemical analysis of the material.

5.3.5.1. Principle and Working

The instrument used for studying the X-ray diffraction is known as the X-ray diffractometer and it works on the Bragg's law of diffraction. This tool uses X-rays of known wavelengths to determine the unknown spacing of crystal planes and gives information about the orientation of the grains and grain size. Consider a crystal lattice which has a thickness *t*, measured in a direction perpendicular to a set of reflecting planes. Let the number of planes in a set be m+1. We will regard Bragg angle (θ) as a variable and θ_B is the angle which satisfies the Bragg law for particular values of d and λ such that [83],

$$n \cdot \lambda = 2d \cdot \sin\theta_B \ . \qquad \text{Equation 106}$$

Thus, by varying either λ or θ, the Bragg law can be satisfied for any given crystal to study its structural properties. From Figure 60a, rays A, D make exactly angle θ_B with the reflecting planes. The angle between the incident beam and the transmitted beam is the diffraction angle, which is calculated to be 2θ. Hence, at a diffraction angle of $2\theta_B$, diffracted rays A' and D' are in-phase (constructive interference), forming a diffracted beam of maximum amplitude (i.e. maximum intensity because intensity is proportional to

square of the amplitude). The width of the diffraction curve increases as the thickness of crystal decreases and is expressed as B [83]. The diffraction width is measured at an intensity equal to half the maximum intensity (full width half maximum). From Figure 29b,

$$B = \frac{1}{2}(2\theta_1 - 2\theta_2) \qquad \text{Equation 107}$$

and $$B = \theta_1 - \theta_2 \ . \qquad \text{Equation 108}$$

The path difference for these two angles θ_1 and θ_2 can be calculated as,

$$2t\sin\theta_1 = (m+1)\lambda \qquad \text{Equation 109}$$

and $$2t\sin\theta_2 = (m-1)\lambda \ . \qquad \text{Equation 110}$$

Subtracting Equation 109 and 110,

$$t(\sin\theta_1 - \sin\theta_2) = \lambda \ . \qquad \text{Equation 111}$$

Using the trigonometric identity**,**

$$\sin C - \sin D = 2\sin\left(\frac{C-D}{2}\right)\cos\left(\frac{C+D}{2}\right)$$

$$2t\sin\left(\frac{\theta_1-\theta_2}{2}\right)\cos\left(\frac{\theta_1+\theta_2}{2}\right) = \lambda \ . \qquad \text{Equation 112}$$

Now, θ_1 and θ_2 are nearly equal to θ_B. Hence, the above expression can be reduced to,

$$2t\left(\frac{\theta_1-\theta_2}{2}\right)\cos(\theta_B) = \lambda \ . \qquad \text{Equation 113}$$

Now, from Figure 60b, $\left(\frac{\theta_1-\theta_2}{2}\right)$ = full width half maximum (B). Substituting in Equation 113, we get the final equation for the thickness in terms of the X-ray wavelength (λ), Bragg's angle (θ_B) and the full width half maximum (B) as,

$$2tB\cos(\theta_B) = \lambda$$

$$t = \frac{\lambda}{B\cos(\theta_B)} \quad . \qquad \text{Equation 114}$$

A more exact formula can be derived by including the shape factor (commonly assumed to be 0.9). Following is the final expression for the grain size [12],

$$t = \frac{0.9 * \lambda}{B\cos(\theta_B)} \quad . \qquad \text{Equation 115}$$

Equation 115 is known as the Debby-Scherer formula and is very commonly used for grain size calculations.

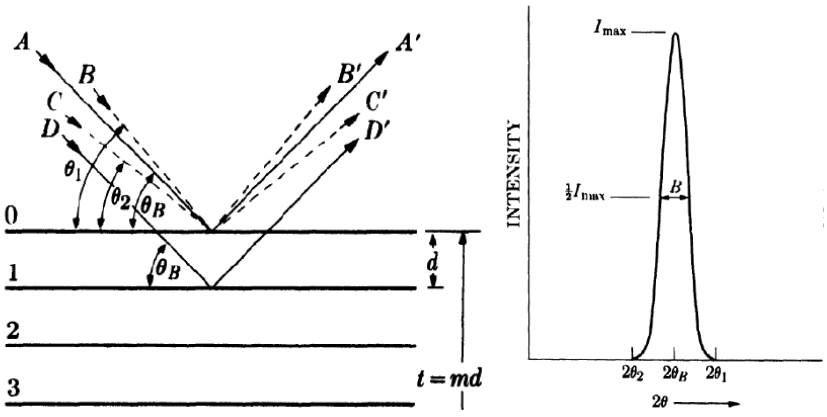

(a) (b)

Figure 60. (a) Diffraction of incident beam in agreement with Bragg's law to yield constructive interference (b) A typical XRD peak in a plot of Intensity vs. 2θ [83].

A Siemen's D5000 Powder X-ray Diffractometer is used for determining the crystal structure and the grain size of the electrodeposited CoFeNi film. Cu K-α radiation of wavelength 1.541 A^o is used as X-ray source. The current and voltage applied to the source are 30mA and 40keV respectively. The θ-2θ scan is performed between 30^o and 60^o with step size of 0.04 radian and hold time of 2minutes. Using the ICDD database, the peaks are identified and the strongest peak is fitted with a Gaussian equation.

Tablecurve 2.0 is used to determine the fit parameters and to obtain the full width half maximum (FWHM) of the curve. By using the Debby-Scherer formula derived in Equation 115, the grain size of the electrodeposited CoFeNi film is calculated.

5.3.6. Magnetic Moment Measurements

The magnetic characterization of the electrodeposited CoFeNi thin films is carried out using a Lakeshore 7400 series VSM. Extensive efforts are taken to electrodeposit the samples with a specific shape and volume so that the moment calculations could be accurate. Following section explains the routine implemented for accurate moment measurements.

5.3.6.1. Wafer cleaning and oxide etch

The requirements for device performance and reliability in the VLSI and ULSI circuit technology have increased progressively. Wafer cleaning processes are hence given more emphasis during the fabrication process. Wafer cleaning is one of the most repeated steps in the IC device fabrication process and careful measures are taken at every fabrication step to keep the wafer away from impurities [66]. Although there are many methods of wafer cleaning, a wet cleaning approach is adopted. The starting wafer is a 3" antimony doped n-type Si (100) wafer from Silicon Quest Co., with a resistivity of 0.01-0.02 Ω-cm as shown in Figure 61.

Figure 61. Blank Si wafer with a thin layer of native oxide (5-10nm)

The wafer is first rinsed with acetone and then dipped in 10% buffer hydrofluoric acid (HF) for 10-15 seconds.

Figure 62. Clean and contaminant free Si-surface

HF is a strong acid and should be handled with extreme care by wearing protective goggles and clothing. The buffer HF etches away the native oxide and any other contaminants on the wafer surface as shown in Figure 62. The wafer is then rinsed thoroughly with deionized (DI) water. A wetting test is performed to check if the wafer is free of the oxide layer [66]. Oxide is hydrophilic and pure silicon is hydrophobic. On rinsing the silicon wafer with DI water, if the water beads up and rolls off, the surface is hydrophobic indicating that the surface is oxide free. The test to check if the wafer is devoid of oxide or contaminants is to see if there are any droplets of water sticking on the wafer surface.

5.3.6.2. Deposit Seed layer

The AJA Ultrahigh Vacuum DC magnetron sputtering system is used to deposit the seed layers tantalum (Ta) and copper (Cu) on the clean Si wafer. The base pressure for the sputtering is $1*10^{-8}$ Torr. Table 2 lists the percent power and the sputtering rate for the Cu and Ta layers. Using the computer user-interface, the design recipe for the sputtered layers is input in the program and a separate file is created which includes specific details about the target, DC power source, sputtering time and order of multilayer sputtering. The first metal layer deposited is Ta of thickness 30nm that works as an adhesive layer to improve the bonding between the Cu layer and Si wafer.

Table 2. Sputtering rates for the seed layers

Sputtered layer	Percent Power	Sputtering Rate
Ta	30%	1.0A/s
Cu	30%	2.5A/s

Ta sputtering is done in two stages. The first step is called as Ta pre-sputtering. When the sputtering is started, the target does not heat up immediately and hence, the desired thickness might not be obtained (especially if thin layers of few nm need to be deposited).

Figure 63. Sputtered Ta (30nm) and Cu (300nm) seed layers.

Therefore, pre-sputtering step is implemented wherein the plasma is turned ON and the target is heated. The pre-sputtering step is normally carried out for 30seconds. The actual

sputtering takes place in the second stage and to deposit 30nm Ta, the sputtering time is 300seconds. Similarly, a 300nm Cu layer is sputtered in two stages.

5.3.6.3. Spin coat photo resist AZ1512

After the metal layers are sputtered, the next step is photoresist AZ 1512 coating. It is a positive photoresist manufactured by AZ Electronic Materials. The detailed description about the thickness vs the spin speeds for AZ 1512 is listed in the manual for the photoresist [84]. The process parameters for spin coating 1µm are shown in Table 3. In Table 3, 500rpm is the initial dispense speed and 3000rpm is called as the terminal speed.

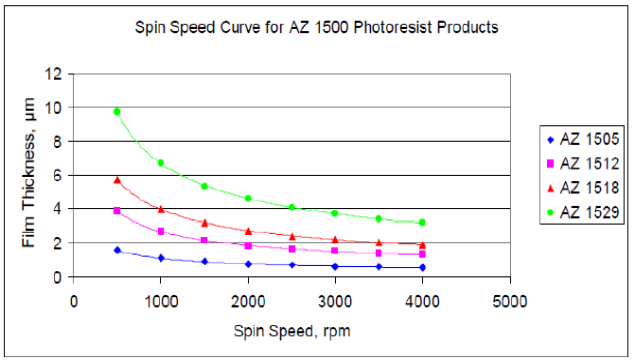

Figure 64. Dependence of the resist thickness on the spin speed [84].

According to the AZ 1512 datasheet, spin speeds between 2000-4000 rpm generate maximum uniformity in the coating and hence, 3000 rpm is used as the terminal speed. The spin curve speed for AZ 1512 is shown in Figure 64 and Figure 65 shows 1µm AZ 1512 spin coated on the metal layers.

Table 3. Spin coating recipe developed for 1µm AZ1512

Speed (rpm)	Time (sec)
500	15
3000	45

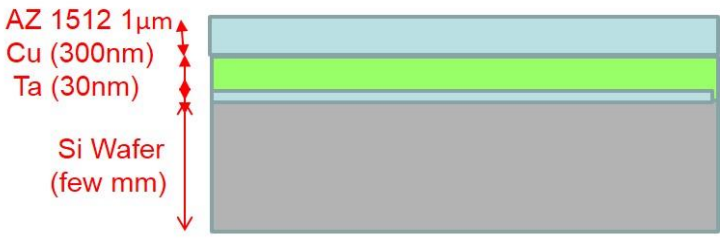

Figure 65. AZ 1512 1µm layer spin coated on the metal seed

5.3.6.4. Pre-bake

Prebake step has a great influence on the final pattern. The primary function of this step is to dry the AZ 1512 film and to fix the development rate of the photoresist. The prebake temperature used in fabrication of the magnetic thin films is 90 C, maintained using a hotplate for 90 seconds.

Figure 66. Hot-plate used to bake the samples at 90C for 90 seconds.

5.3.6.5. Optical Lithography

Optical lithography is performed using ABM mask aligner in the clean room. A photomask is a desired pattern that can be transferred onto a surface using light waves. The mask creates a shadow between the light and the surface blocking sections of light passing through it [66, 85]. Masks can be created by several ways, but one of the most common and accurate methods is by using an electron beam to etch a desired mask or pattern. The mask is aligned correctly in line to the surface by using certain marks on the mask and the surface as a reference. Depending on the way the mask is placed, there are

different ways of lithographic techniques namely contact, proximity and projection lithography. In contact lithography, the mask is in contact with the surface during exposure. For proximity lithography, the mask is close enough but not touching the surface and projection lithography, the mask is not close to the surface and the light passing between them is subject through imaging optics [85].

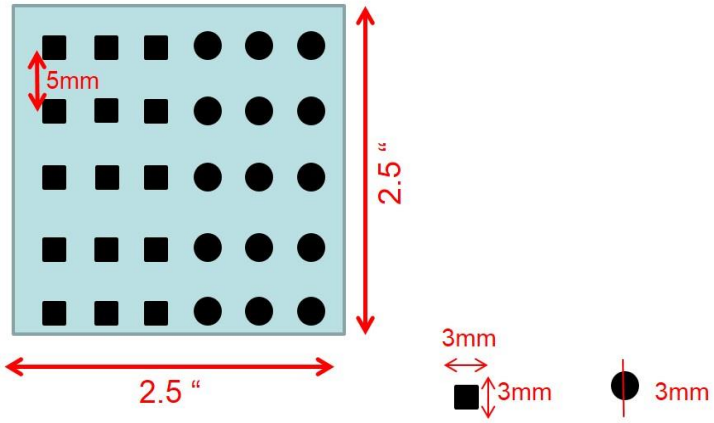

Figure 67. Photolithography mask with the dimensions of the pattern

Using the ABM mask aligner, the pattern is reproduced on the surface using contact lithography technique. The mask shown in Figure 67 is designed by Nikhil Dole and is manufactured by CAD/ART services.

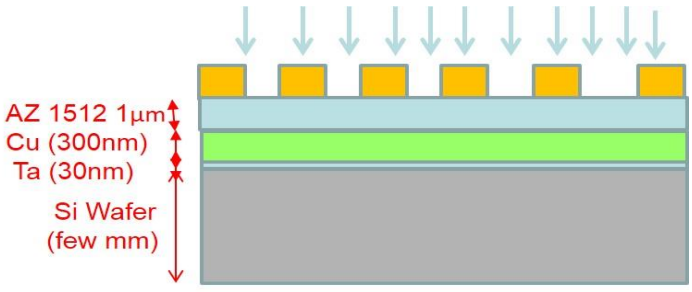

Figure 68. The spin coated sample with the mask in contact with the surface exposed to UV light.

The pattern of the mask is an array of squares and circles as shown in the Figure 67. The dimensions of the square pattern are 3mm * 3mm whereas the circular pattern has diameter of 3mm. A schematic of the exposure to the photoresist covered wafer by UV light through the pattern on the mask as shown in Figure 68. The exposure time is 4 seconds.

5.3.6.6. Development using AZ 300MF

There are two types of photoresist, namely positive and negative resist. In case of a negative photoresist, the molecules in the resist are polymerized (bonded strongly to form long chains) when subjected to UV rays [66, 84]. After the development process, the non-exposed sections of the resist decompose and only the exposed/polymerized resist remains. On the contrary, when a positive photoresist is subjected to UV rays, the exposed section decomposes and the non-exposed section of the resist remains.

AZ 1512 is a positive photoresist. Hence, after the exposure, the sections of the surface not exposed to the UV lights remain intact. The sections of the AZ 1512 resist exposed decompose and are loosely bonded. An AZ 300MF developer is to dissolve the exposed sections of the photoresist. After the development of the photoresist, a patterned sample is obtained as shown in Figure 69.

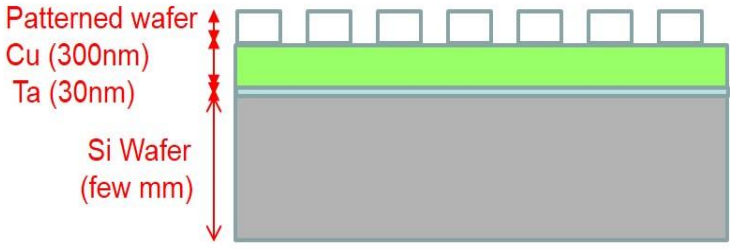

Figure 69. Development of the pattern using AZ 300MF developer.

5.3.6.7. Post-bake

The post-bake is used to stabilize and harden the photoresist. This step is also useful in removing any traces of development chemicals and improving the adhesion of the photoresist to the wafer surface [66, 85]. The samples are baked at 120 C for 2 minutes as shown in Figure 70.

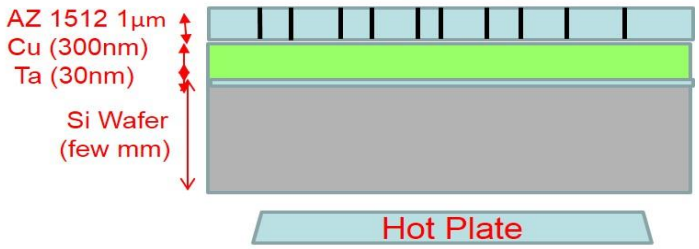

Figure 70. Post-bake the sample to harden the resist

5.3.6.8. Oxygen Plasma Etching

An oxide etch is critical to completely remove the photoresist and the polymer residue after the development process to achieve a reliable metal filling process and a minimal contact resistance.

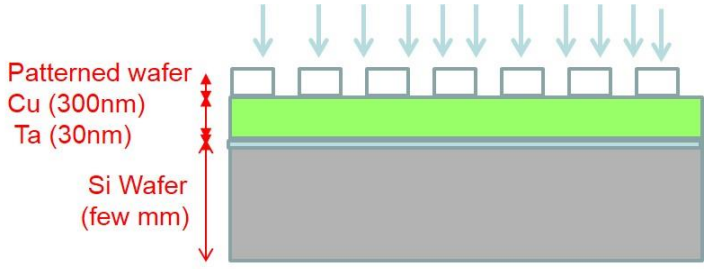

Figure 71. Oxygen plasma etching to remove traces of resist.

Conventionally, the photoresist ashing is done using an oxygen plasma at a high wafer temperature. It has been reported that oxygen atoms rather than the excited state oxygen molecules are the primary reactive species responsible for removal of photoresist in an

oxygen plasma [66]. The developed wafer shown in Figure 70 is then subjected to oxygen plasma etching for 3 seconds. The exposure to oxygen plasma, as shown in Figure 71, etches away the traces of AZ1512 photoresist remaining after the development process.

5.3.6.9. Profilometer

The thickness of the pattern is verified by the profilometer step measurements. Figure 72 shows a typical measurement of the pattern using profilometer.

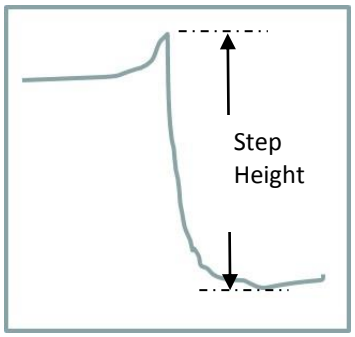

Figure 72. A profilometer plot depicting the surface thickness profile.

5.3.6.10. Electrodeposition

Using the CoFeNi electroplating solution designed using the parameters mentioned in section 5.3.1, thin CoFeNi films are electrodeposited in the patterns prepared. The setup shown in Figure 73a is used to electrodeposit the thin films wherein the working electrode is the patterned wafer, the counter electrode is nickel foil and the reference electrode is saturated calomel electrode (SCE). The thickness of the electrodeposited films is 0.7μm which is maintained uniform throughout the measurements. The step measurements on the profilometer are used to verify the thickness of the electrodeposited films. Figure 73b shows the electroplated wafer after the plating process is completed.

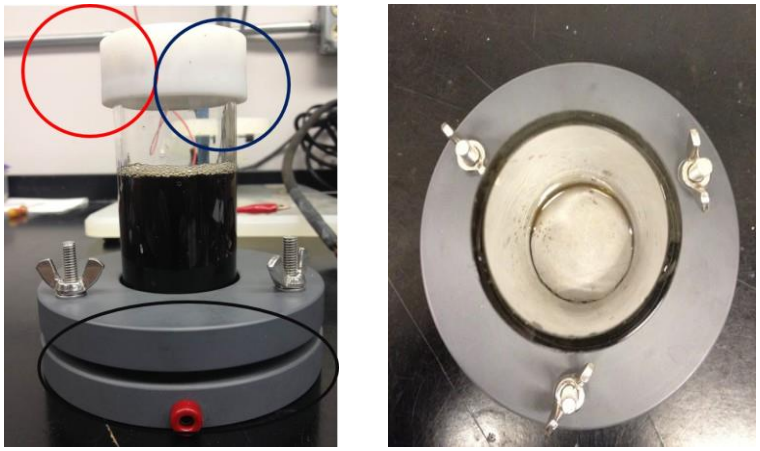

(a) (b)

Figure 73. (a) Wafer electroplating system (b) Electroplated wafer.

5.3.6.11. Etch Photoresist

After the electrodeposition is complete, the remaining of the photoresist is etched away by sonicating the sample in a bath of acetone. Acetone dissolves the photoresist and a clean pattern is obtained. The samples are then washed with DI water and dried with nitrogen. Patterned samples are stored in vacuum to protect oxidation of the Cu layer.

5.3.6.12. Calibration Sample

The electrodeposited CoFeNi thin films are subjected to magnetic moment measurements using the Lakeshore 7400 series VSM. Before proceeding with the characterization of the actual CoFeNi samples, the VSM is calibrated using a electrodeposited Ni (99.99%) sure having the same thickness, size and shape as the CoFeNi samples to be characterized. The field in the VSM is swept from +3000Oe to -3000Oe at a step increase of 2.2Oe/s. the saturation magnetization recorded for the Ni sample is compared with the standard values provided for a NIST sample. The calibration error for the instrument is calculated as,

$$\%error = \frac{actual - measured}{actual} * 100 \ . \qquad \text{Equation 116}$$

The error calculated from Equation 116 is added to all the moment measurements to get the most accurate value of the saturation magnetization of the CoFeNi thin films.

5.3.6.13. Moment Measurements

After the VSM is calibrated with the electrodeposited Ni sample, the CoFeNi thin films are characterized by sweeping the magnetic field in the same range (+3000 to -3000). The coercivity and the saturation magnetization for every thin film is recorded. The effect of saccharin incorporation, annealing and the inclusion of fourth element (CoFeNiX) on the magnetic properties of the CoFeNi alloys is studied using the above explained stepwise procedure.

5.3.7. Strain Annealing of Cu Interconnects

As explained in Chapter 4, the shrinking of the device size leads to a constraint on the size of the Cu interconnects. At nanoscale, researchers have shown an increase in the resistivity of the Cu interconnects and the effect is attributed to the electron scattering at the grain boundaries. A novel concept of strained annealing is used to build the setup to improve the conductivity of the Cu interconnects.

The Si cantilevers are fabricated with Cu-interconnect nanostructures with critical dimensions (CD) 50nm (64nm, 78nm, etc.) as shown in Figure 74. The Cu is electrodeposited using the superfilling process and a proprietary bath design. The length of the copper interconnect structures is of the order of several hundred microns. In order to prevent oxidation, the Cu interconnects are capped with a 100nm SiN protective dielectric layer.

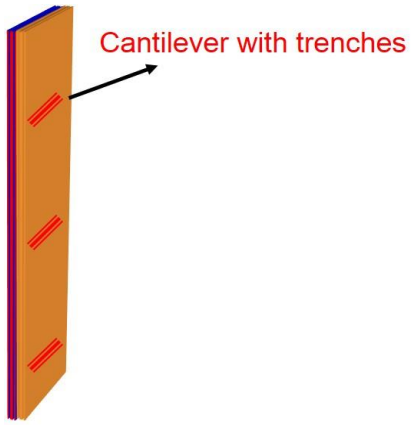

Figure 74. Si cantilevers with Cu interconnects

There are two ways proposed to apply external strain on the cantilevers to promote grain growth via grain boundary densification process. In each approach, the aim is to impose an external strain along a particular (longitudinal) direction (tensile along rr direction, compressive along θθ direction) of the Si cantilever to improve the conductivity of the Cu interconnects.

5.3.7.1. External Strain - Strain Control Layer

In this approach, a strain control layer i.e. an external layer is deposited on the back of the Si cantilever by using e-beam evaporation or UHV sputtering technique. The material for the external layer is chosen by reviewing its coefficient of thermal expansion and the strain imposed on the Cu interconnects. The cross section of the cantilever indicating the most important layers and their thickness is shown in Figure 75. The imposed external strain on Cu interconnects is achieved by stress/strain control layer during annealing which also induces the cantilever bending. The bending occurs along the cantilever long axis (rr-axis) as shown in Figure 76. The stress/strain in Si cantilever develops during the

annealing due to difference in the coefficient of thermal expansion between the silicon and the stress/strain layer control deposited on the back side of the cantilever as shown in Figure 76 [58, 86]. Metals like Ni, Cr, Ta or oxide such as Al_2O_3 having thickness in the range of few microns are deposited on the back of the cantilever using vacuum deposition techniques.

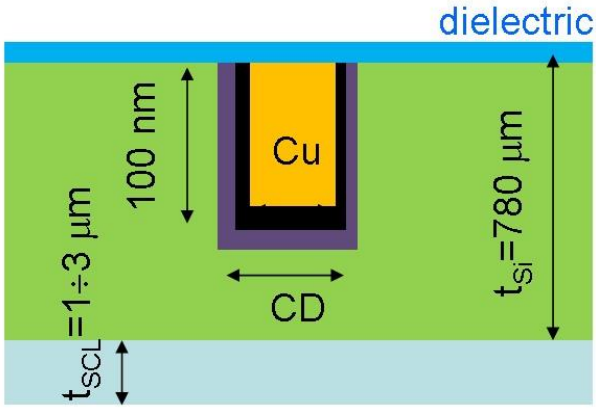

Figure 75: Thickness of the layers in the stack

This allows different values of strain imposed in the Si cantilevers outer surface during annealing. The Cu interconnects are positioned in such way that their longer axis is aligned with the θθ axis of the cantilever as shown in Figure 76. The strain induced in the Cu interconnects during annealing is measured in-situ by a setup based on the cantilever bending technique. The geometry of the system allows a small angle approximation to estimate the curvature of the cantilever directly from the laser displacement on the PSD, d_{PSD}. The curvature of the cantilever is calculated as [55, 67, and 69],

$$\frac{1}{R} = \frac{d_{PSD}}{2 \cdot L \cdot D_{PSD}} \ . \qquad \text{Equation 117}$$

Here, L and D_{PSD} represent the length of the cantilever from the fixture to the place from which the laser beam is reflected and the distance of the cantilever to the PSD respectively. The interface between the Cu interconnect and surrounding SiO2/barrier/seed layer is not compromised and the state of the stress/strain in the surrounding Si is same as in the Cu interconnect.

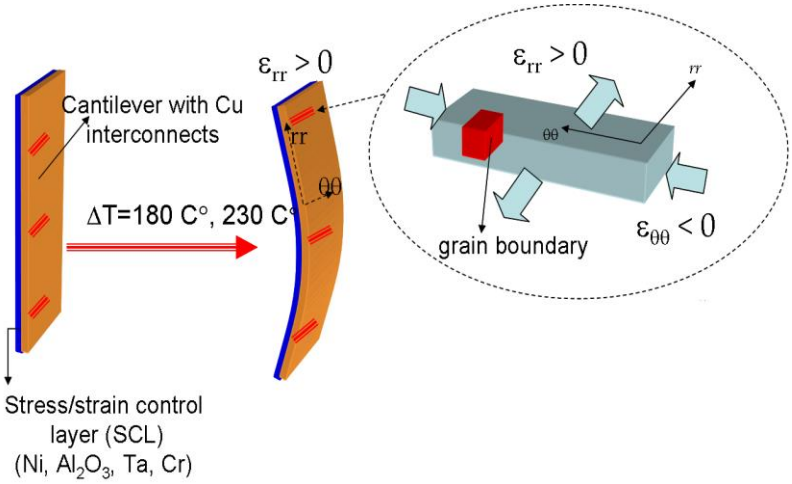

Figure 76. Schematics of Si cantilever indicating the position of the stress/strain control layer, and the orientation of the Cu interconnects with respect to the rr and θθ axes.

Because the thickness of the strain control layer is much smaller (t_{SCL} =1~3μm) than the thickness of the Si cantilever (t_{Si}-780μm), the average value of the imposed external strain ε_{rr} is calculated as

$$\varepsilon_{rr} = \frac{t_{Si} + t_{Cu}}{2 \cdot R} \quad . \qquad \text{Equation 118}$$

5.3.7.2. External Strain – Vise Controlled Strain

In an alternative approach for strained annealing, a new set up has been developed to precisely impose external strain on the Si cantilevers during annealing stage. A specially

designed vise that can apply strain in longitudinal direction has been machined and implemented in the experimental set up for curvature evaluation during annealing of the Si cantilevers as shown in Figure 77. The imposed external strain on Cu interconnects is achieved by cantilever buckling in the vise. The strain in the structures is evaluated from the estimated ratio between the curvature at the reference point measured by the laser spot displacement on the position sensitive detector (PSD) and curvature at the place of the device structures. The main distances required for the evaluation of the radius of curvature of the cantilever at the reference point are shown in Figure 77 and can be expressed mathematically as,

$$R = \frac{2 * L_{Spot} * D_{PSD}}{d_{PSD}} \ , \qquad \text{Equation 119}$$

where R represents the radius of curvature, L_{spot} refers to the distance between the point where laser hits the cantilever and base of the cantilever, d_{PSD} is the displacement of the laser spot on the PSD and D_{PSD} is the distance between the PSD and the cantilever in the experimental setup. The average values of imposed external strain along the rr axis, ε_{rr}, at the reference point (local spot) of the Si cantilever is calculated using the expression

$$\varepsilon_{rr} = \frac{t_{Si} + t_{Cu}}{2R} \ , \qquad \text{Equation 120}$$

where t_{Si} and t_{Cu} represent the thickness of the Si cantilever and height of the Cu-interconnect structures (100 nm) which were positioned at the outer side of the cantilever. This is the average strain calculated at the reference point on the cantilever and can be represented as ε_i. The buckling of the Si cantilever as shown in Figure 78 can be compared to a sinusoidal function which is mathematically expressed as

$$y = A\sin x \ . \qquad \text{Equation 121}$$

The Equation 121 is used to calculate the local curvature at the position indicated by L_{spot} in Figure 77 using linear optics set up with the PSD, beam splitter and laser. This local strain expressed as ε_i is used to recalculate the exact imposed strain at the positions where the Cu nanostructures are located on the Si cantilever.

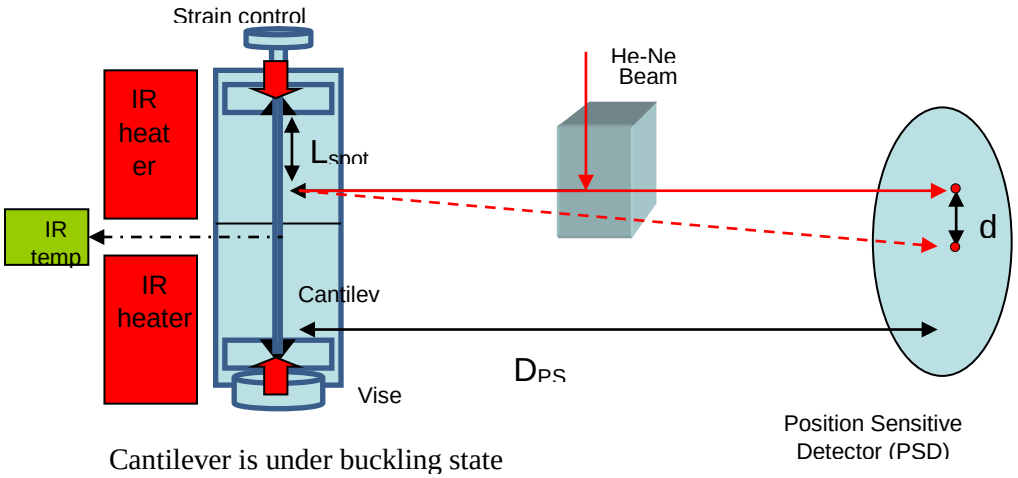

Figure 77. Schematics of the experimental set up for strained annealing with vise allowing precise application of the strain along longitudinal (rr) axis of the cantilever.

The local curvature at any point on the cantilever can be calculated as,

$$k = \frac{\left|y^{''}\right|}{(1+(y^{'})^{2})^{3/2}} \ . \qquad \text{Equation 122}$$

Substituting Equation 121 into Equation 122,

$$k = A\frac{\left|\sin x\right|}{(1+(\cos x)^{2})^{3/2}} \ . \qquad \text{Equation 123}$$

From Equation 123, the local curvature at the Cu nanostructures on the Si cantilever can be accurately calculated if the distance of the nanostructures from the reference spot could be accurately known.

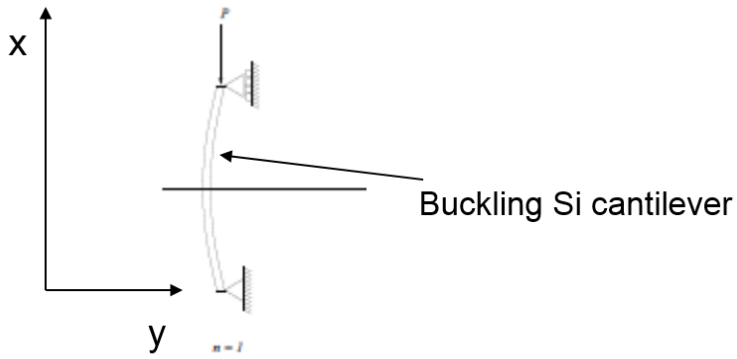

Figure 78. We measure the local curvature at position of the laser spot using linear optics set up with PSD, beam splitter and laser. This result is used to recalculate exact curvature at the positions of the test structures.

With the help of a vernier caliper scale, the distances of the nanostructures are accurately measured as shown in Figure 79. The total length of the cantilever measured is 67mm and is denoted as 'L'. The point where the laser spot hits the Si cantilever is denoted by a red spot and the distance of the laser spot from the base of the cantilever is measured to be 36 mm and is denoted as 'L_i'. The position of the Cu nanostructures on the Si cantilever is denoted by the yellow squares. To simplify the calculations for local curvature, the structures are symbolized by their positions on the cantilever as right (R), middle (M) and left (L) and the distances of these structures from the base of the cantilever are measured as 52mm (L_R), 29mm (L_M) and 5mm (L_L) respectively. As explained before, the strain at the respective Cu nanostructures can be calculated by taking a ratio of the radius of

curvature at the reference point measured by the laser spot displacement and curvature at the place of the nanostructures.

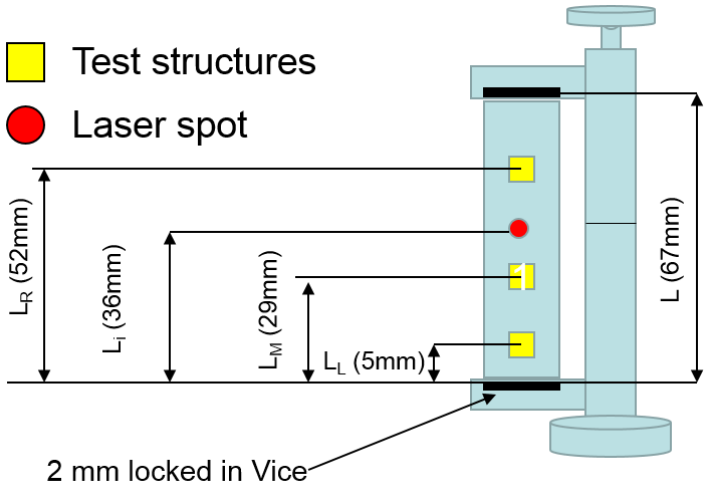

Figure 79. Vise along with the Si cantilever depicting location of the laser spot and the position of the Cu nanostructures on the cantilever

The ratio can be expressed as,

$$k_1 / k_2 = \frac{(\sin x_1)}{(1+(\cos x_1)^2)^{3/2}} \Big/ \frac{(\sin x_2)}{(1+(\cos x_2)^2)^{3/2}} \ , \qquad \text{Equation 124}$$

where x can be related to the distances of the nanostructures from the base of the cantilever as,

$$x = \frac{L_x}{L}\pi \ , \qquad \text{Equation 125}$$

where L_x represents the lengths namely L_i, L_R, L_M, L_L used to denote the distances of the Cu nanostructures from the base of the cantilever. From the experimental measurements, the value of curvature at the laser spot can be calculated by using the Equation 119 and is denoted as k_i. As one of the curvatures is a known factor, from the ratio of the curvature to the other locations, the curvature imposed at the nanostructures is calculated to be

0.0855 (k_L), 0.916 (k_M) and 0.325 (k_R). From the curvature calculations, the strain at these Cu nanostructures is calculated by using Equation 120 and is obtained in terms of the strain at the reference point (ε_i) as 0.088 ε_i (ε_L), 0.94 ε_i (ε_M) and 0.334 ε_i (ε_R). These factors for the local strain and curvature remain unchanged as long as the laser spot distance from the base of the cantilever is maintained uniform during the batch measurements.

5.3.7.3. Strained Annealing Setup

The design of the setup is adopted from the one developed earlier by Stafford et al [68]. All the optical components are mounted on micrometer driven rotational and translational supports allowing short-distance fine adjustments of the laser beam optical path. A 1.5mW JDSU, 632.8nm He-Ne (red) laser is used as the light source. The laser beam is collimated (spot size 1mm) using a beam collimator allowing only part of the beam with maximum intensity in order to improve the signal to noise ratio. The laser beam reflected from the backside of the cantilevers is directed to a position sensitive photo detector, PSD (OSI Optoelectronics). The bending of the Si cantilever with Cu interconnects is tracked by the laser spot displacement along the vertical axis of the PSD. The cantilevers are annealed with two symmetrically positioned IR heaters from the back side whereas the temperature is measured by IR sensor as shown in Figure 80. The use of proportional feedback controller allows precise control of the annealing temperature and the temperature ramping rate [55].

The thermal conductivity of Si is good enough so that the difference in temperature of the front and backside of the cantilevers during annealing is 1 ^oC. All samples are annealed for one hour. The annealing temperatures are 200 ^oC and 250 ^oC

and the strain reported is in-situ during annealing. A typical data recorded for in-situ annealing measurements of the Si cantilever is shown in Figure 81 which represents a plot of temperature vs. displacement of the laser spot on the PSD.

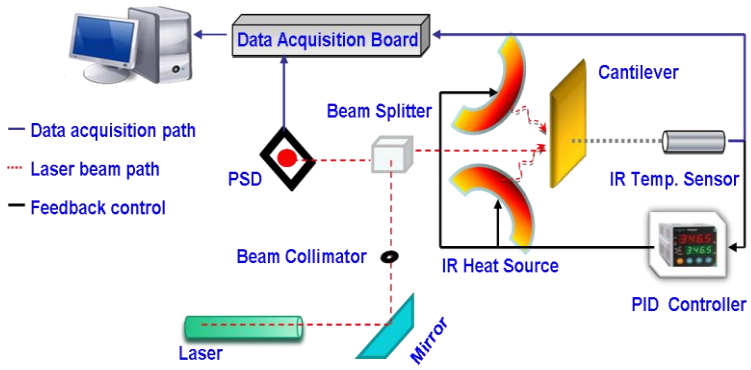

Figure 80. Schematics of the system for in-situ stress measurements during annealing.

The reported strain represents the difference in the strain between relaxed state of the cantilever at room temperature and the strained state of cantilever during annealing. During annealing of the Si cantilevers with the strain controlled layers, the cantilevers are under biaxial state of stress ($\sigma_{rr}=\sigma_{\theta\theta}$) [57, 58, and 61] whereas with the newly machined vise in the setup, the cantilevers are under uniaxial state of stress and the externally imposed strain along rr axis, ε_{rr}, and along θθ axis, $\varepsilon_{\theta\theta}$ ($\varepsilon_{\theta\theta} = - \nu_{Cu} \cdot \varepsilon_{rr}$) can be algebraically summed with the initial strain existing in Cu grains ε_0. The initial strain in θθ direction existing in the Cu interconnects/grains is expected to be tensile due to the grain zipping process during superfilling. However, the way the experiment setup is designed and the geometry of the cantilever bending with respect to the placement of the interconnect nanostructures; the externally imposed strain in θθ direction is always compressive which

effectively reduces the overall strain in this direction during annealing. This effect is expected to promote the densification of the grain boundaries with the surface vector parallel to θθ direction as shown in Figure 76.

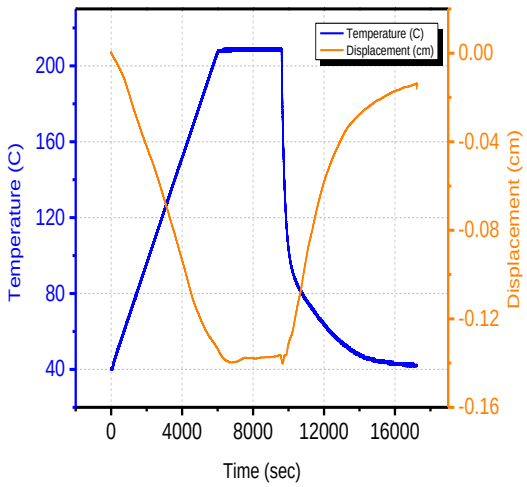

Figure 81. Displacement of the laser spot on the PSD as a function of the temperature and time of annealing of the Si cantilevers.

CHAPTER 6

RESULTS AND DISCUSSION

This chapter discusses the results obtained during the experimental procedures and characterization of the electrodeposited CoFeNi alloys and Cu nanostructures. As discussed in Chapter 1, this dissertation aims at studying the effect of electrodeposition parameters, additives and different substrates on the metallurgical, mechanical and physical properties of electrodeposited CoFeNi thin films. This dissertation further explores a novel concept of strained annealing and its application to improve the conductivity of Cu-interconnect nanostructures widely used in the electronic devices.

6.1. Design parameters and the electrodeposition bath of CoFeNi alloys

The design of an optimum electroplating bath for deposition from stagnant solution involves studying the various chemicals to be included in the plating solution and the effect of chemical concentrations on the composition and magnetic properties of the CoFeNi alloys. Table 4 shows the bath designed by Brankovic et al. [89] which was used as an initial plating solution to deposit CoFeNi alloys. The plating solution can be described as follows: Ammonium chloride (NH_4Cl) and boric acid (H_3BO_3) are used as buffers to regulate the pH of the solution during electrodeposition [4, 89, and 91]. The change in the pH is attributed to the H_2 evolution reaction occurring in parallel at the cathode. Cobalt chloride hexahydrate ($CoCl_2$, $6H_2O$), nickel chloride hexahydrate ($NiCl_2$, $6H_2O$) and ferrous chloride tetrahydrate ($FeCl_2$, $4H_2O$) were used as salts to provide metal ions in the solution. Saccharin is used as an additive to lower the stress during electrodeposition whereas sodium lauryl sulfate and 5-sulfo salicylic acid (SSA) are

added to minimize the surface tension during electrodeposition and to complex the Fe^{3+} ions in the solution.

Table 4. Initial Electroplating Bath Design

Chemical Name	**Concentration (g/L)**
NH_4Cl	20
H_3BO_3	25
$NiCl_2 * 6H_2O$	40
$FeCl_2*4H_2O$	4
$CoCl_2*6H_2O$	30
Saccharin	0.3
Sodium Lauryl Sulfate	0.1
5 - SSA	0.15

6.1.1. Effect of change in buffer

As explained in Chapter 2, the metal reduction reaction is accompanied by H_2 evolution reaction occurring simultaneously at the cathode. Due to the hydrogen gas evolution, there is a local increase in the pH near the electrode/solution interface. This local change in the pH results in hydroxide precipitation on the electrode surface affecting the properties of the electrodeposited CoFeNi alloy. In order to regulate the pH during electrodeposition, researchers have opted ways to add buffer chemicals to the plating solution. Ammonium chloride and boric acid are one of the widely used buffer chemicals in the electroplating industry and hence are included in the initial bath design. However, due to the possible environmental hazards and risks to the human body involved with the use of boric acid, the industry was actively searching for alternate buffer chemicals. With this effort in mind, the existing buffer chemicals are replaced by sodium citrate and citric

acid. These buffer chemicals pose no harm to humans and hence, the effect of these buffers on the properties of electroplated CoFeNi alloys is studied.

6.1.1.1. Potential Transients during Electrodeposition

The effect of change in the buffer chemicals directly affects the kinetics of the electrodeposition as shown in Figure 82.

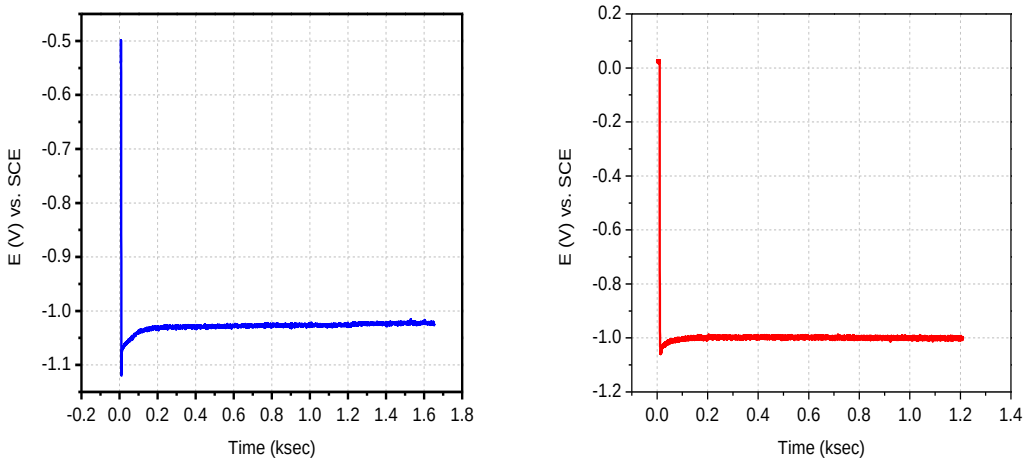

(a) (b)

Figure 82. Potential transient during electrodeposition of CoFeNi alloys from (a) bath containing boric acid and ammonium chloride as buffers (b) bath containing sodium citrate and citric acid as buffers.

With boric acid and ammonium chloride in the plating solution, the overpotential during electrodeposition is more negative as compared to citric acid for the same applied current density. This change is favorable as the rate of hydrogen evolution reaction is lowered as the overpotential becomes more positive during electrodeposition. As the hydrogen evolution rate is suppressed, the pH is maintained constant during electrodeposition and the efficiency of the deposition is increased. Figure 82a shows the potential transient

during a deposition from a boric acid plating solution whereas Figure 82b shows the transient of a deposition from a bath containing citric acid.

6.1.1.2. Magnetic Characterization

After reviewing the kinetics of electrodeposition, the next step involved the magnetic characterization of the deposited thin films.

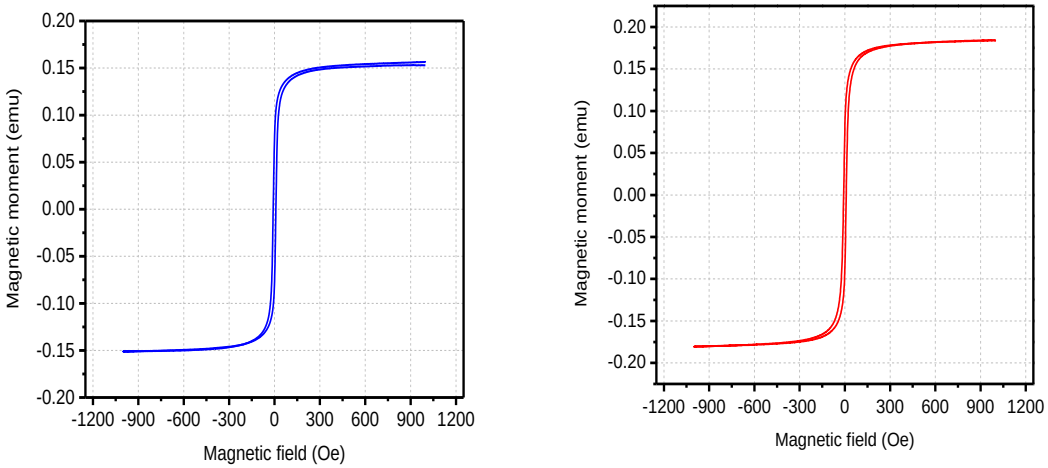

(a) (b)

Figure 83. M-H loop for the electrodeposited CoFeNi film deposited from (a) bath containing boric acid (b) bath containing citric acid

Figure 83a represents the M-H loop for the CoFeNi film electrodeposited from a bath containing boric acid whereas Figure 83b shows a similar M-H loop for the CoFeNi film deposited from a citric buffer plating bath. Both plots show that the magnetic properties of the CoFeNi alloys are retained even after replacing the buffer chemicals in the plating solution. This implies that the inclusion of citric acid in the plating solution does not have any adverse effects on the magnetic properties of the deposited alloy.

6.1.1.3. Electrical Characterization

The electrical characterization of the electrodeposited CoFeNi thin films is performed using the four point probe technique as explained in Chapters 4 and 5.

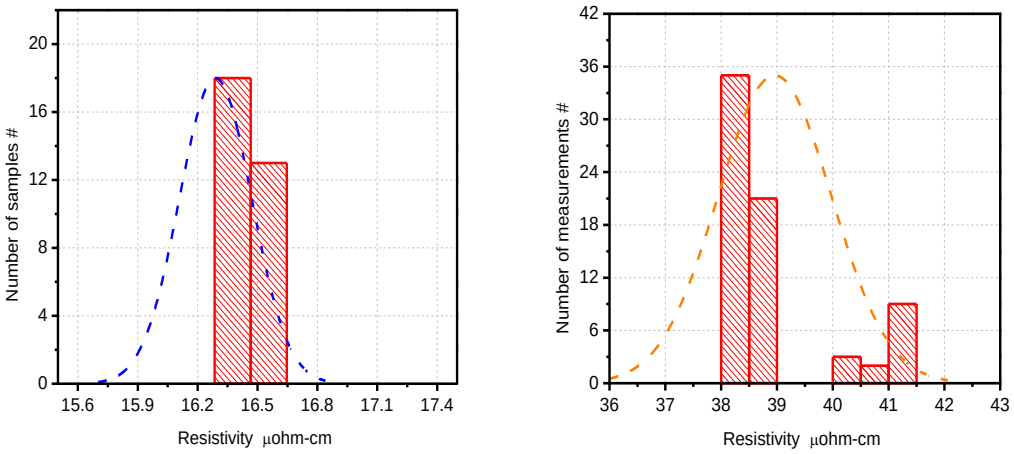

(a) (b)

Figure 84. Histogram depicting the resistivity values over the CoFeNi thin film surface deposited from (a) bath containing boric acid (b) bath containing citric acid.

The CoFeNi films deposited from a bath containing citric acid as buffer have shown higher resistivity than the films deposited from a boric acid bath as shown in Figure 84a and 84b respectively. This effect can be attributed to the insoluble metal complexes formed with the citrates in the plating solution [93, 94]. These complexes are incorporated in the deposit which act as active sites for electron scattering and hence, there is an increase in the resistivity of the CoFeNi film deposited from a solution containing citric acid buffer.

6.1.1.4. Crystallographic Characterization

The crystallographic properties of the electrodeposited films are largely affected by the composition and the overpotential of the deposition. Debye-Scherer's formula is used to calculate the grain size of the peak identified in the XRD data.

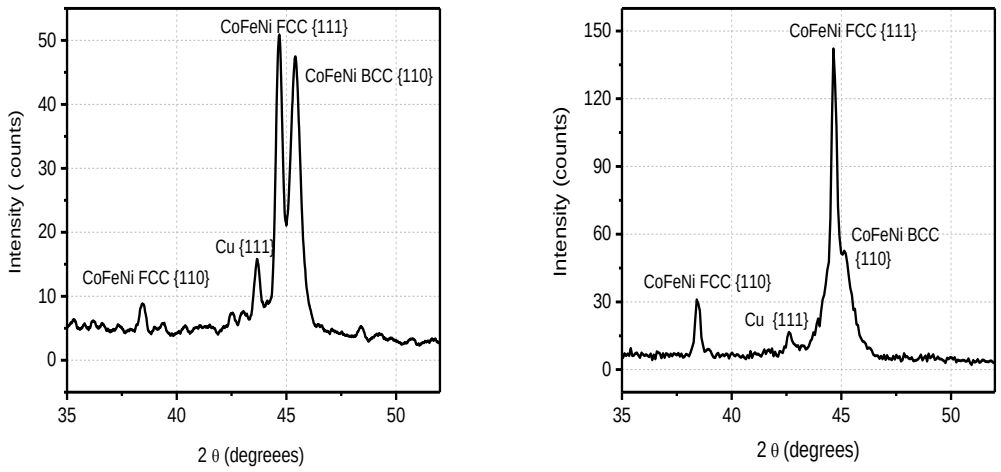

(a) (b)

Figure 85. XRD Data and grain size calculation for the electrodeposited CoFeNi film from (a) bath containing boric acid (b) bath containing citric acid.

Figure 85a shows the crystallographic structure of the CoFeNi film deposited from a solution containing boric acid. Three CoFeNi peaks, namely CoFeNi FCC {110}, CoFeNi FCC {111} and CoFeNi BCC {110} are observed with the BCC and FCC phase equally contributing to the crystal structure. The grain size calculated for these films is roughly 55nm. Figure 85b shows the crystallographic structure of the CoFeNi film deposited from a solution containing citric acid. Three CoFeNi peaks, namely CoFeNi FCC {110}, CoFeNi FCC {111} and CoFeNi BCC {110} are observed with a suppressed

BCC phase in the crystal structure. The grain size calculated for these films is roughly 67nm.

6.1.2. Effect of varying Co concentration

The Co concentration in the initial bath design was 30g/L. An effort was made to increase the Co concentration in two steps, 45g/L and 60 g/L.

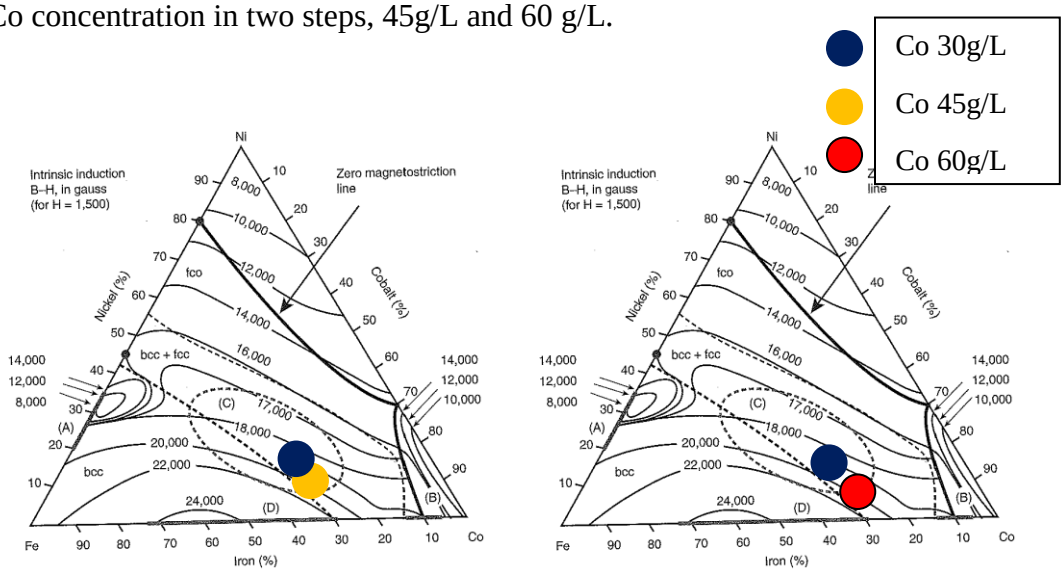

(a) (b)

Figure 86. Ternary plots showing composition of the two films electroplated from (a) bath containing Co 45g/L (b) bath containing Co 60g/L in comparison with the original composition shown by the blue circle.

Following the change in the concentration of Co in the solution, the composition of the deposited CoFeNi film was monitored using the EDS. Results show that the content of Co in the electrodeposited CoFeNi alloy varies directly with the Co concentration in the plating solution. With a higher Co concentration in the solution, there was a significant increase in Co content in the CoFeNi alloy. Figures 86a and 86b show the ternary plots depicting the composition of the deposited film from bath containing varying Co concentration. The blue circle represents the composition of the film deposited from the

initial bath whereas the orange and the red circle represent the composition when the Co concentration is 45g/L and 60g/L respectively.

6.1.3. Effect of varying Fe concentration

The Fe concentration in the initial bath design was 4g/L. An effort was made to increase the Fe concentration in two steps, 25g/L and 30 g/L.

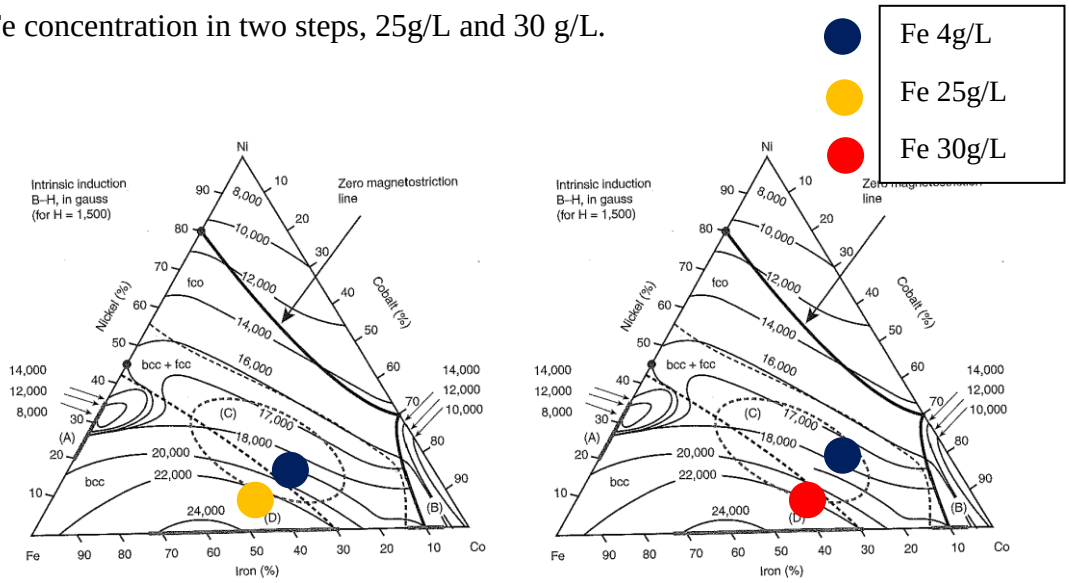

(a) (b)

Figure 87. Ternary plots showing composition of the two films electroplated from (a) bath containing Fe 25g/L (b) bath containing Fe 30g/L in comparison with the original composition shown by the blue circle.

Following the change in the concentration of Fe in the solution, the composition of the deposited CoFeNi film was monitored using the EDS. Results show that the content of Fe in the electrodeposited CoFeNi alloy varies directly with the Fe concentration in the plating solution. The preferential deposition of Fe is at the expense of lowering the Ni deposition rate and thereby increasing the Fe/Ni ratio in the deposit. The intermediate step of iron deposition involves the adsorption of $Fe(OH)^{+}$ which inhibits the active sites for Ni^{2+} reduction on the electrode surface. Hence, with higher increase in the Fe

concentration in the solution, the Ni content from the alloy gets depleted. Figures 87a and 87b show the ternary plots depicting the composition of the deposited film from bath containing varying Fe concentration. The blue circle represents the composition of the film deposited from the initial bath whereas the orange and the red circle represent the composition when the Fe concentration is 25g/L and 30g/L respectively.

6.1.4. Effect of Current Density

In the earlier sections, the effect of chemical concentration on the composition and magnetic properties of the electrodeposited CoFeNi film is discussed. This section explains the effect of current density on the deposition overpotential, the deposition rate and coercivity of the deposited CoFeNi film. The applied current and the overpotential are very crucial parameters while designing a process for the electrodeposition of thin films and hence, these parameters need to be tuned at their optimum value.

6.1.4.1. Overpotential

The electrodeposition is done by the galvanostatic method in which a fixed current is applied for a definite amount of time and the potential is recorded. This potential is recorded between the working electrode (Cu substrate) and the reference electrode (Saturated Calomel Electrode) and it governs the kinetics of the electroreduction reactions. For different values of current density, CoFeNi thin films are deposited and the overpotential is recorded during the experiment. Figure 88 shows a plot of overpotential during deposition as a function of the applied current density. With the increase in the applied current density, the potential has shown to increase and thereby improve the reaction kinetics. However, at higher current densities, the potential recorded is more than -1.2V (vs. SCE). As shown in the Pourbaix diagram in Figure 89, water splitting

reaction is promoted beyond a potential of -1.2 V vs. SCE. This reaction further reduces the efficiency and thereby the deposition rate for the CoFeNi film.

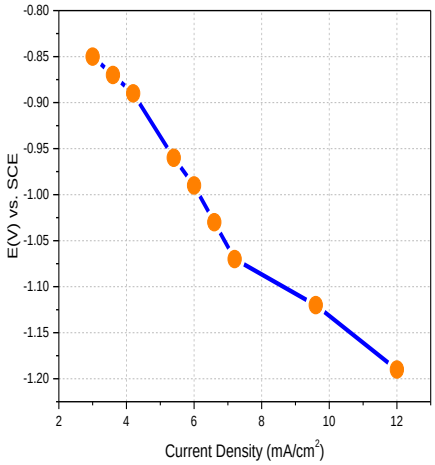

Figure 88. Potential during deposition as a function of the current density.

Hence, the potential needs to be maintained at an optimum value (below -1.2V) to yield the best efficiency and growth rate for the CoFeNi film.

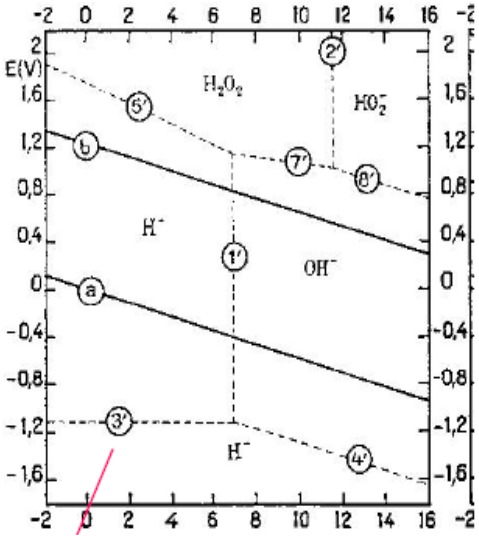

Figure 89. Pourbaix Diagram for water

Considering all the above mentioned factors, a current density of 9.6mA/cm^2 (-1.1 V vs. SCE) is chosen to be the optimum.

6.1.4.2. Deposition Rate

The applied current density directly affects the nucleation rate on the electrode surface and hence, indirectly controls the deposition rate of the film. Hence, to study the effect of current density on the deposition rate, the current density is varied from 5mA/cm^2 to 12mA/cm^2. Figures 90a and 90b show the effect of current density on the deposition rate and the efficiency of the electrodeposition.

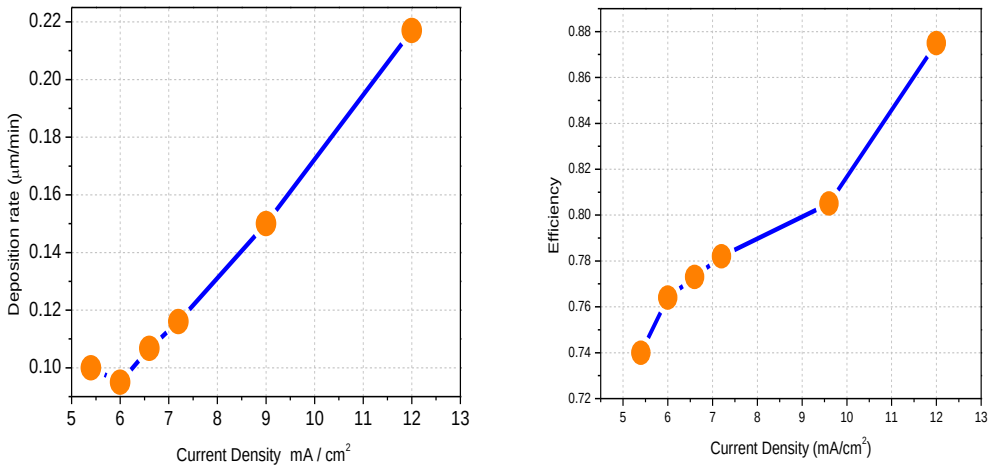

(a) (b)

Figure 90. Effect of current density on (a) Deposition rate (b) Efficiency

The constant increase in the deposition rate can be attributed to the increase in nucleation rate, increase in overpotential and depletion of H^+ ions which minimize portion of current used for hydrogen evolution reaction. This effect in turn improves the efficiency of the electrodeposition.

6.1.4.3. Coercivity of the CoFeNi thin film

One of the important parameters while designing the plating bath for the deposition of CoFeNi alloys is the coercivity. Ideally, a highly soft magnetic material (i.e. low coercivity) is suitable for the magnetic core used in MEMS devices. Researchers have shown the dependence of electroplating parameters on the magnetic properties of the material and hence, the effect of applied current density on the coercivity is studied below. Figure 91 shows the dependence of the coercivity on the applied current density. It is observed that the coercivity of the CoFeNi film decreases with increase in the current density. This effect can be attributed to the increase in nucleation rate at higher current densities. Higher nucleation rate results in larger number of grains and hence, effectively reduces the grain size. Due to smaller grain size, lesser amount of energy is required to align the grains in the direction of the magnetic field which in turn lowers the coercivity of the CoFeNi film.

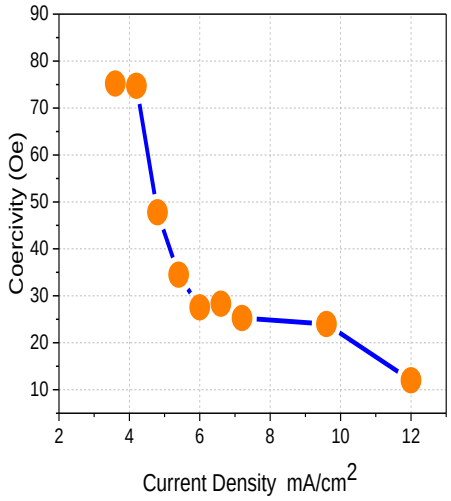

Figure 91. Dependence of coercivity of the CoFeNi film on the applied current density during electrodeposition.

6.1.5. Effect of pH on the composition of the CoFeNi alloy

In order to study the effect of pH and current density on the composition and magnetic properties of the CoFeNi alloy, two sets of data with varying pH and current density are recorded. As explained in Chapter 2, Fe, Co and Ni reduction reactions are pH dependent. Ni and Co have faster deposition rates at pH < 2 whereas Fe reduction reaction is dominant at pH>3. For the first set of data, a pH of 2.5 is maintained and the current density for deposition is varied from 5.4mA/cm^2 to 9.6mA/cm^2 whereas for the second set of data, the pH is maintained at 3.0 and the current density is varied in the same limits. Figure 92a shows the trend in the composition of the CoFeNi films deposited from a solution maintained at pH 2.5 using varying current densities.

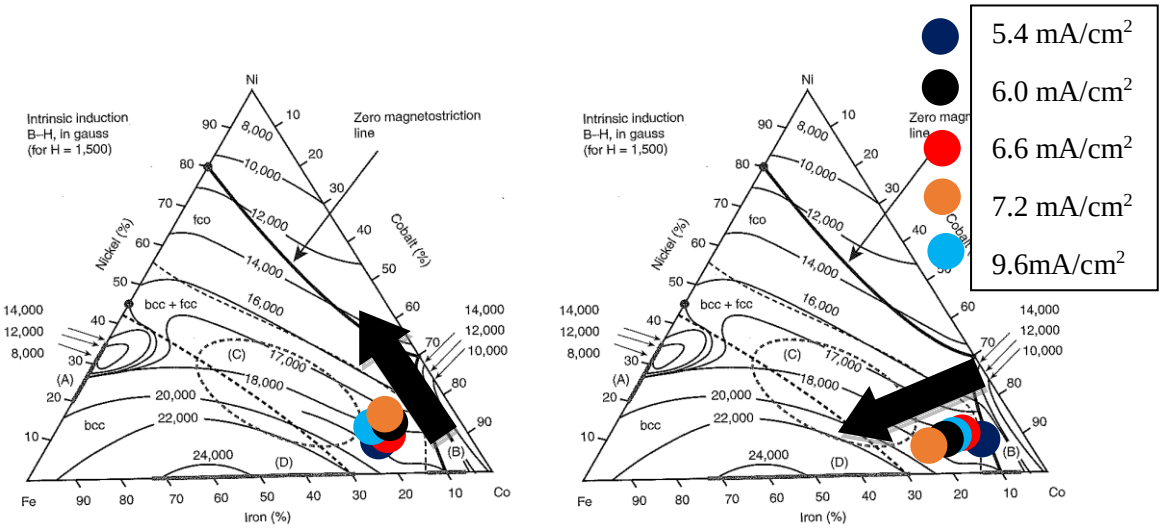

(a) (b)

Figure 92. Effect of pH and current density on the composition and magnetic properties of CoFeNi thin film deposited from a plating solution maintained at (a) pH=2.5 (b) pH=3.0.

At this pH, the Ni and Co reduction rates increase with increase in the current density and a retarded Fe deposition rate is observed. This can be attributed to the slower reaction rate

of the intermediate step during Fe reduction (formation of Fe $(OH)^{+}_{ads}$). In contrast, an opposite effect is seen for the second data set, wherein the Fe deposition rate is fast at higher pH. At this pH, the rate limiting step for formation of $Fe(OH)^{+}$ is faster and hence the reduction rate of Fe is higher than Ni and Co. Fe(OH) adsorbs preferentially on the surface and blocks the sites for Ni adsorption thereby reducing the Ni content in the CoFeNi alloy. With increasing current density, the Fe content continues to increase at the expense of the Ni content in the deposit. From the above results and discussion, two optimum electroplating solutions can be suggested for obtaining the desired composition, magnetic and physical properties of the electrodeposited CoFeNi thin films. These solutions are named as Bath Design III and Bath Design IV and are characterized by the difference in the metal ion concentration, efficiency and the deposition rate. Following Tables 5 and 6 show the two proposed plating bath designs:

Table 5. Optimum electroplating bath design and process parameters (bath III)

Chemical Name	**Concentration (g/L)**
$C_6H_8O_7$	1.45
$C_6H_5O_7Na_3$	21
$NiCl_2$ * $6H_2O$	80
$FeCl_2$*$4H_2O$	30
$CoCl_2$*$6H_2O$	60
Saccharin	2
Sodium Lauryl Sulfate	0.1
5 - SSA	0.15

Parameters	**Value**
pH	3.0
J	8.64mA/cm^2
γ	0.92
R	164 nm/min

The electroplating bath design III is characterized by Ni and Fe concentrations as 80g/L and 30g/L respectively. Additionally, the process parameters pertaining to this bath design include the applied current density, the efficiency of the deposition and the deposition rate. The electroplating bath design IV is characterized by Ni and Fe concentrations as 50g/L and 25g/L respectively and is shown in Table 6. Additionally, the process parameters pertaining to this bath design include the applied current density, the efficiency of the deposition and the deposition rate.

Table 6. Optimum electroplating bath design and process parameters (bath IV)

Chemical Name	**Concentration (g/L)**
$C_6H_8O_7$	1.45
$C_6H_5O_7Na_3$	21
$NiCl_2$ * $6H_2O$	50
$FeCl_2$*$4H_2O$	25
$CoCl_2$*$6H_2O$	60
Saccharin	2
Sodium Lauryl Sulfate	0.1
5 - SSA	0.15

Parameters	**Value**
pH	3.0
J	9.6mA/cm^2
γ	0.898
R	175 nm/min

6.2. Magnetic characterization of electrodeposited CoFeNi alloys

6.2.1. Design of Photolithography Mask

In an effort to accurately calculate the magnetic moment of the electrodeposited CoFeNi films, a sophisticated stepwise procedure is implemented to fabricate the magnetic films. The first step is to design the mask for lithography and prepare the substrate for electrodeposition of CoFeNi thin films. With a well-defined size of the pattern, the

volume of the electrodeposited films is calculated accurately, leading to improved moment calculations. Figure 93 shows the lithography mask used to pattern the substrate. A spherical and square shaped mask pattern is designed to minimize the error due to the shape anisotropy playing role in the moment and coercivity measurements. The size of the square pattern is 3mm ^{x} 3mm and the diameter of the circular pattern is 3mm as well.

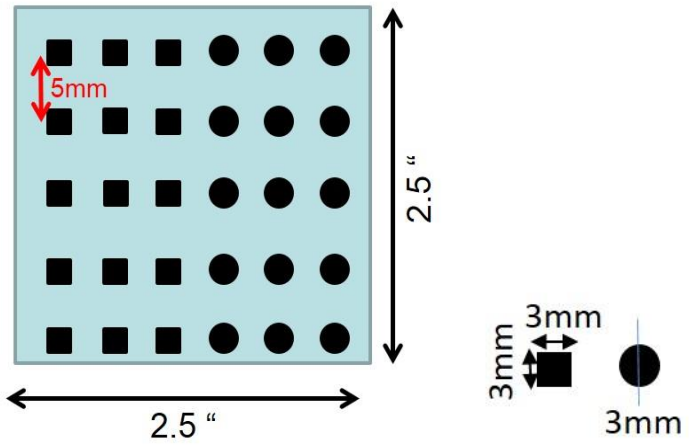

Figure 93. Photolithography mask with spherical and square patterns. Dimensions of the pattern are illustrated.

6.2.2. Calibration Sample Measurements

The second step in the moment measurements is to calibrate the VSM with a reference sample. Generally, a standard NIST Nickel (Ni) sample is used to calibrate the gauss meter. However, for accuracy of the moment measurements, the shape and size of the calibration sample needs to be exactly same as the CoFeNi films to be measured. Hence, a 99.99% pure electrodeposited Ni sample having the same shape and thickness as the electrodeposited CoFeNi thin films is used to calibrate the instrument. Table 7 shows the electroplating bath and the deposition parameters used to plate the Ni calibration sample.

Table 7. Ni electroplating solution and deposition parameters

Chemical Name	Conc. (g/L)
Boric Acid	25
$NiCl_2 * 6H_2O$	110
Saccharin	2
L-Cysteine	0.018

Parameter	Value
pH	3.0
$E_{applied}$	-1.1 V
Thickness	0.75 µm
Temperature	298K

The deposition rate and the efficiency of the Ni plating is calculated by the charge stripping voltammetry.

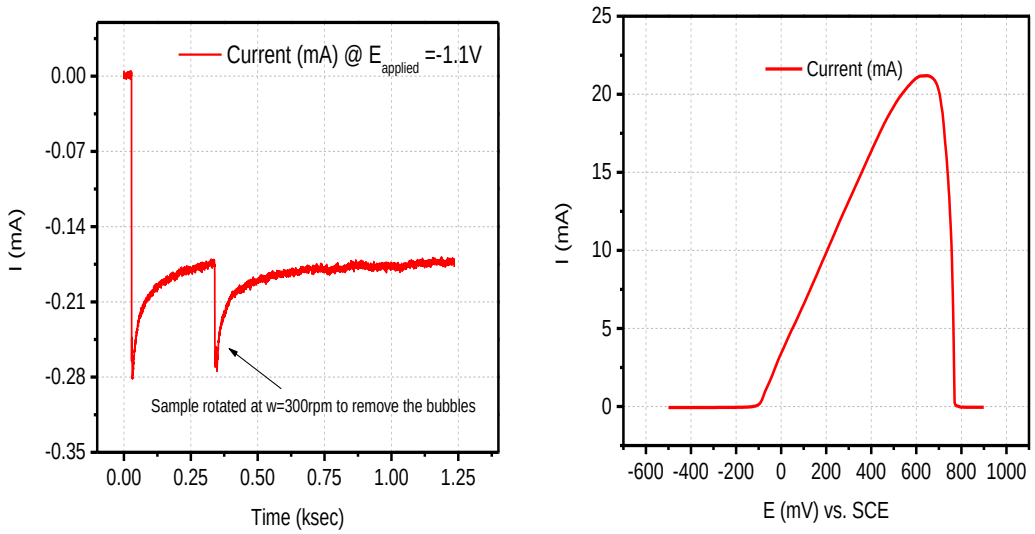

(a) (b)

Figure 94. (a) Current transient during electrodeposition when a constant potential of -1.1V is applied (b) Current transient during the film stripping.

Figure 94a shows the transient recorded during the deposition whereas Figure 94b represents the transient recorded during the film stripping. The efficiency is calculated as

the ratio of charge during stripping to the charge during deposition. From the charge stripping voltammetry results for Ni deposition, the efficiency is 92% and the deposition rate calculated is 550nm/min. Using these values, 0.75 μm thin film is deposited on the spherical and square shaped Cu substrates and the thickness is verified by profilometer and FIB cross section.

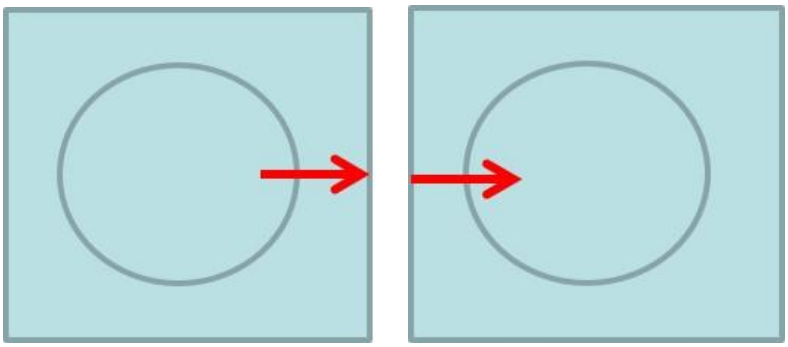

(a) (b)

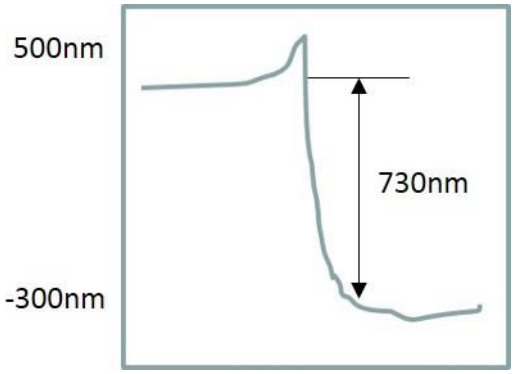

(c)

Figure 95. (a) Left to right scan on the film edge (b) Right to left scan on the film edge (c) A typical scan plot recorded on the profilometer.

Figures 95a and 95b show a typical measurement on the profilometer indicating the thickness of the Ni film. Figure 95c indicates the plot recorded on the profilometer as the

needle scans on the thin film surface. The EAR represents the slight increase in thickness at an edge of the film which is contributed mainly to the edge roughness. The profilometer measurements are indicated in Table 8.

Table 8. Profilometer thickness measurements

# of Iterations	Average Thickness (µm)	Std Deviation (µm)
30	0.804	±0.035

A total of 30 such scans are carried out at different locations on the film surface and the average thickness of the deposited films is calculated.

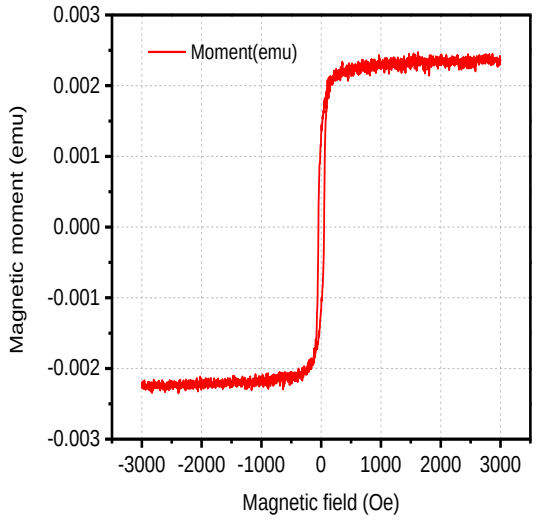

Figure 96. M-H loop for the electrodeposited Ni thin film.

The expected thickness is 0.75 µm and the average measured thickness is 0.804 µm. The plated Ni films are then subjected to magnetic moment measurements using the VSM. The field is swept from 3000 Oe to -3000 Oe at the rate of 1Oe/s and moment is measured as shown in Figure 96. The average saturation moment measured is 2.417emu.

The average thickness of the film verified by the profilometer measurements is 0.804μm and the volume of the sample is calculated equal to $5.68*10^{-6}$ cm^3. The average saturation magnetization (M_s) can be calculated as,

$$M_s = \frac{m_s}{V} \quad . \qquad \text{Equation 126}$$

From the measured parameters, the saturation magnetization (Ms) can be calculated as,

$$M_s = 425.5 \frac{emu}{cm^3} \quad .$$

The standard saturation magnetization of the NIST Ni sample is given to be 475.9 emu/cm^3. Comparing the measured magnetization of the electroplated Ni thin film to the standard NIST sample magnetization, the instrument calibration error is calculated as,

$$\%Calibration\ Error = \frac{425.5 - 475.9}{475.9}$$

and $$\%Calibration\ Error = -10.6\% \quad .$$

The next step is to check the Ni content in the electroplated film and its surface roughness.

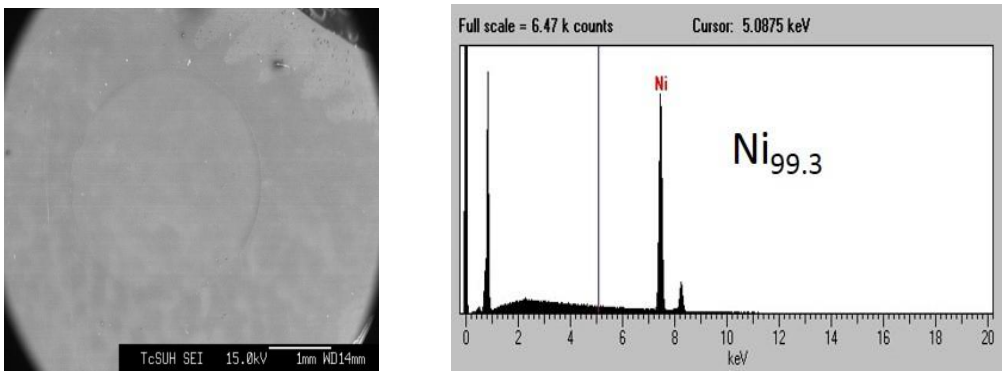

(a) (b)

Figure 97. (a) SEM image of the electroplated Ni and (b) EDS measurements of the Ni confirming 99.9% pure Ni thin films.

Figure 97a and 97b show the SEM image and the EDS measurements of the electroplated Ni thin film surface. These measurements verified that the film deposited was indeed 99.9% pure Ni and has a smooth surface finish.

6.2.3. Magnetic Moment Measurements

The ternary CoFeNi alloys are electrodeposited on patterned Cu substrates using the two electroplating solutions explained in the earlier section. Moment measurements are carried out on three samples electrodeposited using each bath design. An average saturation magnetization per bath design is then calculated to achieve better accuracy in the moment measurements. The thickness, shape and size of the electrodeposited CoFeNi films is maintained similar to the electroplated Ni reference sample.

Initially, the plating solution III is used to deposit the CoFeNi alloys. Three CoFeNi films with thickness 0.7 μm are electrodeposited on a Cu substrate. The thickness of these films is verified by the profilometer measurements and the FIB cross section. Figures 98a, 98b and 98c show the M-H loop measurements for the CoFeNi films plated using bath III. The saturation magnetization is calculated from the M-H loop using Equation 126. The SEM image and the EDS measurements of a CoFeNi thin film deposited from bath III are shown in Figure 99a and 99b respectively. The moment measurements are highly reproducible and are dependent largely on the thickness of the deposited CoFeNi film. The high content of Fe in the alloy composition results in higher saturation magnetization as shown in the ternary plot in Figure 100 [87, 88].

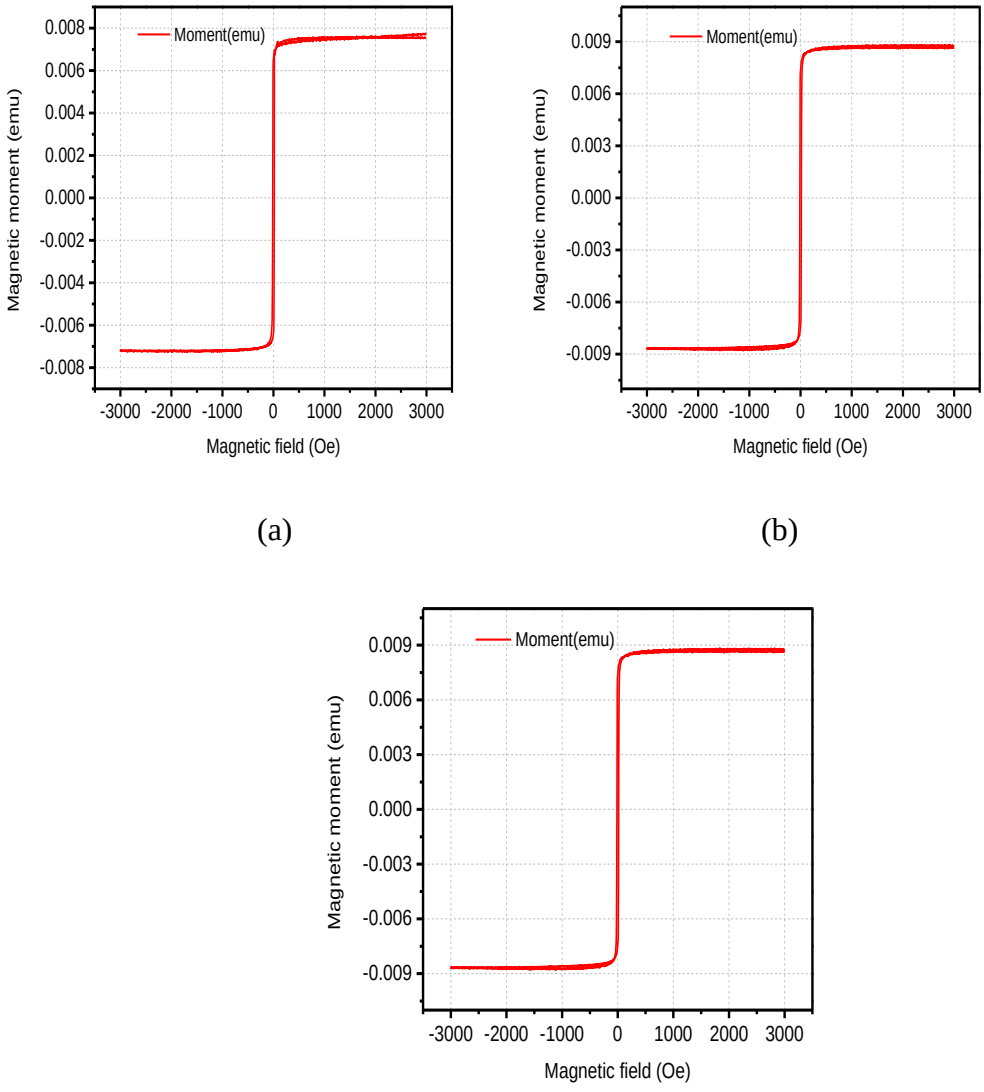

Figure 98. (a), (b) and (c) represent the M-H loops of the CoFeNi samples electrodeposited from bath III plating solution.

The value of the saturation magnetization from the M-H loop closely matches the value expected from the composition as shown in Figure 100. The Coercivity (coercive field) value is extracted from the M-H loop and the results are documented in Table 9.

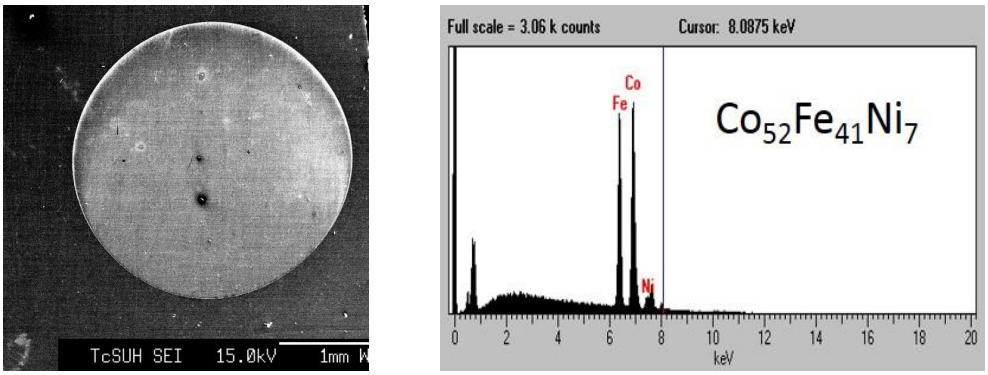

(a) (b)

Figure 99. (a) SEM image (b) EDS measurements on the electrodeposited CoFeNi film surface.

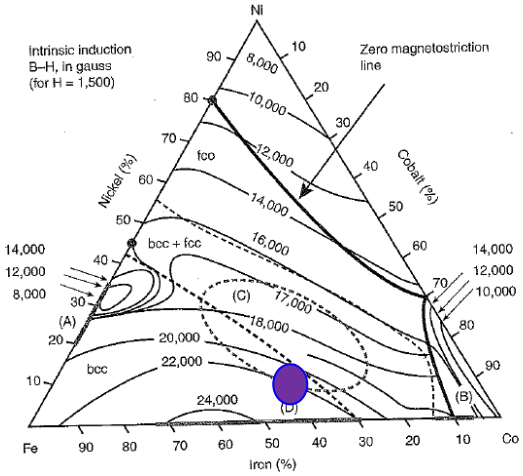

Figure 100. Composition of CoFeNi alloy deposited from plating bath III

Similar experiments are performed to measure the saturation magnetization and coercivity of CoFeNi films deposited using bath IV. Three CoFeNi films with thickness 0.7µm are deposited on a Cu substrate. Figures 101a, 101b and 101c indicate the M-H loop measurements for CoFeNi films plated using bath IV. Figure 102a and 102b show

the SEM image and the EDS measurements of the CoFeNi film deposited using bath IV plating solution.

Table 9. Magnetic characterization of the CoFeNi films electrodeposited from bath III

Property	**Sample1**	**Sample 2**	**Sample 3**
Saturation Magnetization (T)	2.04	2.01	1.98
Saturation Magnetization + 10.6% calibration error (T)	2.24	2.21	2.20
Coercivity (Oe)	13.7	10.85	10.9

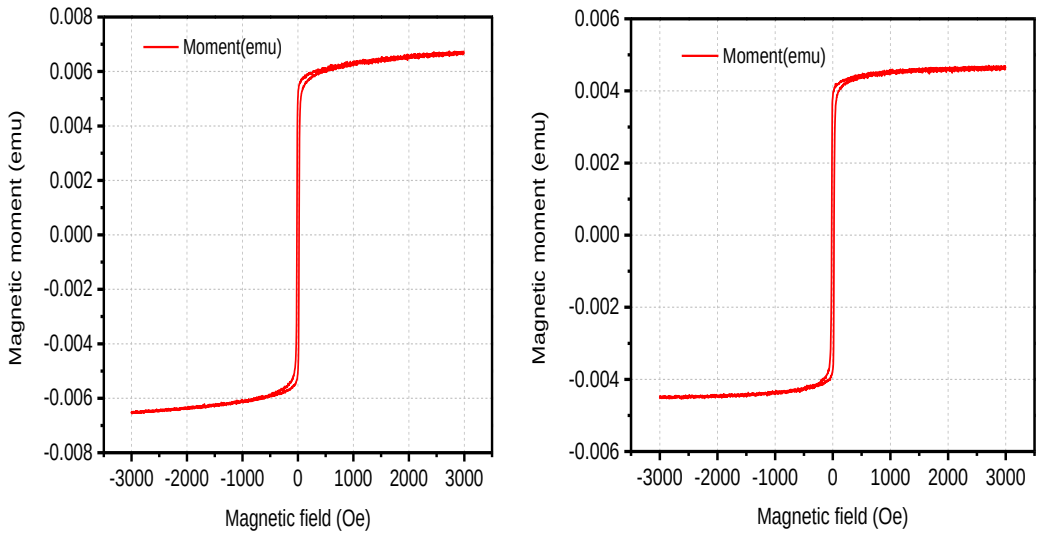

(a) (b)

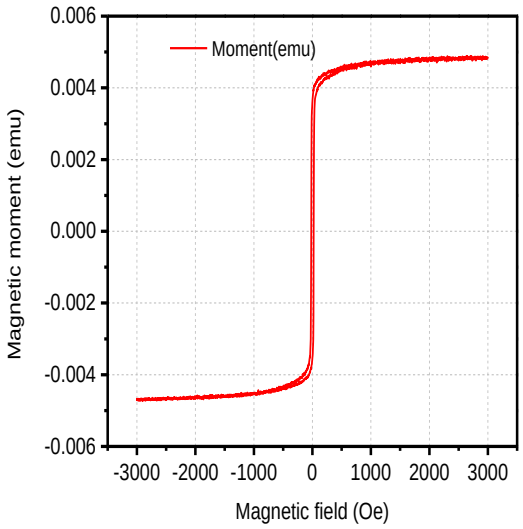

(c)

Figure 101. (a), (b) and (c) represent the M-H loop measurements of the CoFeNi samples electrodeposited from bath IV plating solution.

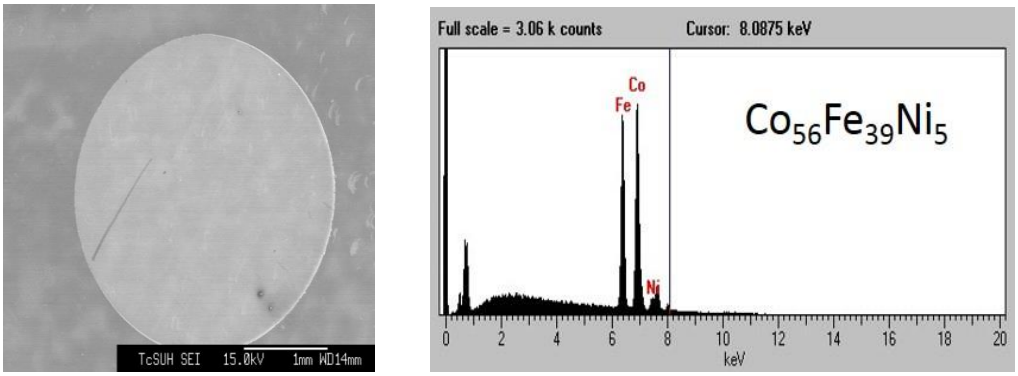

(a) (b)

Figure 102. (a) SEM image (b)EDS measurements on the electrodeposited CoFeNi surface.

The magnetic characterization results including the coercivity and saturation magnetization are listed in Table 10. The results shown in Table 9 and Table 10 clearly indicate that the designed plating solutions yield soft high magnetic moment CoFeNi

alloys. CoFeNi films plated from bath III show higher saturation magnetization and lower coercivity as compared to the films plated from bath IV.

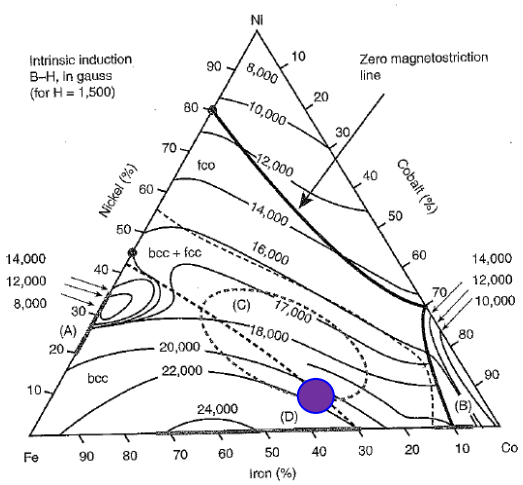

Figure 103. Composition of CoFeNi alloy deposited from plating bath IV.

Table 10. Magnetic characterization of the CoFeNi films electrodeposited from bath IV

Property	**Sample1**	**Sample 2**	**Sample 3**
Saturation Magnetization (T)	1.65	1.62	1.58
Saturation Magnetization + 10.6% calibration error (T)	1.85	1.82	1.77
Coercivity (Oe)	13.82	15.7	17.03

These results can be used while selecting a bath design to deposit CoFeNi alloys for a particular application.

6.3. Effect of saccharin incorporation on the properties of CoFeNi alloys

The ever increasing quality and reliability demand of microsystems indicate that the electrodeposited magnetic alloys used for their fabrication should have minimum possible magnetic losses at the desired frequency range. In order to meet this challenge, the magnetic industry is facing the task of electrodepositing soft high moment magnetic alloys (SHMM) with resistivity greater than 100μΩ-cm. The ternary ferromagnetic CoFeNi alloys represent the class of SHMM alloys which inherently have a higher resistivity than their binary NiFe, CoFe or CoNi counterparts, with similar magnetic properties [4, 5, and 89]. The optimum properties of these electrodeposited alloys are a function of the additive concentration in the electrodeposition solution. Saccharin is one of the most widely used additive and hence, the focus of this section is to discuss the effect of saccharin on the properties of 2.0 – 2.2T CoFeNi alloys.

6.3.1. Saccharin effect on efficiency and deposition rate

Several mechanisms have been proposed to explain the effect of additive incorporation on the rate of metal reduction during electrodeposition of magnetic alloys. However, these mechanisms differ not only from one metal to another but also due to the electrodeposition conditions and additives present. One of the direct methods to observe this effect is by measuring the current efficiency. Empirical observations by research groups have showed that the current efficiency of metal reduction increases in the presence of additives in the electroplating bath. The presence of the additive shifts the potential for parasitic hydrogen evolution reaction cathodically and suppresses the hydrogen evolution [4, 89, and 90]. The charge during deposition is calculated by recording the current transient as shown in Figure 104a. The charge during stripping is

calculated by integrating the area of the current transient and diving by the scan rate, when the potential to the working electrode is swept in the limits of -700 mV to +700mV as shown in Figure 104b. Figure 105a shows the effect of saccharin incorporation on the efficiency of the CoFeNi electrodeposition using plating bath III. Initially, the efficiency increases with increase in saccharin concentration as the hydrogen evolution reaction is inhibited by saccharin adsorption on the electrode surface. However, at larger saccharin concentrations, more amount of saccharin gets adsorbed on the surface reducing the number of nucleation sites for deposition of the CoFeNi alloy [5, 89]. Hence, at higher saccharin concentrations, a drop in the efficiency is observed.

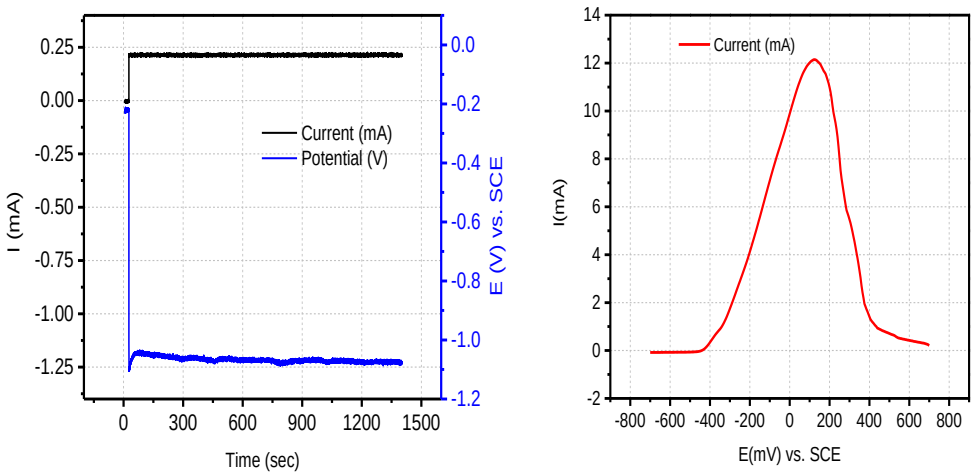

(a) (b)

Figure 104. Influence of saccharin concentration on the (a) Current vs. Potential transient during electrodeposition of CoFeNi film (b) Current vs. Potential transient during stripping of CoFeNi film.

Figure 105b shows the change in the deposition rate as a function of the saccharin concentration in the plating bath III solution. As derived from the efficiency, the deposition rate initially increases with increase in the saccharin concentration, but for

similar reasons mentioned before, the deposition rate of the CoFeNi alloy drops at higher saccharin concentrations.

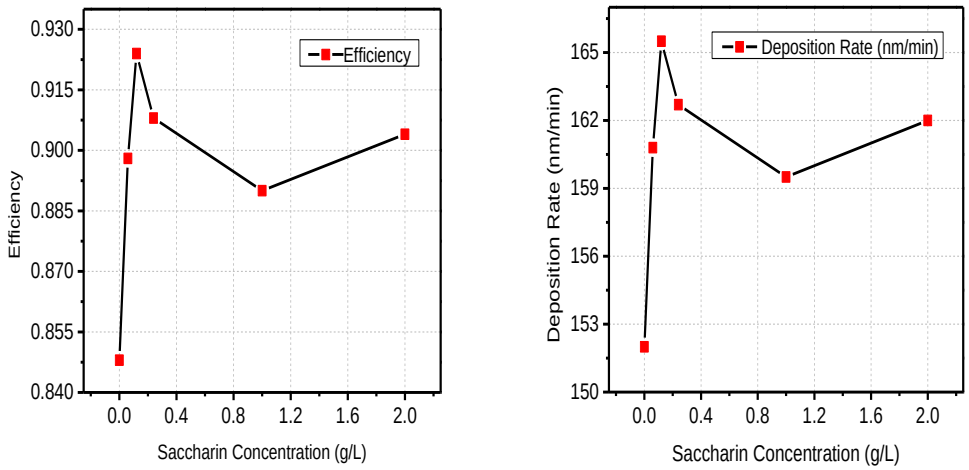

(a) (b)

Figure 105. Influence of saccharin concentration in the bath III plating solution on the (a) Efficiency of the deposition (b) Deposition rate of the CoFeNi alloys.

Figure 106a shows the effect of saccharin incorporation on the efficiency of the CoFeNi electrodeposition using plating bath IV. The efficiency increases with increase in saccharin concentration as the hydrogen evolution reaction is inhibited by saccharin in the solution. However, at larger saccharin concentrations, more amount of saccharin gets adsorbed on the surface reducing the nucleation sites for deposition of the CoFeNi alloy [5, 89]. Hence, at higher saccharin concentrations (2g/L), a drop in the efficiency is observed. A trend similarly to the efficiency is observed for the deposition rate when the CoFeNi films are plated using bath IV. Figure 106b shows the trend in deposition rate as a function of saccharin concentration in plating solution IV.

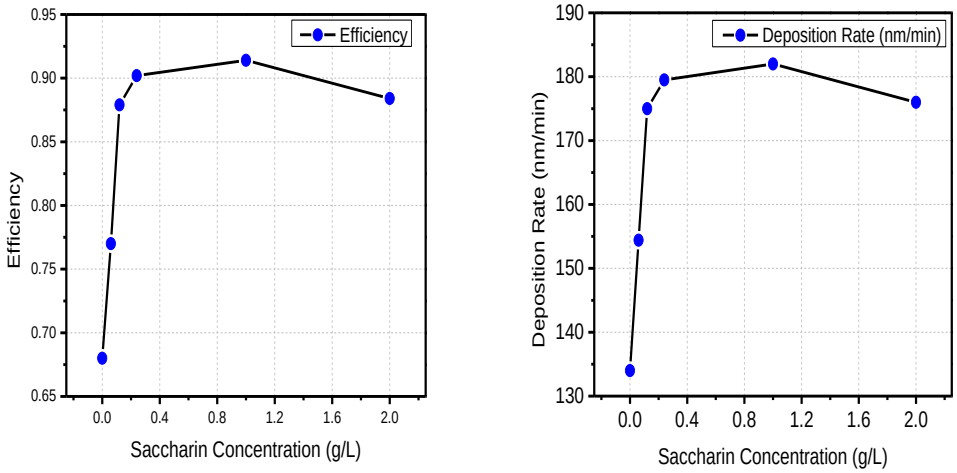

(a) (b)

Figure 106. Influence of saccharin concentration in the bath IV solution on (a) Efficiency of the electrodeposition (b) Deposition rate of the CoFeNi alloys.

6.3.2. Saccharin effect on coercivity of electrodeposited CoFeNi alloys

In order to investigate the magnetic properties of the electrodeposited CoFeNi alloys, the films deposited using plating solution III are subjected to VSM measurements. Results presented in Figure 107a show the dependence of coercivity (H_c) on the content of saccharin in the electroplating solution. This dependence is in agreement with the one reported by George et al. for CoFe alloys electrodeposited from a saccharin based solution [26]. The initial decrease in the coercivity is attributed to the reduction in stress levels during the electrodeposition of CoFeNi with small additions of saccharin in the electroplating solution. The reduced stress levels result in smaller contribution of magnetoelastic energy to the total anisotropy energy thereby leading to electrodepositing lower coercivity CoFeNi films [4, 26, and 89]. However, with increasing saccharin

concentration beyond a particular threshold, the coercivity of the CoFeNi films increases. This cannot be related to the stress in effect on magnetic anisotropy energy change.

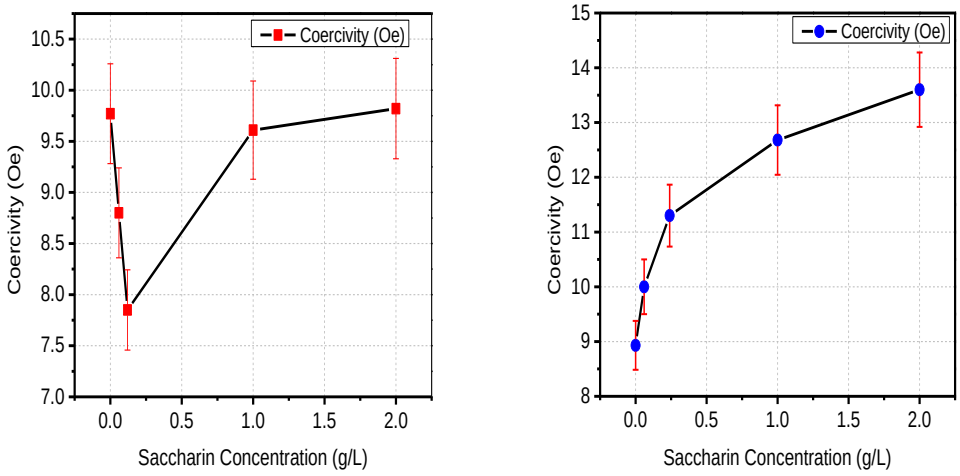

(a) (b)

Figure 107. Influence of saccharin concentration on the coercivity (softness) of the electrodeposited CoFeNi alloy deposited using (a) bath III (b) bath IV.

A correct explanation for this effect could be the additive incorporation mechanism during electrodeposition of the magnetic alloy. The magnetic decoupling of the grains due to the additive related precipitation at the grain boundaries is an antagonistic effect on coercivity of the CoFeNi films [89, 90]. The two opposite effects of saccharin on the coercivity of CoFeNi films result in observed dependence of coercivity on the saccharin concentration producing the CoFeNi films with the lowest coercivity values. Similar measurements are done for CoFeNi films deposited using bath IV plating solution. The trend for coercivity of the CoFeNi films as a function of saccharin concentration in the bath IV solution is shown in Figure 107b. The increase in the coercivity with increase in the saccharin concentration can be attributed to the non-magnetic phase such as CoS, FeS

and NiS in the alloy due to saccharin reduction in the deposit. The magnetic decoupling of the grains due to the additive precipitation results in higher coercivity values of the CoFeNi films deposited using bath IV.

6.3.3. Saccharin effect on the crystal structure and grain size

It is well known that the grain size of the electrodeposited film is strongly influenced by the presence of additive in the electroplating bath and the ability of grain refining of the electrodeposited films by different additives has been previously reported by several researchers. Numerous mechanisms have been suggested regarding the influence of additives on the grain size of electrodeposited films. In brief, the role of an additive as a grain refiner is its effect to (i) block the surface by formation of complex compounds which increase the frequency of nucleation and decrease the surface diffusion of Co, Fe and Ni ions retarding the crystalline growth (ii) hydrogen evolution and/or adsorption and (iii) change in the cathodic overpotential [4, 5, 89, 91]. The evolution of the grain size of the electrodeposited CoFeNi films versus the saccharin concentration in the electroplating solution III has been depicted in Figure 108a, while the Figure 108b shows the XRD data to represent the crystal structure of the electrodeposited films. The crystal structure shown in Figure 108b showed no new peaks attributing to the impurities adsorbed due to the addition of saccharin in the electroplating solution. The grain size is calculated from the XRD data by the Debby- Scherer formula given as [83],

$$d = \frac{0.9 \cdot \lambda}{B \cos\theta} \quad . \qquad \text{Equation 127}$$

Here, *0.9* is the instrumentation factor, λ is the wavelength of the X-ray source, B is the full width half maximum and θ is the Bragg's angle.

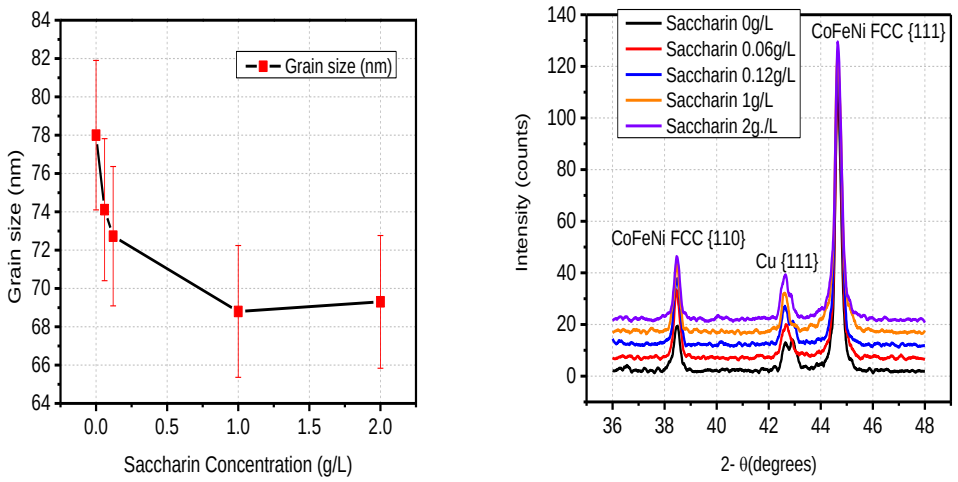

(a) (b)

Figure 108. Influence of saccharin concentration on (a) Grain size (b) Crystal structure the electrodeposited CoFeNi alloy (bath III).

The results show that a small amount of saccharin has a considerable effect on the grain refining of the CoFeNi film deposit. The maximum grain refining has occurred at 1g/L saccharin, after which there is no significant change in the grain size with addition of more saccharin in the plating solution. A similar set of experiments are performed to study the trend in the grain size and crystal structure of the CoFeNi films electrodeposited from plating solution IV. Figure 109a shows the trend in the grain size as a function of the saccharin concentration in the solution. The grain size is calculated using Equation 127 and it is observed that the grain size of the CoFeNi film increases with increase in the saccharin concentration. This effect can be attributed to the adsorption of saccharin molecule on the grain boundaries and promoting the grain growth. However, Figure 109b shows no new peak corresponding to any other crystal phase indicating that the saccharin incorporation in the deposit does not affect its crystal structure.

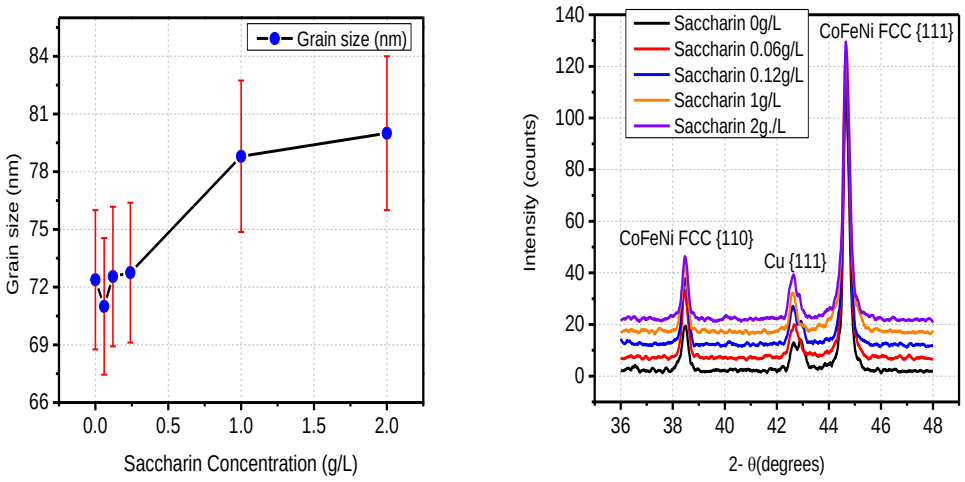

(a) (b)

Figure 109. Influence of saccharin concentration on (a) Grain size (b) Crystal structure the electrodeposited CoFeNi alloy (bath IV).

6.3.4. Saccharin effect on stress in electrodeposited CoFeNi films

There are various reports in literature about the effect of additive concentration in the solution on the growth stress in electrodeposited SHMM films. Most of the data are obtained for saccharin as an additive using ex-situ wafer curvature measurements. The observed stress sign is usually positive (tensile) with a decreasing trend for increasing concentration of saccharin in the plating solution. Figure 110a represents the average stress at 3μm as a function of the saccharin concentration in the plating solution IV. The average stress acting on the cross section of the CoFeNi film (σ_{avg}) during the growth of the film is tensile, except for the very initial region (t_f <0.03μm). In this region, the compressive stress is observed due to the nucleation of CoFeNi islands on the Au seed.

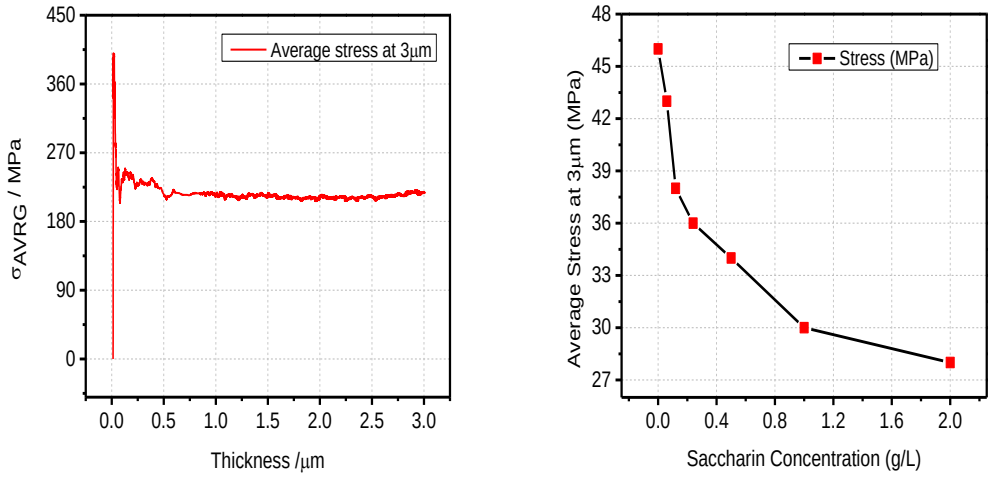

(a) (b)

Figure 110. (a) Stress vs. thickness curve showing the stress evolved as the film growth progresses (b) Stress evolution during deposition of CoFeNi alloys from plating solution IV as a function of saccharin concentration in the solution. Figure represents average stress at 3µm.

The CoFeNi film electrodeposited from saccharin-free solution showed the largest growth stress which was in agreement with the role played by an additive in the electroplating solution. For all the CoFeNi films, the shape of the stress- thickness curves was very similar, the main difference being the value of the maximum tensile stress. The data presented in Figure 111 is the maximum average stress (tensile stress) plotted as a function of the saccharin concentration in the solution IV. For low surface mobility metals like Co and Fe, the maximum tensile stress is mainly during the grain zipping process resulting in the grain boundary formation. Saccharin adsorbs on the electrode surface during electrodeposition and modifies the thermodynamics of the nucleation process, grain structure and the grain boundary formation [5, 36]. It incorporates in the magnetic film in the form of a low surface energy phase such as sulfur related additives, molecular fragments or intermetallic compounds. Saccharin segregates at the grain

boundaries affecting the specific energy and acting as stress reliever during the grain zipping process. During electrodeposition, small amounts of hydrogen gets incorporated in the deposit which is a known cause for post deposition tensile stress (aging stress). Additive adsorption suppresses the hydrogen incorporation in the deposit, thus reducing the levels of tensile stress during deposition and aging. The CoFeNi surface with adsorbed saccharin molecules is likely to have surface bonds saturated by adsorption process reducing the CoFeNi surface energy [4, 5]. However, the grain boundaries formed during the zipping process of CoFeNi surfaces covered with saccharin have a higher grain boundary energy as compared to the grain boundary formed during the zipping process of clean CoFeNi surface. Therefore, we conclude that the impact of saccharin on stress reduction is thermodynamic in nature and we expect a decrease in the deposition stress with increase in the saccharin concentration in the plating solution IV. Brankovic et al derived the model for the maximum average stress as a function of the saccharin coverage, the grain size and the driving force for the grain boundary zipping process given as [5],

$$\sigma_{avg}^{\max}(\theta) = \sigma_{avg,CoFe}^{\max} - 8\frac{\Delta\gamma^{*}}{d_G}\cdot\frac{B\cdot C_{Sac}}{(1+B\cdot C_{Sac})} \quad . \qquad \text{Equation 128}$$

Here, $\Delta\gamma^{*}$ is the difference in the driving force for zipping of CoFe grains with saccharin free surface and CoFeNi grains with maximum coverage of adsorbed saccharin phase (θ=1), d_G is the grain size, $B\cdot C_{Sac}/(1+B\cdot C_{Sac})$ is the saccharin coverage given by Langmuir adsorption isotherm [5, 36].

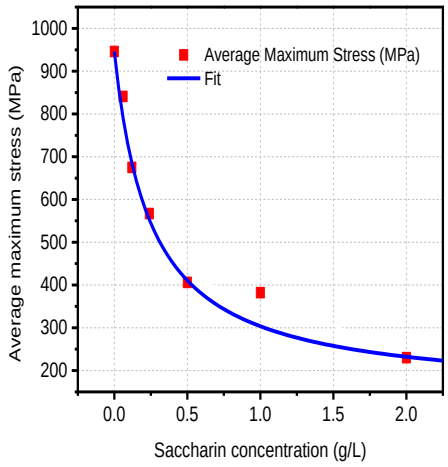

Figure 111. Stress evolution during deposition of CoFeNi alloys (bath III) as a function of saccharin concentration in the solution. Figure represents average maximum stress. The blue line indicates the fit and the fit parameters are listed below in Table 11.

The data for the maximum average stress is fitted using the equation 128 and the fitting parameters are listed in Table 11.

Table 11. Extracted parameters from the fit (bath III)

Parameter	**Value**	**± Std Error**
$\sigma^{max}_{avg,CoFeNi}$	945.9 MPa	44.93
$8\Delta\gamma/d_G$	803.3 J/m^3	64.33
B	4.03 L/g	1.24

A similar set of experiments are performed to measure the in-situ stress during the deposition of CoFeNi films using plating solution III. Due to undesirable results like delamination and film cracking being observed at higher film thicknesses, the CoFeNi film thickness is limited to 1 μm and the average stress is recorded. Figure 112a shows

the average stress measured during CoFeNi film deposition using plating bath III at 1 μm film thickness whereas Figure 112b displays a trend in the average stress as a function of saccharin concentration in the plating solution III.

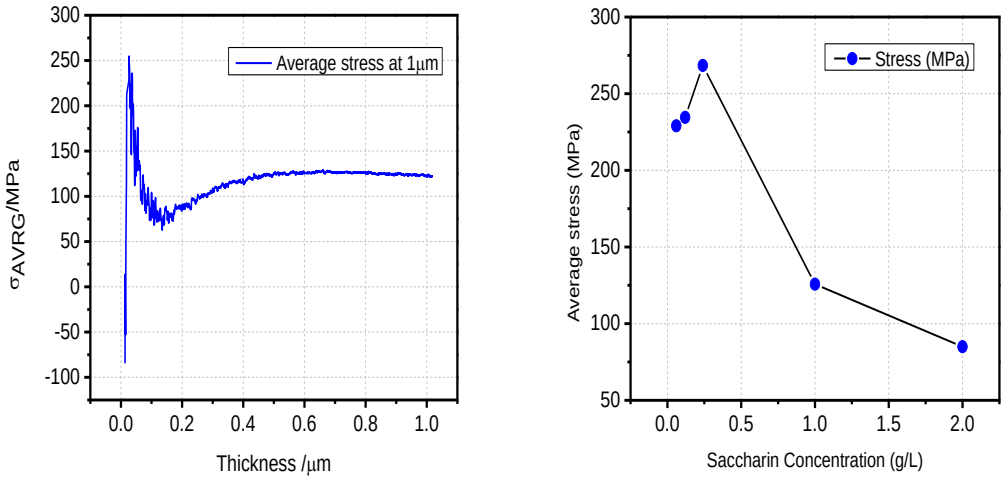

(a) (b)

Figure 112. (a) Stress vs. thickness curve showing the stress evolved as the film growth progresses (b) Stress evolution during deposition of CoFeNi alloys from plating solution III as a function of saccharin concentration in the solution. Figure represents average stress at 3μm.

The data is in agreement with the theory explained in chapter 3 supporting the role played by an additive to minimize the stress during thin film growth. Figure 113 shows the trend in average maximum stress as a function of the saccharin concentration in the plating solution III. With an increase in the saccharin concentration in the plating solution, the hydrogen evolution is suppressed thereby minimizing the maximum tensile stress during island coalescence process. Hence, a decrease in the average maximum stress is observed with an increase in saccharin concentration in the plating solution. As explained above, equation 128 is used to fit the data plotted in Figure 113 and the fit parameters are listed in Table 12.

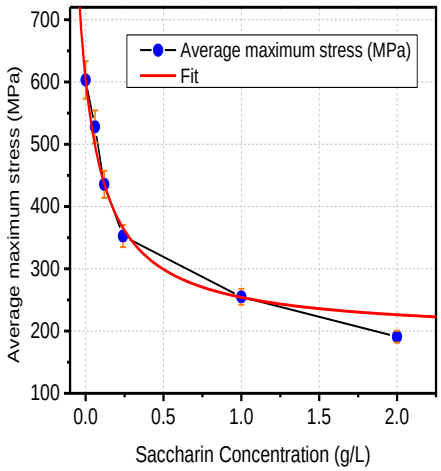

Figure 113. Stress evolution during deposition of CoFeNi alloys (bath IV) as a function of saccharin concentration in the solution. Figure represents average maximum stress. The blue line indicates the fit and the fit parameters are listed below in Table 12.

Table 12. Extracted parameters from the fit (bath IV)

Parameter	**Value**	**± Std Error**
$\sigma^{max}_{avg,CoFeNi}$	603.22 MPa	26.51
$8\Delta\gamma/d_G$	409.82 J/m^3	40.33
B	5.75 L/g	1.34

6.3.5. Saccharin effect on resistivity of electrodeposited CoFeNi alloys

The resistivity of the electrodeposited CoFeNi films is analyzed as a function of the saccharin concentration in the plating solution. The resistivity is measured using the four point probe method and the thickness of the deposit was measured using the charge stripping voltammetry and later verified using the FIB. Figures 114a and 114b show the FIB cross section of the electrodeposited film using plating solutions III and IV. The thickness measured was verified to be 4.95μm and 4.91 μm respectively. Several FIB

cross sections were done per sample and an average film thickness was noted. Figure 115a shows the effect of saccharin concentration on the electrical properties of the electrodeposited CoFeNi thin films deposited using plating solution III. The initial decrease in the resistivity is due to less Fe_x $(OH)_y$ incorporated because of the suppression of hydrogen evolution with addition of small amounts of saccharin.

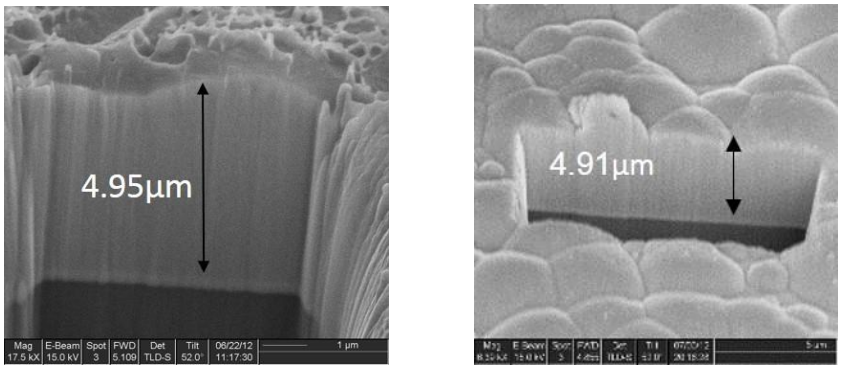

(a) (b)

Figure 114. FIB cross sections of CoFeNi thin films plated (a) From bath III plating solution, the measured thickness is 4.95µm. (b) From bath IV plating solution, the measured thickness is 4.91µm.

An increase in the sulfur content in the deposit shows to increase the resistivity of the CoFeNi film by sacrificing its magnetic properties (reduction in the magnetization and increase in the coercivity). This effect can be attributed to two factors: one, an increase in the impurity concentration due to sulfur incorporation at the grain boundaries, second, the saccharin adsorption reduces the grain size leading to increase in electron scattering at the grain boundaries [5, 36, 91]. The grain boundaries formed by coalescence of the grains/surfaces covered with adsorbed saccharin phase are likely to have more defects; less atom-atom coordination and lower atom packing density contributing to the increase

in conduction electron scattering [92]. Similar resistivity measurements are carried out on the CoFeNi films electrodeposited from plating solution IV with varying saccharin concentration.

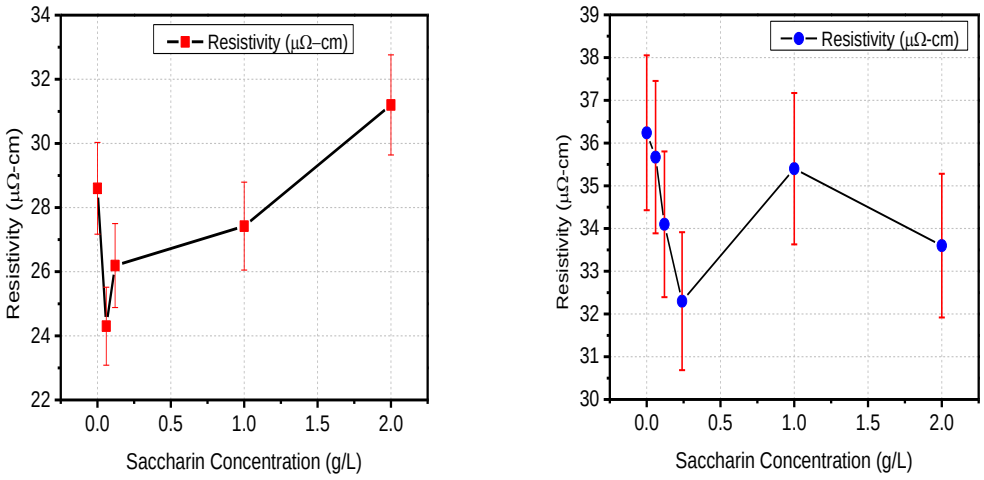

(a) (b)

Figure 115. Influence of saccharin concentration on the resistivity of the electrodeposited CoFeNi alloy (a) using plating bath III (b) using plating bath IV.

The trend in the resistivity as a function of saccharin concentration is shown in Figure 115b. Results show that the resistivity of the CoFeNi films initially decreases with increase in the saccharin concentration. This effect can be attributed to the increase in grain size with the addition of saccharin in the solution. However, at higher saccharin concentrations, larger amount of the additive gets incorporated at the grain boundaries resulting in scattering sites for the electrons. Hence, an increase in the resistivity of the CoFeNi films is observed when deposited from solutions containing higher saccharin concentrations.

6.4. Electrical characterization of electrodeposited CoFeNi alloys

As explained in Chapter 4, the resistivity of the electrodeposited magnetic alloys plays a crucial role in minimizing the eddy current losses at high frequencies. A plating solution has been designed to deposit CoFeNi thin films having a high resistivity. The electrical properties of the electrodeposited CoFeNi alloys are studied using a four point probe measurement technique. The four point probe resistivity measurements are highly influenced by parameters such as the thin film thickness, the material used as seed layer and the seed layer thickness. Hence, a model is designed to predict the actual resistivity of the CoFeNi alloy as a function of the above mentioned parameters.

6.4.1. Electrical Resistivity Model

Thin CoFeNi films are electrodeposited on a conductive seed layer namely copper (Cu), gold (Au) and Permalloy (NiFe) to study the effect of seed layer on the resistivity of the CoFeNi thin films.

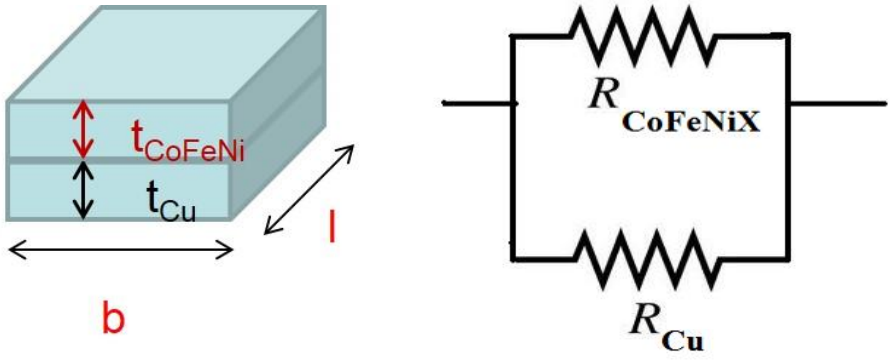

(a) (b)

Figure 116. (a) The CoFeNi thin film and the Cu seed layer can be considered as two independent conducting layers (b) Model showing the two layer acting as parallel resistors.

The electrodeposited thin film and the conductive seed layer act as two parallel resistors as shown in Figure 116a and 116b, implying that the conductive seed layer also contributes to the resistivity measurements while using the four point probe method. The effective resistance of the parallel combination can be calculated as,

$$R_{Tsh} = R_{CoFeNiX} \parallel R_{Cu}\,. \qquad \text{Equation 129}$$

Now, the sheet resistance of a material can be calculated in terms of the physical properties of the material as [66],

$$R_{Tsh} = \frac{\rho_{Tsh} * l}{t_{Tsh} * b} \qquad R_{CoFeNi} = \frac{\rho_{CoFeNi} * l}{t_{CoFeNi} * b} \qquad R_{Cu} = \frac{\rho_{Cu} * l}{t_{Cu} * b}\ , \qquad \text{Equation 130}$$

where R_{Tsh} is the total sheet resistance measured by the four point probe technique, $R_{CoFeNiX}$ is the sheet resistance of the CoFeNi thin film, R_{Cu} is the sheet resistance of the seed Cu layer, ρ_{Tsh} is the total effective resistivity of the parallel combination, $\rho_{CoFeNiX}$ is the resistivity of the CoFeNi thin film and ρ_{Cu} is the resistivity of the seed Cu layer. Parameters l and b represent the physical dimensions of the CoFeNi film device. Substituting Equation 130 in Equation 129, the derived equation can be written as,

$$\frac{\rho_{Tsh} * l}{t_{Tsh} * b} = \frac{\rho_{CoFeNi} * l}{t_{CoFeNi} * b} \parallel \frac{\rho_{Cu} * l}{t_{Cu} * b}\ . \qquad \text{Equation 131}$$

Above Equation 131 can be simplified by canceling out the length and width parameters and the resulting equation can be written in the terms of the resistivity and the film thicknesses as,

$$\rho_{Tsh} = \rho_{CoFeNi} * \left(\frac{t_{Cu} + t_{CoFeNi}}{\frac{t_{Cu} * \rho_{CoFeNi}}{\rho_{Cu}} + t_{CoFeNi}} \right)\ . \qquad \text{Equation 132}$$

Equation 132 indicates that the total resistivity measured by the four point probe method is a function of the individual resistivity of the CoFeNi thin film and the seed layer as well as the thickness of the CoFeNi film and the seed. It can be concluded that a seed with higher resistivity will yield higher value of the total resistivity and to check the same, CoFeNi films are electrodeposited on three substrates namely copper (Cu), gold (Au) and Permalloy (NiFe). Figure 117 shows the total resistivity measured on the CoFeNi thin films with thickness varying from 1μm to 5μm on Cu, Au and NiFe seed layers. The data obtained is in agreement with the model proposed in Equation 132 where the seed resistivity directly affects the total resistivity measured by the four point probe method.

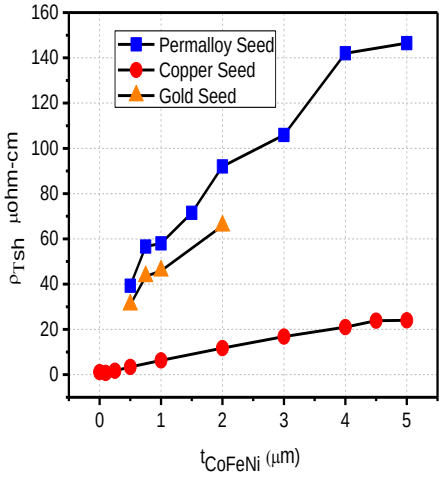

Figure 117. Effect of seed layer on the total resistivity of the electrodeposited CoFeNi thin films. Each point is an average of 50 measurements done on the film surface.

This can be attributed to higher scattering of electrons from a resistive seed layer as compared to a lesser scattering from a conductive seed layer [66, 92]. Similarly, the actual resistivity of CoFeNi thin film can be extracted by fitting each of the curves shown

in Figure 117 by the Equation 132. Figure 118a shows the data for NiFe seed fitted with Equation 132, which yields actual resistivity of CoFeNi thin film equal to 261±30μΩ-cm. Similarly, Figure 118b shows the data for Cu seed, which yields actual resistivity of CoFeNi thin film equal to 131±38μΩ-cm. The value of ρ_{CoFeNi} of the thin films extracted from the fit shows that there is a significant difference in the value of CoFeNi film resistivity when deposited on different seed layers. This difference can be attributed to the scattering at the film/seed layer interfaces which the model fails to take into account.

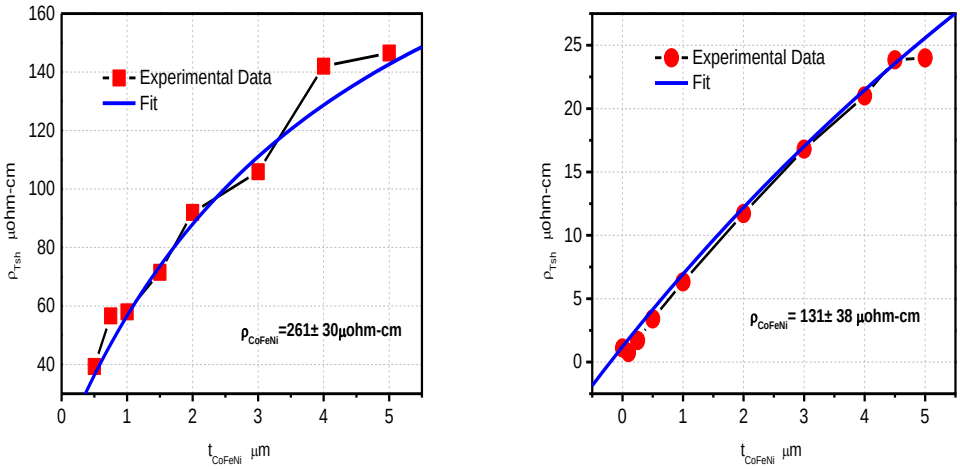

(a) (b)

Figure 118. (a) CoFeNi alloy deposited on a NiFe seed (b) CoFeNi alloy deposited on Cu seed with varying thickness

Additionally, the model does not consider the effect of epitaxial mismatch between the CoFeNi film and the underlying seed layer during the thin film growth. The simplicity of the model overlooks other factors like difference in lattice parameters, grain structure, interfacial scattering and hence, a significant difference in the actual value of CoFeNi thin film resistivity is obtained. However, these results show that the total resistivity of the CoFeNi thin film measured using four point probe technique is a function of the seed

layer. Secondly, the results shown in Figures 118a and 118b also demonstrate the effect of thickness of the CoFeNi film on its actual resistivity. Higher film thickness minimizes the electron shunting through the underlying Cu seed layer and hence, the four point probe technique measures an increased value of the CoFeNi film resistivity.

6.4.2. Resistivity control of CoFeNi alloys using quaternary elements

In order to improve the electrical properties of the electrodeposited CoFeNi alloys, a quaternary element such as chromium (added as Cr^{3+}), vanadium (added as VO^{2+}), and EDTA is added in extremely small proportions in the plating solutions. In this section, the effect of addition of Cr^{3+} and VO^{2+} in the plating solution on the resistivity of CoFeNi alloys is studied. Figure 119a shows the effect of Cr^{3+} on the resistivity of the deposited CoFeNi thin films.

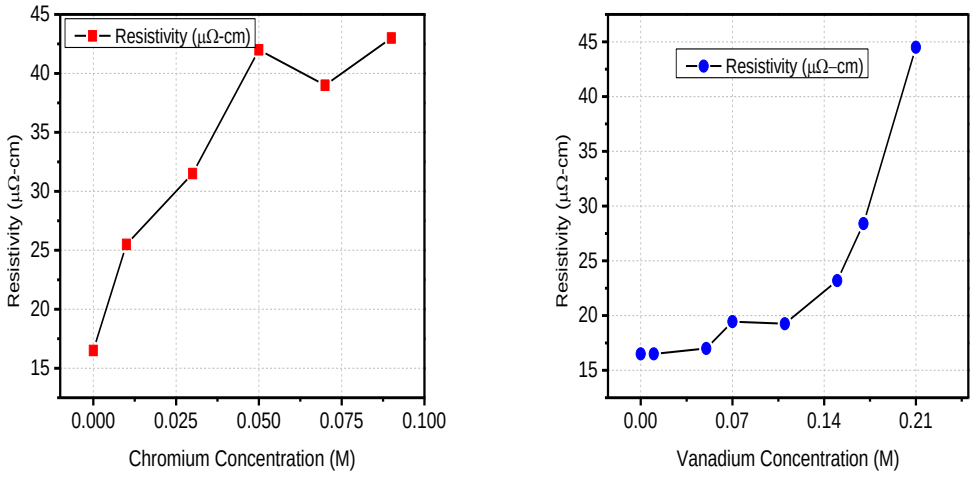

(a) (b)

Figure 119. Effect of addition of the fourth element (a) Cr^{3+} (b) VO^{2+} on the electrical properties of the electrodeposited CoFeNi thin films.

With an increase in the Cr^{3+} concentration in the solution, the resistivity of the electrodeposited CoFeNi thin film is shown to increase. This effect can be attributed to

the precipitation of the Cr_2O_3 as an oxide phase in the deposit. Brankovic et al. have experimentally proven with a sophisticated EELS measurement that the oxygen/oxide incorporation in a deposit is along the grain boundary region. Hence, the Cr_2O_3 oxide phase being a low energy phase is adsorbed preferentially at the grain boundaries and provides active sites for electron scattering. An increase in Cr^{3+} concentration in the solution leads to a higher precipitation of the Cr_2O_3 oxide phase resulting in an increase in the resistivity of the electrodeposited CoFeNi film. On similar lines, the trend observed in Figure 119b can be used to explain the influence of VO^{2+} concentration in the solution on the resistivity of the electrodeposited CoFeNi thin films. The quaternary element vanadium gets incorporated into the CoFeNi deposit as an oxide phase being preferentially adsorbed as a low energy phase at the grain boundaries. This contributes to the electron scattering at the grain boundaries thereby boosting the resistivity of the electrodeposited CoFeNi films.

However, while studying the impact of the quaternary element on the resistivity of the deposited CoFeNi film, the effect on other metallurgical and magnetic properties of the CoFeNi films is also investigated.

6.5. Permeability Measurements

Referring back to the literature work discussed in Chapter 1, the field due to eddy currents can be related to the physical characteristics of the material, namely resistivity and permeability. The equation which relates the field to these parameters can be expressed as

$$\mu_{Total} = \mu_{FMR}\left(\frac{(1-t)e^{(1+j)d/\delta} - 1}{(d/\delta)\cdot e^{(1+j)d/\delta} + 1}\right), \qquad \text{Equation 133}$$

where μ_{Total} is the total permeability, μ_{FMR} is the permeability measured using the FMR setup, t is the thickness of the film, δ is the loss tangent (dielectric loss) of the film and can be expressed in terms of resistivity is shown in Equation 134 as

$$\delta = \sqrt{\frac{\rho}{\pi \cdot \mu_o \mu_{FMR} \cdot f}}, \qquad \text{Equation 134}$$

where f is the frequency spectrum over which the permeability is recorded, μ_o is the absolute permeability and μ_{FMR} is the relative permeability of the CoFeNi film.

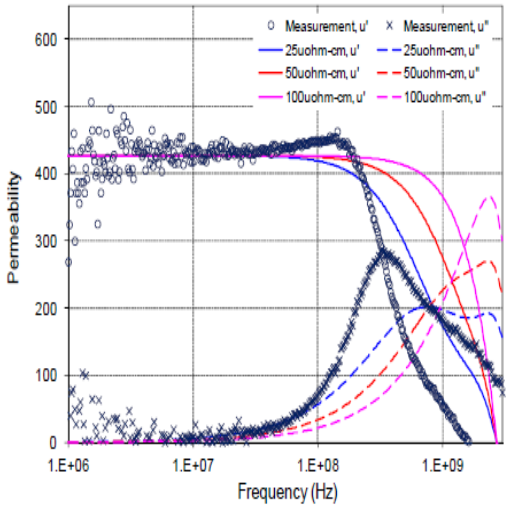

Figure 120. Data plotted from permeability measurements performed on 2μm thick electrodeposited CoFeNi films.

From Equations 133 and 134 it is evident that the permeability of a thin film is dependent on the film thickness and is also influenced by the thin film resistivity. Hence, an optimum value of resistivity and permeability for a thin film should be chosen for maximum performance of the film in MEMS/NEMS devices. The above Equation 133 is

used to fit the data obtained from permeability measurements and the values of permeability and resistivity are extracted. Figure 120 shows a typical data plotted from the permeability measurements. The solid lines show the real part of the permeability spectrum whereas the dotted lines show the imaginary part. The lines corresponding to different resistivity values are used to fit the real part of the permeability curve. The quality of the fit depends upon the frequency selected for the roll off and hence, the parameters extracted are dependent on the roll off frequency. Figures 121a and 121b show the trend in relative permeability and resistivity measured as a function of the film thickness. The graphs show that the resistivity model earlier discussed in the dissertation holds true and the thickness of the deposited film does impact the total resistivity measured.

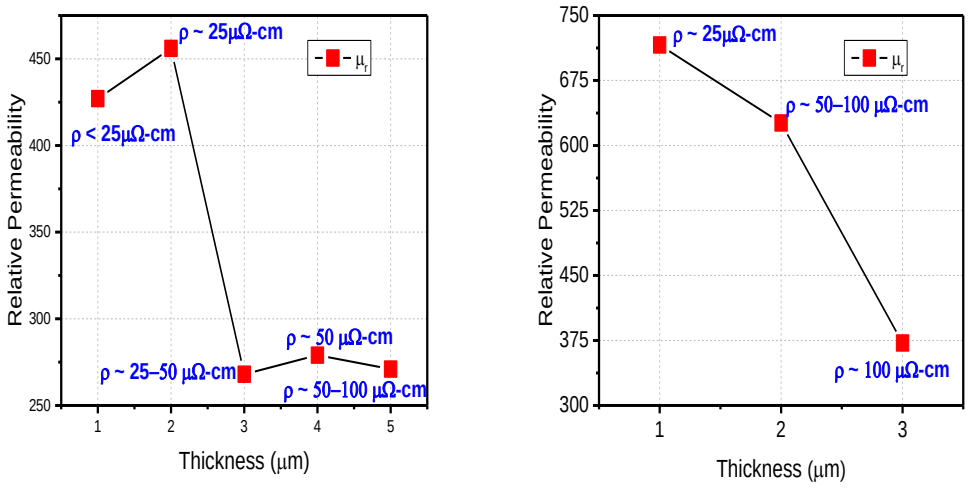

(a) (b)

Figure 121. Inter-dependence of permeability and resistivity of CoFeNi films electroplated using (a) bath III (b) bath IV on the film thickness

The results are in agreement with the Equation 133 and 134 which illustrate the interdependence of the permeability and the resistivity of the CoFeNi thin films. The

films deposited from bath III and bath IV solutions show a similar trend. The permeability has shown to decrease and resistivity of the CoFeNi films is increasing with an increase in the film thickness.

6.6. Resistivity Control in Cu Nanostructures

6.6.1. External Strain – Strain Controlled Layer

More than 50 cantilevers were annealed with Cu-interconnect nanostructures. Four different stress/strain control layers were used giving the wide spread ε_{rr} and $\varepsilon_{\theta\theta}$ values in the Cu nanostructures. The measured strain is in the range of 10^{-5} to 10^{-4}. The resistance of Cu interconnects was measured before and after the annealing cycle using microprobe resistivity measurement setup. The change in resistance was negative, i.e. $\Delta R<0$ implying that the resistance before annealing was greater than the resistance after annealing. The values of ΔR are in the range of -1000Ω to -6000Ω. The summary of these results is plotted in Figure 122A and Figure 122B showing the change in resistance for samples with CD 50nm and CD 64nm respectively. These samples were annealed at 200^{o}C and 250^{o}C and the data points corresponding to these annealing cycles are represented as black squares and red circles respectively. Although the data have a significant scattering behavior for both the annealing temperatures, they show an obvious trend in agreement with the proposed hypothesis. Interestingly, the cantilevers annealed at lower temperatures show higher scattering in the resistance data. The lowest and the highest values of the measured resistance decrease is also observed for structures annealed at lower temperatures. Undoubtedly, the results obtained suggest that the strained annealing

of Cu interconnects is an effective approach that can be employed to improve the resistance of Cu interconnects.

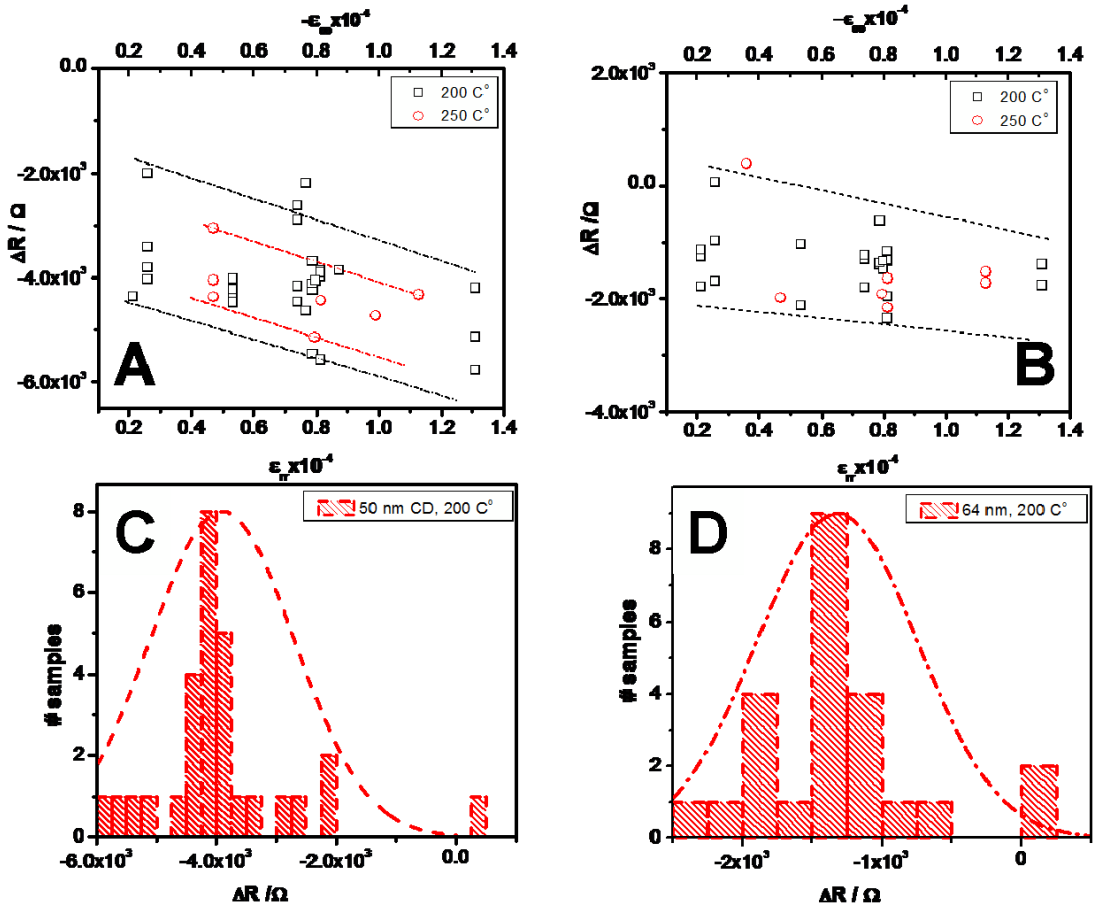

Figure 122. Cumulative data for more than 50 cantilevers (a) Cu interconnects with structures having CD 50nm (b) 64nm. The dashed lines in (a) and (b) show the outer boundaries of the trend. The histogram for ΔR during annealing of (c) CD 50nm and (d) CD 64nm at 200°C.

According to the thermodynamic criteria for the grain boundary densification (GBD) process to occur, the tensile strain in the rr direction will not improve conditions for densification of the grain boundaries with interface vector orthogonal to the length of Cu interconnects. In fact, it will make the GBD process for these grain boundaries even more difficult. However, the externally imposed compressive stress in θθ direction should

benefit the GBD process of the grain with interface vector parallel to the longer dimensions of interconnects (θθ axis). The θθ direction is also parallel to the current carrying path in Cu interconnects. Considering the length of these interconnects to be of the order of hundreds of microns, grain boundary scattering provides a dominant contribution to the resistance of these interconnects. The scattering event mainly occurs at the grain boundaries with the surface vector parallel to the current path. Externally applied strain does provide the thermodynamic conditions where densification of these grain boundaries is allowed. Therefore, the results shown in Figure 122a and 122b are in agreement with the theoretical postulates. In general, any grain boundaries with relatively small angle between their interface vector and θθ direction along which the compressive strain is imposed should benefit from the strained annealing in terms of the GBD process.

The mean ΔR value for interconnects with CD 50nm which are annealed at 200 ^{o}C is -4000Ω when the mean external strain, $\varepsilon_{\theta\theta} = -0.8*10^{-4}$. Similarly, the mean ΔR value for interconnects with CD 64nm which are annealed at 200 ^{o}C is -1100Ω when the mean external strain, $\varepsilon_{\theta\theta} = -0.8*10^{-4}$. These results are represented as histograms as shown in Figure 122c and 122d. The decrease in the resistance for structures with CD 50nm is more as compared to 64nm which shows that the structures with smaller CD benefit more and the effect reduces for higher CD. This trend could be explained by using the simple argument of the grain boundary density per unit length of the interconnect structures. All interconnects have the same length and for 50nm interconnects there are more grain boundaries per unit length (or volume) than 64nm interconnects. Thus, it is expected that the strained annealing will affect the grain boundaries per length of the

structures with smaller dimensions. Additionally, it is very important to mention that a very close value of the mean strain is imposed to Cu interconnects with CD 50nm and 64nm which allows us to compare the ΔR values when annealed at the same temperature (200 ^{o}C). The ratio for change in resistance for CD 50nm and CD 64nm can be calculated as ((ΔR_{mean} (50nm)/ ΔR_{mean} (64nm))) ≈ 4. Similarly, the ratio between the numbers of Cu grains per volume of these two structures is ≈ 2. This suggests that strained annealing benefit to resistance of Cu interconnects cannot be entirely understood by considering its effect only on Cu grain boundaries. For instance, the strained annealing might affect the interface quality between the electrodeposited Cu and the seed layer. In addition to that, segregation of grain boundaries as a function of strained annealing could play a role as well.

6.6.2. External Strain – "Vise" Method

More than 100 cantilevers were annealed with Cu interconnect structures in the vice configuration. Out of these annealed samples, roughly 60 samples were electrically tested in Intel and these results are briefly discussed in this dissertation. The resistance of Cu interconnects were measured before and after annealing and in the case of all structures, a significant decrease in the resistance was observed. Depending on the wafer/cantilever tested, the resistance decrease varied. In general, the test structures with the smallest CDs have shown a largest change in the resistance (decrease). The representative data shown in Figure 123 and Figure 124 for structures from the wafers 876 and 877 respectively. For some samples, a clear linear regression is observed for resistance change as a function of the imposed strain using the vice.

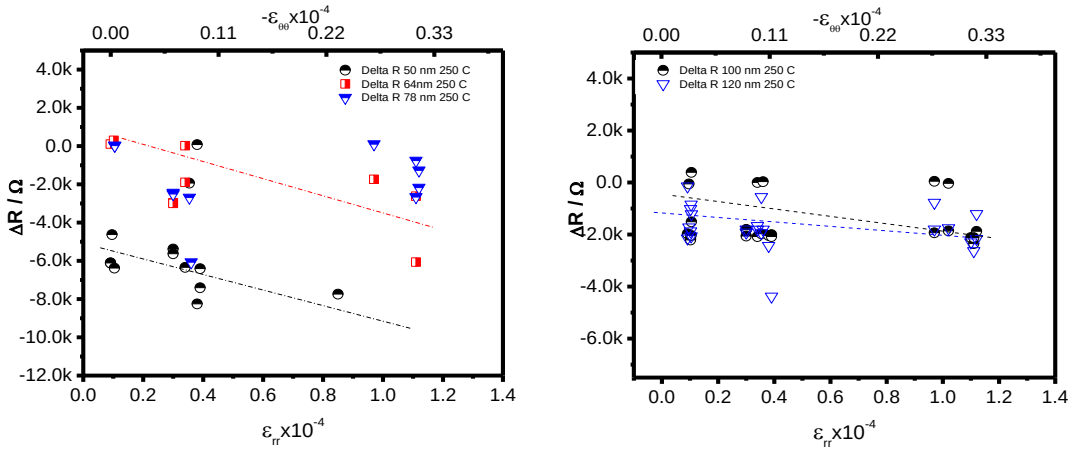

Figure 123. W 876 Representative data for resistance change in devices with 50 nm, 64 nm, 78 nm 100 nm, 108 nm, and 120 nm CD as a function of the strain during annealing. The annealing temperature was 250 C.

As explained in the earlier section, the thermodynamic criteria for grain growth via grain boundary densification suggests that the external imposed strain should only benefit GBD process of the grain boundaries which have a surface vector parallel to the longer dimension/direction of the interconnects (θθ) axis. The direction is also parallel to the current path through the Cu interconnects.

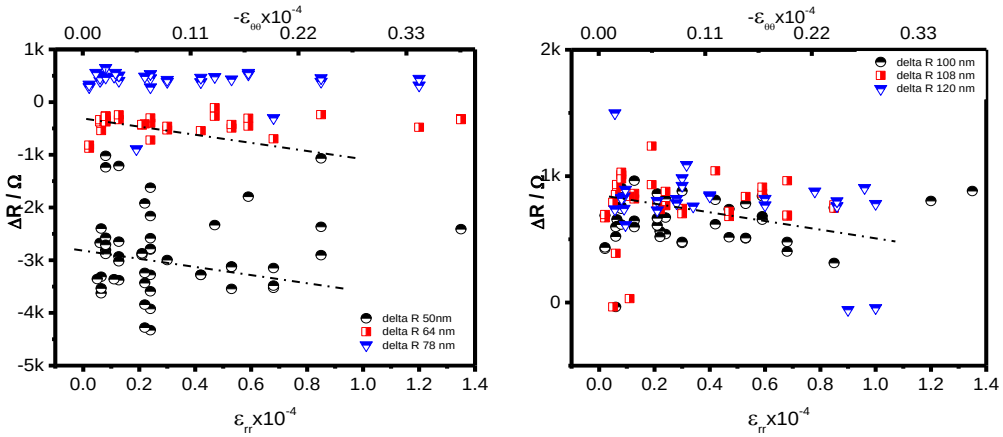

Figure 124. W 877 Representative data for resistance change in devices with 50 nm, 64 nm, 78 nm 100 nm, 108 nm, and 120 nm CD as a function of the strain during annealing. The annealing temperature was 250 C.

Considering that the length of Cu interconnect is hundreds of microns, while the width is only <100nm, the significant contribution to the resistance is the electron scattering from these particular grain boundaries. External straining obviously does provide thermodynamic conditions where densification of these grain boundaries is allowed at intermediate temperatures and thus the observed results are in agreement with the theoretical postulates. Figures 125a and 125b show the comparison of change in resistance of not annealed (NA) and pre-strained samples. The certain ambiguity emerged when the data from the control samples were compared against the data from the annealed samples. The control samples were not processed or annealed but just electrically re-tested at the same time and testing station where the other annealed samples were tested.

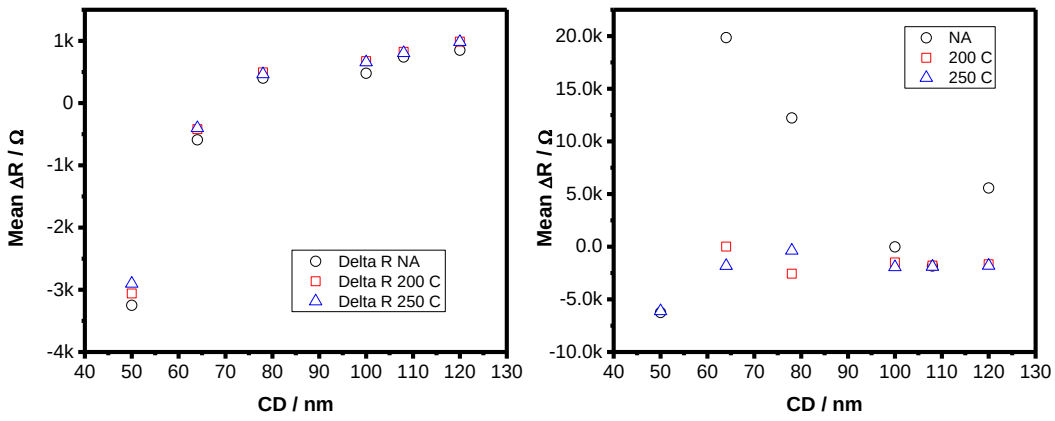

(a) (b)

Figure 125. Mean value of the resistance change for wafers (a) 877 and (b) 876 as a function of the sample/interconnect CDs. The NA abbreviation in the graph stands for the data for control (not annealed =NA) samples.

While some NA samples showed lower or no decrease in the resistivity, certain NA samples did show a higher change in the resistivity (even more than the strained samples). It may be that the electrical testing did have some kind of a bias which needs to be eliminated while recording the resistivity. This would be a future task to explore.

CHAPTER 7

CONCLUSIONS AND FUTURE WORK

This chapter concludes the dissertation work and proposes some relevant future work to explore the fundamentals of the research discussed in this dissertation. In the first part of this research, the presented results and discussions address in detail the procedure for designing the electroplating solutions and process parameters for electrodeposition of novel magnetic materials. An existing plating solution proposed by Brankovic et al. [88] is used as the initial recipe for plating the ternary CoFeNi alloys. A novel electroplating bath is designed from this initial bath by adjusting the metal ion concentration and replacing the buffer chemicals in the solution. The effect of change in the metal concentration, namely Fe and Co, directly affected the composition of the deposited films. Increase in Fe concentration in the solution inhibited the Ni deposition rate and thereby reduced the Ni content in the deposit. The existing buffer chemicals were replaced from the initial bath due to the environmental hazards of boric acid. The effect of new buffer chemicals, citric acid and sodium citrate on the electrical, magnetic and metallurgical properties of the electrodeposited CoFeNi films is further investigated. Results show that changing the buffer chemical leads to desired effects as a direct impact on resistivity of the films is observed without hampering its magnetic and metallurgical properties. After proposing the final bath designs for electroplating, the effect of plating parameters such as pH, current density etc. is studied on the properties of the electrodeposited thin films. An optimum current density pertaining to each bath is selected, J=8.64mA/cm^2 for plating solution III and J=9.6mA/cm^2 for plating solution IV.

This plating design and the process parameters are used to electrodeposit CoFeNi alloys at a high deposition rate (>150nm/min). For the current applications in MEMS devices few micron thick films are needed, this plating process can significantly reduce the fabrication costs. The plated CoFeNi films yielded a high resistivity (>100μΩ-cm) which was verified by the permeability measurements and by the theoretical model proposed to explain the dependence of resistivity on film thickness, seed layer and the seed layer thickness. The magnetic properties of the CoFeNi films were favorable as it yielded high saturation magnetization (1.8-2.2T).and significantly lower values of coercivity (<12 Oe). These parameters were measured through sophisticated sample preparation techniques where an extensive effort was taken to fabricate these samples in a clean room environment (Class 100). Additionally, the effect of saccharin on the magnetic, electrical and crystallographic properties of CoFeNi alloys is studied. The effect of saccharin as a stress reliever is investigated by recording the in-situ stress during deposition. Saccharin acts a stress reliever, improves the surface smoothness and hence, serves the purpose of an additive in the plating solution. The inclusion of the fourth element 'X' in the alloy showed a promising effect on the resistivity of the alloy. However, the magnetic and physical properties of the alloy were altered due to the oxide precipitation at the grain boundaries (CrO^{2-} for instance). In future, it would be interesting to see a combined effect of the additives and the fourth element incorporation on the properties of the plated CoFeNi films. Also, in-situ stress measurements during annealing could be a task to be undertaken in the near future.

The experimental data for the strained annealing samples certainly suggests that the externally imposed strain has a positive effect on the resistivity. The compressive

strain applied along the longer dimension of the Cu interconnects induced an overall decrease of strain energy in the Cu grains. Therefore, the local conditions for GBD process were achieved stimulating the densification of the grain boundaries with the interface vector parallel to the current path. Similarly the tested data from the "vise" measurements also indicate that externally imposed strain during annealing has effect on resistivity of Cu interconnects. Some measurements/data do show clear linear trend between the strain during annealing and achieved decrease in resistivity while some data do not show this trend. The strain is compressive along the length of the Cu interconnect and tensile across the interconnect width. The effect is largest for pattern with 50 nm and decreases as the CDs increase to 64 nm and 78 100nm, 108 and 120 nm. Analysis of the data from one wafer (W876) indicate that strained annealing has positive effect. These results are encouraging. For future work, a simpler system is needed to be developed to fabricate Cu samples in a cost-effective way. Availability of higher number of Cu samples for the strain annealing experiments will be definitely helpful in the study of conductivity improvements on the Cu interconnects at nanoscale.

REFERENCES

1. Peter Wissmann and Hans-Ulrich Finzel, Electrical Resistivity of Thin Metal Films, Springer Tracts in Modern Physics.
2. K. Fuchs, "The conductivity of thin metallic films according to electron theory of metals", *Mathematical Proceedings of the Cambridge Philosophical Society.*, 34(01), (1938).
3. B.D.Cullity and C.D. Graham, Introduction to magnetic materials, New York Wiley (2008).
4. S.R.Brankovic, N. Vasiljevic and N. Dmitrov, " Chapter 27: Applications to Magnetic Recording and Microelectronic Technologies", Modern Electroplating V, editors: M. Paunovic and M. Schlesinger, John Wiley and Sons, Inc (2010)
5. S.R. Brankovic, B. Kagajwala, J. George, G. Majkic, G. Stafford and P. Ruchhoeft, " Stress Control in Electrodeposited CoFe films", *Electrochimica Acta*, 83 (387), (2012).
6. M. Moriyama, K. Matsunaga and Masanori Mukarami, "The Effect of Strain on Abnormal Grain Growth in Cu Thin Films", *Journal of Electronic Materials,* 32 (4), (2003).
7. K. N. Tu, "Recent advantages on electromigration in very large scale integration of interconnects", *Journal of Applied Physics*, 94 (9*)*, (2003).
8. N.Dole and S.R. Brankovic, "Strained Annealing of Cu Interconnects – Pathway to Improve Conductivity via Grain Boundary Densification Process", *TECHCON*, Sept 9-11 (2013).

9. Allen J. Bard and Larry R. Faulkner, Electrochemical Methods – Fundamentals and Applications, John Wiley & Sons (2001).
10. Eliezer Gileadi, Electrode Kinetics – for Chemists, Chemical Engineers, and Materials Scientists, Wiley – VCH (1993).
11. E.I. Cooper, C. Bonhote, J. Hiedmann, Y. Hsu, P. Kern, J.W. Lam, M. Ramasubramnian, N. Robertson, L.T. Romankiw and H. Xu, "Recent developments in high moment electroplated materials for recording heads", *IBM Journal of Research and Development*, 49(1), 92005).
12. Sholeh Hessami and Charles W. Tobias, "A Mathematical Model for Anomalous Codeposition of Nickel-Iron on a Rotating Disk Electrode", *Journal of the Electrochemical Society*, 136 (12), (1989).
13. A. Brenner, Electrodeposition of alloys: Principles and Practice, 2(137), Academic Press, New York (1963).
14. H. Dahms and I.M. Croll, "The Anomalous Codeposition of Iron-Nickel Alloys", *Journal of the Electrochemical Society*, 112 (771), (1965).
15. L. T. Romankiw, "Electrodeposition Technology, Theory and Practice", L. T. Romankiw, Editor, *the Electrochemical Society Softbound Proceeding Series*, 87(17), (1987).
16. Wendy C. Grande, and Jan B. Talbot, "Electrodeposition of Thin Films of Nickel-Iron: II. Modeling TECHNICAL PAPERS - Electrochemical Science and Technology", *Journal of the Electrochemical Society*, 140(3), (1993).

17. Michael Matlosz, "Competitive Adsorption Effects in the Electrodeposition of Iron Nickel Alloys TECHNICAL PAPERS - Electrochemical Science and Technology", *Journal of the Electrochemical Society*, 140 (8), (1993).
18. Brett C. Baker, and Alan C. West, "Electrochemical Impedance Spectroscopy study of Nickel-Iron Deposition: I. Experimental Results TECHNICAL PAPERS - Electrochemical Science and Technology" *Journal of the Electrochemical Society*, 144 (1), (1997).
19. Brett C. Baker, and Alan C. West, "Electrochemical Impedance Spectroscopy study of Nickel-Iron Deposition: II. Theoretical Interpretation TECHNICAL PAPERS - Electrochemical Science and Technology" *Journal of the Electrochemical Society*, 144 (1), (1997).
20. N. Zech, E. J. Podlaha, and D. Landolt, "Anomalous Codeposition of Iron Group Metals: I. Experimental Results Articles", *Journal of the Electrochemical Society*, 146(8), (1999).
21. N. Zech, E. J. Podlaha, and D. Landolt, "Anomalous Codeposition of Iron Group Metals: II. Mathematical Model Articles", *Journal of the Electrochemical Society*, 146 (8), (1999).
22. Y. Zhuang, and E. J. Podlaha, "NiCoFe Ternary Alloy Deposition: I. Experimental Kinetic Study Articles", *Journal of the Electrochemical Society*, 147 (6), (2000).
23. Y. Zhuang, and E. J. Podlaha, "NiCoFe Ternary Alloy Deposition: II. Influence of Electrolyte Concentration at Steady State ELECTROCHEMICAL/CHEMICAL

DEPOSITION and ETCHING", *Journal of the Electrochemical Society*, 150 (4), (2003).

24. Y. Zhuang, and E. J. Podlaha, "NiCoFe Ternary Alloy Deposition: III. A Mathematical Model ELECTROCHEMICAL/CHEMICAL DEPOSITION and ETCHING", *Journal of the Electrochemical Society*, 150 (4), (2003).
25. I. W. Wolf, "Electrodeposition of Magnetic Materials", *Journal of Applied Physics*, 33 (3), (1962).
26. Jinnie George, James Rantscheler, Sang-Eun Bae, Dmitri Litvinov and Stanko R. Brankovic, "Sulfur and Saccharin Incorporation into Electrodeposited CoFe Alloys: Consequences of Magnetic and Corrosion Properties", *Journal of the Electrochemical Society*, 155 (9), (2008).
27. Ibro Tabakovic, Steve Riemer, Katmerka Tabakovic, Ming Sun and Mark Kief, " Mechanism of Saccharin Transformation to Metal Sulfides and Effect of Inclusions on Corrosion Susceptibiltiy of CoFe Magnetic Films", *Journal of The Electrochemical Society*, Volume 153, Issue 8, Pages C586- C593 (2006).
28. Steve Riemer, Jie Gong, Ming Sun and Ibro Tabakovic, "Influence of Solution pH and Concentration of Solution on Electrodeposition and Properties of 2.4 T CoFe Alloys", *Journal of The Electrochemical Society*, Volume 156, Issue 10, Pages D439-D447 (2009).
29. Stanko R. Brankovic, Ryan Haislmaeir and Natasa Vasiljevic, " Molecular Incorporation of Saccharin into Soft High Moment CoFe Alloys", *ECS Transactions*, 3(25), Pages 71-80 (2007).

30. B. Kagajwala, Stress control in electrodeposited permalloy films, University of Houston, Master thesis, p.25 (2010).
31. H. J. Frost, " Microstructural evolution in thin films", *Materials Characterization*, 32(4), Pages 257-273(1994).
32. Hang Z. Yu and Carl V. Thompson, " Grain growth and complex stress evolution during Volmer-Weber growth of polycrystalline thin films", *Acta Materialia*, 67, Pages 189-198, (2014).
33. Carl V. Thompson and Roland Carel, "Texture development in polycrystalline thin films", *Material Science and Engineering:B*, 32(3), Pages 212-219 (1995).
34. Carl V. Thompson and Roland Carel, " Stress and grain growth in thin films", *Journal of the Mechanics and Physics of Solids*, 44 (5), Pages 657-673 (1996).
35. W. D. Nix and B. M. Clemems, " Crystallite coalescence: A mechanism for intrinsic tensile stresses in thin films", *Journal of Materials Research*, 14 (8), Pages 3467-3473, (1999).
36. Stanko R. Brankovic, "Saccharin effect on properties of 2.4 T CoFe films", *Electrochimica Acta* in press (2012).
37. Tetsuya Osaka, Takahiro Sawaguchi, Fumio Mizutani, Tokihiko Yokoshima, Madoka Takai and Yutaka Okinaka, " Effect of Saccharin and Thiourea on Sulfur Inclusion and Coercivity of Electroplated Soft Magnetic CoNiFe film", *Journal of The Electrochemical Society*, 146(9), Pages 3295-3299 (1999).
38. Paul L. Rossiter, The electrical resistivity of metals and alloys, Cambridge University Press, London (1987).

39. Tik Sun, Classical Size effect in copper thin films: Impact of surface and grain boundary scattering on resistivity, PhD Dissertation (2009).
40. Fen Chen and Don Gardner, "Influence of line dimensions on the resistance of Cu interconnects", *IEEE Electron Device Letters*, 19 (12), (1998).
41. H.B. Lee, "A highly reliable Cu interconnect technology for memory device", *IITC Proc.*, p64 (2007).
42. "International technology Roadmap for Semiconductors, 2003 Edition, Executive Summary", http://public.itrs.net/
43. S. M. Rossnagel and T. S. Kuan, "Alteration of Cu conductivity in the size effect regime", *J. of Vac. Sci. Technology B*, 22, 240 (2004).
44. P. Kapur, J. P. McVittie and K.C. Saraswat, "Technology and reliability constrained future copper interconnects. II. Performance implications", *Electron Devices, IEEE Transactions on*, 49 (598-604), (2002).
45. Victor V. Zhirnov, R. K. Cavin, D.J.C.Herr and T.A.Woolridge, "On Designing Sub-70nm Semiconductor materials and processes", *IEEE Transactions on Semiconductor Manufacturing*, 15(2), (2002).
46. P. Kapur, J. P. McVittie and K.C. Saraswat, "Realistic copper interconnect performance with technological constraints", *Proceedings of the IEEE 2001 International*, (233 – 235), (2001).
47. E.H. Sondheimer, "The mean free path of electrons in metals", *Advances in Physics*, 1(1), (1952).

48. J. W. Lim and M. Isshiki, “Electrical resistivity of Cu films deposited by ion beam deposition: Effects of grain size, impurities and morphological defect”, *J. Appl. Phys.*, 99 (9), (2006).
49. S. G. Soffer, “Statistical model for the size effect in electrical conduction”, *J. Appl. Phys.*, 38, 1710, (1967).
50. Mayadas A. F. and Shatzkes M., “Electrical resistivity model for polycrystalline films: the case of arbitrary reflection at external surfaces”, *Phy. Rev.* B, 1 (1382-1389), (1970).
51. Mayadas A.F., Shatzkes M., Janak J.F., “Electrical resistivity model for polycrystalline films: the case of specular reflection at external surfaces”, *Appl. Phys. Lett.*, 14 (345-347), (1969).
52. J. C. Hensel, R. T. Tung, J. M. Poate and F.C.Unterwald, “Specular Boundary Scattering and Electrical Transport in Single-Crystal Thin Films of $CoSi_2$”, *Phys. Rev. Lett.*, 54 (1840-1843), (1985).
53. Tetsuya Osaka, Tokihiko Yokishima and Takuya Nakanishi, “Effect of Impurities on Resistivity of Electrodeposited High B_s CoNiFe Based Soft Magnetic Thin Films”, *IEEE Transactions on Magnetics*, 37(4), (2001).
54. N.V.Myung and K. Nobe, “Electrodeposited Iron group thin film alloys: Structure-Property Relationships”, *Journal of The Electrochemical Society*, 148 (3), (2001).
55. P.C. Andricacos and N. Robertson, “Future directions in electroplated materials for thin-film recording heads”, *IBM J. Res. Dev.*, 42 (671), (1998).

56. S. Hossain, Stress control during annealing of magnetic thin film alloys, University of Houston, Master thesis (2011).
57. Z. Liu and Y. Hong, "Stress relaxation of thin film due to coupled surface and grain boundary diffusion", *Thin Solid Films,* 518 (20), (2010).
58. E. Chason, J.W. Shin, S.J. Hearne and L.B. Freund, "Kinetic model for dependence of thin film stress on growth rate, temperature and microstructure", *J. Appl. Phys.*, 111 (2012).
59. L. B. Freund and E. Chason, "Model for stress generated upon contact of neighboring islands on the surface of a substrate", *J. Appl. Phys.*, 88 (4866), (2001).
60. S. Brand, The Clock of the Long Now, Basic Books, New York (1999).
61. G.E.Moore, "Cramming more components into integrated circuits", *Proceedings of the IEEE*, 86(1), (1998).
62. P. Chaudhari, "Grain Growth and Stress Relief in Thin Films", *J. Vac. Sci. Technol.,* 9 (520), (1972).
63. M.F. Doerner and W.D. Nix, "Stresses and deformation processes in thin films on substrates", *Critical reviews in Solid State and Material Science*, 14 (225), (1988).
64. A. Ibanez, "Mechanical and structural properties of electrodeposited copper and their relation with the electrodeposition parameters", *Surf. And Coatings Tech.*, 191 (2005).
65. Simon Foner, "Versatile and Sensitive Vibrating Sampling Magnetometer", *Review of Scientific Instruments*, 30 (548), (1959).

66. Wesley Burgei, Michael J. Pechan and Herbert Jaeger, "A simple vibrating sample magnetometer for use in a materials physics course", *Association of Physics Teacher*s, 10.1119/1.1572149 (2003).
67. J. D. Plummer, M.D. Deal and P.B. Griffin, Silicon VLSI Technology: Fundamentals, Practice and Modeling, Prentice Hall Publications (2000).
68. B. Kagajwala, Stress control in electrodeposited permalloy films, University of Houston, Master thesis (2010).
69. O. E. Kongstein, U. Bertocci and G.R. Stafford, "In-situ stress measurements during copper electrodeposition on 111- Textured Au", *J. of Electrochem. Soc.*, 152 (3), C116 – C123 (2005).
70. G. G. Stoney, "The Tension of Metallic Films Deposited by Electrolysis", *Proceedings of the royal society of London*, 82, Pages 172-175, (1909).
71. Watlow Electric Manufacturing Company, Radiant Heating with Infrared: A technical guide to understand and applying infrared heaters, (1997).
72. D. P. DeWitt and G.D. Nutter, Theory and practice of radiation thermometry, Wiley-IEEE, (1998).
73. Chromalox Inc. Technical Documents, Chromalox Technical Information Radiant Infrared Heating – Theory and Principles, (2011).
74. Salamander Ceramic Infrared Emitters - Technical Manual, Mor Electric Heating Assoc. Inc. (2010).
75. W.R. Barron, Principles of Infrared Thermometry, Williamson Corporation, Omega Engineering, (2011).

76. Optris CTLaser, CTLaser - Infrared Sensor Operators manual (Optris CTlaser – E2007-10-C), Basic Principles of Non-Contact Temperature Measurement, (2010).
77. Klaus-Dieter Gruner, Principles of Non-Contact Temperature Measurement, Raytek (2010).
78. R. Langton, Stability and Control of Aircraft Systems Introduction to Classical Feedback Control, Wiley and Sons (2010).
79. Basic Instrumentation Measuring Devices and Basic PID Control, CNSC Technical Training Group (Science and Reactor Fundamentals – Instrumentation and Control).
80. J. Horkans, "Effect of Plating Parameters on Electrodeposited NiFe", *Journal of the Electrochemical Society: Electrochemical Science and Technology*, 128 (1), (1981).
81. L. Gianuzzi and F. Stevie, Introduction to Focused Ion Beams-Instrumentation, Theory, Techniques and Practice, Springer Verlag (2010).
82. J. C. Russ, Fundamentals of Energy Dispersive X-ray Analysis, Butterworths (1984).
83. S.J.B. Reed, Electron microprobe analysis, Cambridge University Press, 2nd edition (1993).
84. B.D.Cullity and S.R.Stock, Elements of X-Ray Diffraction, Prentice Hall, 3rd edition (2001).
85. AZ Electronics Materials, AZ 1500 Photoresist- Data Package.

86. Chris Mack, Fundamental Principles of Optical Lithography- The Science of Microfabrication, Wiley (2011).

87. L. B. Freund and S. Suresh, Thin Film Materials – Stress, Defect Formation and Surface Evolution, Cambridge University Press, p. 94 (2003).

88. Jeong Oh Lee, Hyun Kyung Kim and Won Young Jeung, "Tailoring the magnetic properties of CoFeNi alloys with variations in copper contents", *Journal of Applied Physics*, 99 (08), 08B704 (2006).

89. Hyun Kyung Kim, Dong Won Chun, Jun Hyun Han, Kwang Bum Kim and Won Young Jeung, "Effects of external magnetic field on magnetic properties and surface morphology of electrodeposited CoFeNi alloys", *Physica Status Solidi*, 204 (12), Pages 4104 – 4107, (2007).

90. Stanko R. Brankovic, Natasa Vasiljevic, Timothy J. Klemmer and Earl C. Johns, "Influence of Additive Adsorption on Properties of Pulse Deposited CoFeNi Alloys", *Journal of the Electrochemistry Society*, 152 (4), Pages C196-C202, (2004).

91. A.M. Rashidi and A. Amadeh, "Effect of Electroplating Parameters on Microstructure on Nanocrystalline Nickel Coatings", *Journal of Material Science Technology*, 26 (1), Pages 82-86, (2010).

92. Jie Gong, Steve Riemer, Augusto Morrone, Venkatram Venkatasamy, Michael Kautzky and Ibro Tabakovic, " Composition Gradients and Magnetic Properties of 5-100nm Thin CoNiFe Films Obtained by Electrodeposition", *Journal of the Electrochemical Society*, 159(7), D447-D454, (2012).

93. George Palasantzas, “Surface roughness and grain boundary scattering effects on the electrical conductivity of thin films”, *Physical review B, Condensed matter*, 58 (15), Pages 9685-9688, (1988).

94. lYahui Zhang and Douglas G. Ivey, “Electroplating of Nanocrystalline CoFeNi Soft Magnetic Thin Films from a Stable Citrate-Based Bath”, *Chemical Materials*, 16 (7), Pages 1189-1194, (2004).

95. Daheum Kim, D. -Y. Park, B.Y.Yoo, P. T. A. Sumodjo, N.V. Myung, “ Magnetic properties of nanocrystalline iron group thin film alloys electrodeposited from sulfate and chloride baths”, *Electrochimica Acta*, 48, Pages 819-830, (2003).

96. Jinnie George, Shereen Elhalawaty, A. John Mardinly, R.W. Carpenter, Dmitri Litvinov, Stanko R. Brankovic, “Oxide/hydroxide incorporation into electrodeposited CoFe alloys – Consequences for magnetic softness”, Electrochimica Acta, 110, Pages 411-417, (2013).

97. S. Elhalawaty, R. W. Carpenter, J. George and S.R.Brankovic, “Oxygen Incorporation into Electrodeposited CoFe Films: Consequences for Structure and Magnetic Properties”, *Journal of the Electrochemical Society*, 158 (11), (2011).